Copyright © 2000, by the author(s).
All rights reserved.

Permission to make digital or hard copies of all or part of this work for personal or classroom use is granted without fee provided that copies are not made or distributed for profit or commercial advantage and that copies bear this notice and the full citation on the first page. To copy otherwise, to republish, to post on servers or to redistribute to lists, requires prior specific permission.

EXTREME ULTRAVIOLET (EUV) HOLOGRAPHIC METROLOGY FOR LITHOGRAPHY APPLICATIONS

by

Sang Hun Lee

Memorandum No. UCB/ERL M00/63

13 December 2000

EXTREME ULTRAVIOLET (EUV) HOLOGRAPHIC METROLOGY FOR LITHOGRAPHY APPLICATIONS

by

Sang Hun Lee

Memorandum No. UCB/ERL M00/63

13 December 2000

ELECTRONICS RESEARCH LABORATORY

College of Engineering
University of California, Berkeley
94720

EXTREME ULTRAVIOLET (EUV) HOLOGRAPHIC METROLOGY FOR LITHOGRAPHY APPLICATIONS

Copyright © 2000

By

Sang Hun Lee

5 December 2000

ELECTRONIC RESEARCH LABORATORY

College of Engineering
University of California, Berkeley
94720

Extreme Ultraviolet (EUV) Holographic Metrology for Lithography Applications

By

Sang Hun Lee

B.S. (University of Rochester) 1996
M.S. (University of California, Berkeley) 1998

A dissertation submitted in partial satisfaction of the

Requirements for the degree of

Doctor of Philosophy
in

Engineering-Electrical Engineering
and Computer Science

in the

GRADUATE DIVISION

of the

UNIVERSITY OF CALIFORNIA, BERKELEY

Committee in charge:

Professor Jeffrey Bokor, Chair
Professor David Attwood
Professor Eicke Weber

Fall 2000

Abstract

Extreme Ultraviolet (EUV) Holographic Metrology for Lithography Applications

By

Sang Hun Lee

Doctor of Philosophy in Engineering – Electrical Engineering and Computer Sciences

University of California at Berkeley

Professor Jeffrey Bokor, Chair

Extreme ultraviolet (EUV) lithography is one of the most promising next-generation lithography techniques being developed to print the feature sizes below 0.1 μm. In order to make EUV lithography commercially viable for the manufacture of IC devices at 0.1 μm and beyond, several technological challenges remain to be solved. In this thesis, various holographic metrology systems are presented, analyzed, and implemented to address a number of the key technological issues facing EUV lithography. These issues include characterization of optical system performance, characterization of illuminator coherence properties, and detection and characterization of EUV mask-blank defects.

The holographic techniques presented here are all based on the previously described EUV phase-shifting point diffraction interferometer (PS/PDI). This interferometer has been in operation for several years and has been used to characterize and align numerous prototype EUV lithographic optical systems operating at wavelengths near 13.4 nm. Although the PS/PDI is typically viewed as a wavefront metrology tool, it can also be viewed as a special case of a holographic metrology tool where a Fourier-transform hologram of the optical

system point-spread function is recorded. Here this point of view is further developed laying the foundation for all subsequent holographic metrologies described in this thesis.

A critical issue for the PS/PDI is its accuracy, which is ultimately limited by the quality of the pinhole-diffracted illumination and reference beams. Here this ultimate accuracy is determined through computer modeling and comparisons are made to experimental results.

Although it is possible to predict imaging performance based on wavefront metrology data, it is often desirable to obtain direct measurements of the imaging performance of lithographic optics. To this end, a holographic aerial image monitoring system has been developed through modification of the PS/PDI. The system, based on lensless Fourier-transform holography, is demonstrated to provide 100-nm-resolution aerial image monitoring at EUV wavelengths. As with the original PS/PDI, this system uses synchrotron-based illumination. The system has been implemented at beamline 12.0.1 at the Lawrence Berkeley National Laboratory. The holographic system is used to characterize the imaging performance of an EUV 10×-Schwarzschild objective. The results are compared with simulations, and a good qualitative agreement is obtained. Various object patterns, including phase-shift-enhanced objects, have been studied.

Another important EUV metrology is the ability to characterize illumination coherence properties. The holographic aerial image monitoring system developed here is also well suited to the coherence metrology task. The capabilities of this method are demonstrated through the coherence characterization of two EUV synchrotron-based illuminators. Moreover, the effect of certain beamline parameters on coherence is characterized.

Another crucial component to EUV lithography is the multilayer reflective mask. Perhaps the biggest challenge for EUV mask technology is that of defect control. Because defects in the mask can be transferred to the wafer, it is crucial to have a defect free mask. The concept of holographic metrology can also be applied to the microscopic characterization of EUV multilayer-mask-blank defects. The holographic method is of particular interest because few other methods exist that can quantify both the phase and amplitude of sub-micron sized defects on EUV mask blanks. As a proof of principle, a holographic defect characterization tool is developed and demonstrated using programmed defects in transmission masks. Amplitude defects ranging in diameter from 500 nm to 70 nm are successfully characterized. Finally, extension of the holographic defect microscopy technique to the more relevant reflection mask configuration is considered in detail.

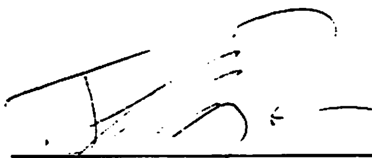

Professor Jeffrey Bokor

Committee chair

Table of Contents

CHAPTER 1. Introduction and motivation..1

1.1 EXTREME ULTRAVIOLET (EUV) LITHOGRAPHY..2
1.2 COMPONENTS OF EUV LITHOGRAPHY SYSTEMS..6
1.2.1 EUV source..6
1.2.2 Condenser system..7
1.2.3 EUV reflective mask..7
1.2.4 Projection optical system..8
1.2.5 Pattern recording resist..9
1.3 HOLOGRAPHY TECHNIQUES FOR THE ACTINIC CHARACTERIZATION OF EUV LITHOGRAPHY..9
1.3.1 Interferometric characterization of EUV lithographic optics..10
1.3.2 EUV holographic aerial image recording..11
1.3.3 Holographic microscopy..12
1.4 THESIS ORGANIZATION..13

CHAPTER 2. Phase-shifting point diffraction interferometry..............14

2.1 INTRODUCTION..15
2.2 PHASE-SHIFTING POINT DIFFRACTION INTERFEROMETER (PS/PDI): GENERAL DESCRIPTION..17
2.3 AT-WAVELENGTH CHARACTERIZATION OF EUV PROTOTYPE LITHOGRAPHIC OPTICS..19
2.3.1 EUV light source: beamline condenser system..19
2.3.2 PS/PDI configuration..22
2.3.3 Optical system under test: 10×-Schwarzschild optics..27
2.4 INTERFEROGRAM ANALYSIS METHOD..30
2.5 RESULTS OF THE PS/PDI MEASUREMENT..32
2.5.1 Alignment of 10× optics at wavelength..35
2.5.2 Chromatic effects due to multilayer coating..36
2.5.3 Flare measurements..38
2.5.4 Comparison with visible light interferometry..39
2.6 ACCURACY OF THE PS/PDI..40
2.6.1 Systematic effects from measurement geometry..40
2.6.2 Experimental method to determine the accuracy of the PS/PDI: a null test............41
2.6.3 Analytical treatment to identify the accuracy of the PS/PDI..42
2.6.4 The lower limit accuracy of the PS/PDI..43
2.6.5 The reference-wavefront-error-limited accuracy and the systematic-error-limited accuracy of the PS/PDI..44

2.7 PS/PDI AS HOLOGRAPHY....47
2.7.1 Reconstruction of the point spread function of the 10× optical systems....49
2.8 CONCLUSION....50

CHAPTER 3. EUV Holographic aerial image recording....51

3.1 INTRODUCTION....53
3.2 EUV HOLOGRAPHY SYSTEM DESCRIPTION....54
3.3 FRESNEL AND FOURIER TRANSFORM HOLOGRAPHY....55
3.4 EXPERIMENTAL SET-UP....59
3.4.1 Alignment procedure....62
3.5 RECORDING HOLOGRAMS AND ANALYSIS....64
3.5.1 Determination of the window-pinhole separation....66
3.5.2 Resolution of the reconstructed holography....66
3.6 EXPERIMENTAL RESULTS....68
3.6.1 A circular aperture....68
3.6.2 Through focus studies....69
3.6.3 More complicated objects....71
3.7 SIMULATION OF THE COHERENT IMAGING PERFORMANCE OF CAMERA A....75
3.8 EFFECT OF FLARE IN THE HOLOGRAPHIC IMAGE RECORDING SYSTEM....79
3.9 ATTENUATED PHASE-SHIFTING OBJECT....84
3.9.1 Fabrication of the attenuated phase-shifting object....84
3.9.2 Holographic characterization of the attenuated phase-shifting object....87
3.10 CONCLUSION....89

CHAPTER 4. Spatial coherence measurement of synchrotron-based illuminators....90

4.1 INTRODUCTION....91
4.1.1 Two-pinhole experiment....92
4.1.2 Holographic coherence characterization....95
4.2 HOLOGRAPHIC COHERENCE MEASUREMENT OF SYNCHROTRON-BASED EUV ILLUMINATORS....98
4.2.1 Coherence of the K-B condenser system....100
4.2.2 Coherence of the pinhole illuminator....105
4.3 CONCLUSION....107

CHAPETR 5. Holographic microscopy to characterize EUV-mask-blank defects....108

5.1 INTRODUCTION....109
5.1.1 Defects in EUV multilayer-mask-blanks....109
5.1.2 EUV holographic microscopy for characterization of EUV-mask-blank defects....110
5.1.3 EUV multilayer-mask-blank defect inspection tool....112
5.2 A PROOF OF PRINCIPLE EXPERIMENT....114
5.2.1 Experimental configuration....114
5.2.2 Transmission mask....116
5.3 EXPERIMENTAL RESULTS....119
5.3.1 Reconstruction of the Fresnel hologram....119
5.3.2 Mathematical description of the hologram reconstruction process....120
5.3.3 Results with a null mask....126
5.3.4 Reconstructed images of program defects....128
5.4 CHARACTERIZATION OF PHASE DEFECTS....131
5.5 CHARACTERIZING REFLECTION MASKS: PROPOSED SYSTEM....131
5.5.1 Multilayer bandpass issues....133
5.5.2 45° mirror and order sorting aperture....133
5.5.3 Holographic optical element: a beam-splitting grating....135
5.6 CONCLUSION....136

CHAPTER 6. Summary....138

Bibliography....142

Acknowledgments

I would especially like to express my great appreciation to my advisor Professor Jeffrey Bokor for his numerous support, encouragement, and guidance. This work is based on his continuous suggestions and ideas. I would also like to give very special thanks Dr. Patrick Naulleau at the Lawrence Berkeley National Laboratory for his supports, guidance, and advices. Additionally, I thank Professor David Attwood and Professor Eicke Weber for reviewing this thesis. I especially thank to Professor David Attwood, Dr. Kenneth Goldberg, and Dr. Edita Tejnil for their insights, supports, and encouragement.

I would like to thank the entire engineering and technical support team, includes Paul Denham, Phillip Batson, Drew Kemp, Senajith Rekawa, and others, at the Center for X-Ray Optics at Lawrence Berkeley National Laboratory for making all my work possible.

I gratefully acknowledge Eric Anderson at the Center for X-Ray Optics at Lawrence Berkeley National Laboratory for his help with the transmission fabrications. I would also like to acknowledge Dr. Chang Hyun Cho at Samsung Semiconductor for his help with the attenuated phase-shift object fabrication. I would like to thank Kia Cooper at the University of California at Berkeley for her supports in many ways.

I very much thank my family and friends for their supports, encouragements, and help that have in the end allowed me to complete this work.

I acknowledge the supports who funded this research. This work was funded by the Semiconductor Research Corporation (SRC) under the contract number 460-001 and DARPA Defense Advanced Lithography Program.

Chapter 1

Introduction and Motivation

1.1 EXTREME ULTRAVIOLET (EUV) LITHOGRAPHY 2

1.2 COMPONENTS OF EUV LITHOGRAPHY SYSTEMS 6
1.2.1 EUV source 6
1.2.2 Condenser system 7
1.2.3 EUV reflective mask 7
1.2.4 Projection optical system 8
1.2.5 Pattern recording resist 9

1.3 HOLOGRAPHY TECHNIQUES FOR THE ACTINIC CHARACTERIZATION OF EUV LITHOGRAPHY 9
1.3.1 Interferometric characterization of EUV lithographic optics 10
1.3.2 EUV holographic aerial image recording 11
1.3.3 Holographic microscopy 12

1.4 THESIS ORGANIZATION 13

1.1 EXTREME ULTRAVIOLET (EUV) LITHOGRAPHY

The fabrication of electronic devices with ever-smaller feature sizes is an ongoing challenge for the integrated circuit (IC) manufacturing community. Recently, the industrial standard critical dimension (CD) for IC devices has dropped from 0.25 μm to 0.18 μm using a lithographic system with 248-nm wavelength. As seen in Table 1-1, further progress to CDs of 0.1 μm are anticipated by extending conventional optical lithography methods to shorter wavelengths such as 193 and 157 nm and employing optical enhancement techniques such as phase-shift masks, optical proximity correction, and off-axis illumination [1-9]. For CDs smaller than 0.1 μm, however, it is widely believed that significantly different lithographic technologies will be required.

One of the most promising candidates for CDs of 100 nm and below is extreme ultraviolet (EUV) lithography [10-15]. This method continues on the path of projection optical systems but with a radical reduction in wavelength (10-15 nm) and conversion to lower numerical aperture (NA) all reflective systems. The biggest advantage of the drastic reduction in wavelength and adoption of lower-NA systems is a sizable depth of focus (DOF), which improves the manufacturing process window, while maintaining the ability to print smaller CDs [10,13].

The minimum printable feature size and the latitude of the fabrication process determine the performance of the optical lithography system. For a lithographic imaging system operating at a wavelength of λ, the resolution *res* and the *DOF* are given by

$$res = k_1 \cdot \frac{\lambda}{NA} \qquad \text{Eq. 1-1}$$

$$DOF = \pm k_2 \cdot \frac{\lambda}{NA^2}$$ Eq. 1-2

where k_1 and k_2, called "k-factors", account for the imaging system quality, illumination conditions (coherence), the use of resolution enhancement techniques (i.e. phase-shift masks and proximity correction), as well as photoresist properties. The Rayleigh criterion corresponds to k factors of 0.5. As is evidenced in Eq.1.1, reducing the operating wavelength (λ) and increasing the NA directly lead to finer resolution, however, both factors also decrease the DOF. The effect is particularly dramatic in the case of the NA due to its inverse square relation as seen in Eq. 1.2.

Lithography type	193-nm lithography	157-nm lithography	EUV lithography
Source	ArF laser	F_2 laser	Laser Plasma or discharge plasma
lens material	Fused silica, CaF	CaF	Mo/Si or Mo/Be multilayer
Time anticipated	2001	2003	2007
Printable feature size	130 nm	100 nm	70 nm and below
typical NA of optics	~ 0.75	~ 0.75	0.10 ~ 0.30
Depth of focus	~ 0.4 μm	~0.3 μm	1.4 μm ~ 0.2 μm

Table 1-1. Comparisons among advanced lithography systems. When calculating the DOF, k_1 of 0.7 and k_2 of 0.5 have been used. Larger DOF can be achieved in EUV lithography system.

EUV lithography has significant advantages over extended optical lithography for feature sizes of 100 nm and below due to its reliance primarily on wavelength reduction as opposed to increase of the NA. In EUV lithography, it is readily possible to achieve simultaneously a resolution of 100 nm or better and a DOF of 1 μm or larger. For example, for k_1=0.7 and k_2=0.5 with 13.4-nm wavelength and 0.1 NA, the smallest printable feature size is 100 nm

and the DOF is 1.4 μm. Even better performance is feasible assuming less conservative *k*-factors. Table 1-1 compares the operating wavelengths, typical NAs of the lithographic optics, the smallest printable feature sizes, and depth of focus for various advanced lithography systems.

Despite the advantages described above, EUV lithography faces several challenges. Due to the near unit refractive index [16] and strong absorption at EUV wavelengths, refractive materials for lithographic system components are not feasible. Instead, multilayer-coated reflective optics are used. The reflective multilayer coatings produce high reflectivities at EUV wavelengths via constructive interference of the weak reflections from multiple layer interfaces between two materials with dissimilar refractive indices [17]. The reflective enhancement is possible at a given incident angle when the multilayer period satisfies the Bragg condition [18,19]. The most useful multilayer material combinations operating at EUV wavelengths [20-21] are Mo/Si, Mo/Be, and their compounds. Reflectivities of ~ 70% near normal incidence can be achieved with Mo/Si and Mo/Be at wavelengths near 13 and 11 nm respectively. The reflectivity curves for Mo/Si and Mo/Be are shown in Fig.1-1 (a) and (b) respectively. The bandwidth of the multilayer mirror is approximately 0.5 nm in FWHM.

Due to high absorption in air, the EUV lithography system must operate under vacuum. This places practical constraints on the characterization and usage of these systems.

Other critical challenges for EUV lithography include the ability to manufacture optics with extremely high precision and accuracy, uniform multilayer coatings with no defects, and thermal controls of the reticle and all optical surfaces.

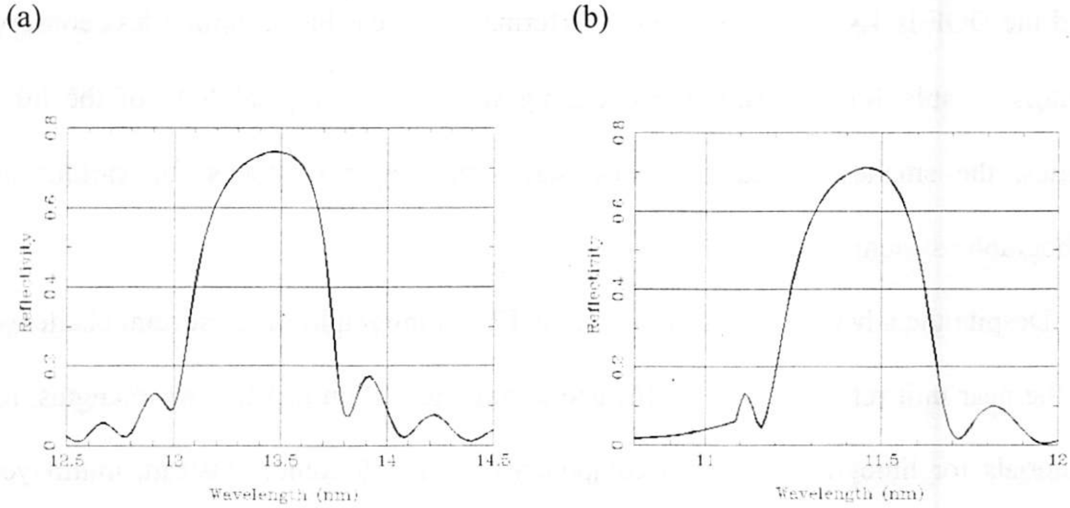

Fig.1-1 The reflectivity curves for (a) Mo/Si and (b) Mo/Be multilayer reflective mirror. The Mo/Si and Mo/Be mirrors have a peak reflectivity around 13 nm and 11 nm wavelength respectively. The 40 periods (6.9 nm for Mo/Si and 5.8 nm for Mo/Be multilayers) with $\Gamma = 0.4$ are used in the calculation. [The graphs are calculated using reference 16.]

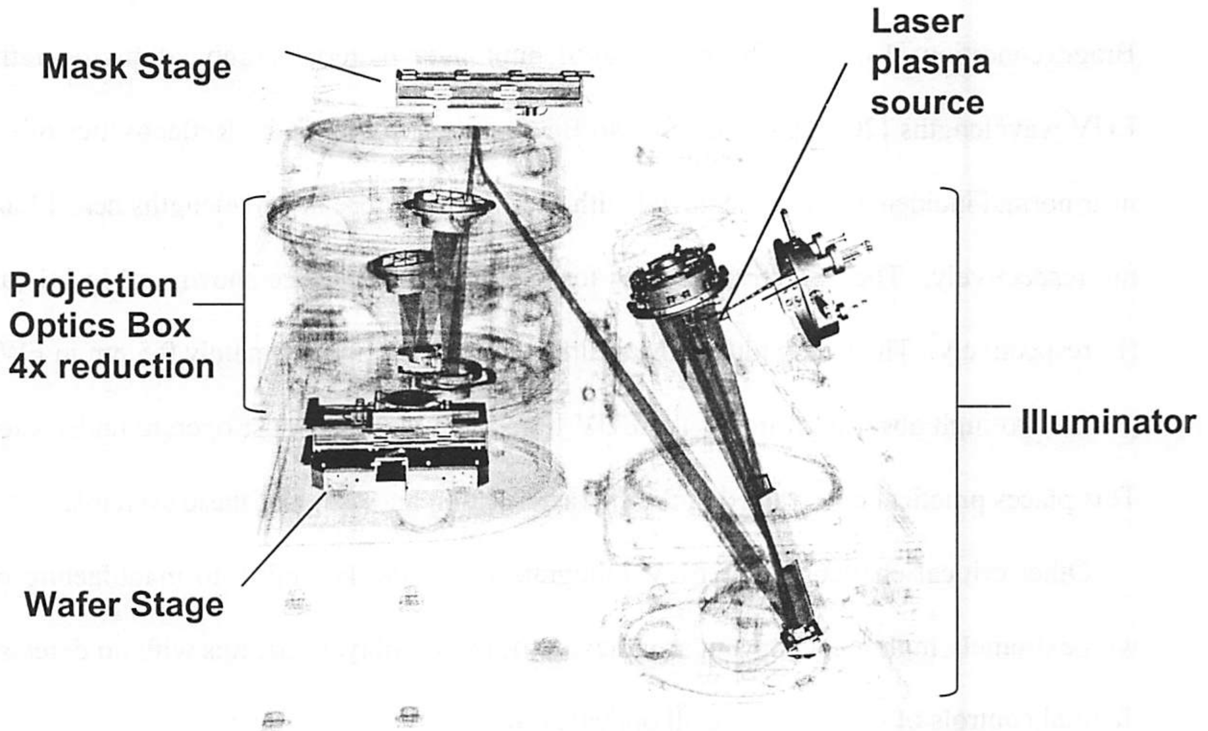

Fig. 1-2 The all-reflective EUV projection lithography system includes a laser plasma source, condenser optics, a patterned multilayer reflective mask, imaging optics, and a photoresist coated wafer. [Picture provided P. Naulleau at the LBNL. The original picture is provided by D. Tichenor at the Sandia National Laboratory.]

1.2 COMPONENTS OF EUV LITHOGRAPHY SYSTEMS

The schematic diagram of an EUV lithography system is depicted in Fig. 1-2. The lithography system consists of an EUV source, condenser optics, a patterned reflective mask, a projection optic, and an EUV sensitive photoresist-coated wafer.

1.2.1 EUV source

The radiation from the EUV light source is collected by condenser optics which illuminate the reflective multilayer mask. The projection optic produces a demagnified image of the mask onto a resist-coated wafer, which can be transferred to integrated circuit devices. EUV technology uses the same "step and scan" architecture used in some of today's DUV tools, whereby the mask and wafer are scanned synchronously.

Among possible candidates for the EUV source, the most promising is currently the laser plasma source [21-24]. It is relatively compact and has the highest demonstrated power to date. The power of the source is crucial as it is directly related to the fabrication throughput of the complete lithography system. Wafer throughput is a metric paramount to the commercial success of the technology.

The laser plasma source uses a high-power pulsed laser focused onto a xenon supersonic gas jet where xenon atomic clusters are heated to a high temperature [22-25]. The plasma produces characteristic 45-eV black body radiation with additional photons produced by excited electron transitions. The source converts 1 to 2% of the incident laser power into EUV light. This conversion efficiency forces the laser power to be 1700W or higher to meet commercial throughput requirements [23].

Another candidate as an EUV lithography source is a synchrotron radiation source [26-27]. The benefits of the synchrotron radiation source include high stability and cleanliness. However, the synchrotron source is not compact or modular. Also, the power levels remain a factor of 2 to 3 below the laser plasma source.

An electric discharge source is potentially the simplest and least expensive. However, the discharge sources are in a much earlier stage of development than the laser plasma source and synchrotron radiation source [25]. The discharge sources use high voltage and high current discharge pulses to form a 15- to 50-eV plasma in gaseous media such as Li vapor, Xe, or oxygen. 7mJ/eV pulse and up to 1000 Hz repetition rate have been achieved, and a high power prototype is currently under development. Source lifetime and elimination of the deleterious effects of eroded capillary wall material are challenging problems.

1.2.2 Condenser system

A condenser system collects the light from the EUV source and provides a proper illumination to the mask. The goals of the condenser are to collect the largest possible fraction of in-band EUV power, deliver uniform illumination to the mask, and generate a proper partial coherence or pupil fill [24, 28]. The design of the illuminating system is often the hardest task in a lithographic system design.

1.2.3 EUV reflective mask

The EUV multilayer reflective mask is fabricated by patterning an absorber material, like aluminum, titanium, or tungsten, on a multilayer-coated low-expansion-glass plate mask blank. During the exposure, EUV radiation is reflected from the non-patterned regions of the

mask and absorbed in the patterned regions. The biggest challenge for the multilayer reflective mask is defect control. Since defects in the mask can be transferred to the wafer, it is crucial to have a defect free mask.

The defects in the EUV mask can be in the substrate, multilayer-mask-blank, or patterned absorber material. The absorbing pattern is inspected for defects using mask inspection tools and is repaired as needed using focus ion beam technique. Because it is almost impossible to fix defects in a multilayer-mask-blank, the defect density on the multilayer mirror must be controlled during the fabrication process. The coating defects of the multilayer-mask-blank are divided into phase and amplitude defects. Defects in or below the multilayer can disrupt the multilayer which reduces the reflectivity and form amplitude defects. The phase defects occur when the multilayer grows conformally over a substrate defect.

1.2.4 Projection optical system

A typical EUV lithography projection system consists of 4-6 multilayer mirrors with typically 4× or 5× demagnification and a NA of 0.1-0.3. The imaging system delivers the demagnified image of the mask to the photoresist-coated wafer. The use of off-axis aspheres is required to achieve diffraction-limited performance. The use of the aspheres also helps reduce the number of mirrors used in the optical system. Each reflection causes a ~30% loss of the incident radiation power, thus, by using fewer mirrors, the throughput of the lithographic system can be drastically improved.

Tight tolerance of surface errors, much less than 1-nm rms (less than 0.25-nm rms), is required [29]. Both visible and at-wavelength interferometric characterization have been established to test such high quality EUV imaging optics.

1.2.5 Pattern recording resist

A photosensitive material is required to record the image of the patterned mask onto the wafer. DUV photoresists used by the 248-nm technology have been successfully extended to EUV wavelength with some modifications. The high absorption of EUV radiation by organic materials severely restricts the choice of resist materials and thicknesses that can be used [30-33]. Usually, the exposed thickness is a few hundred nanometers. Two EUV resist approaches, including single-layer ultra-thin resists (UTR) and bilayer resists (BLR), are currently being developed.

1.3 HOLOGRAPHY TECHNIQUES FOR THE ACTINIC CHARACTERIZATION OF EUV LITHOGRAPHY

Success of EUV lithography will bring many benefits including increased DOF and the possible extension to line widths perhaps below 30 nm. In order to make EUV lithography commercially viable to manufacture IC devices at 0.1 μm and beyond, several technological challenges remain to be solved. Among the many key technological issues in EUV lithography, this thesis concentrates on the following: wavefront characterizations and imaging performance monitoring of projection optical systems, characterizations of defects on EUV mask blanks, and measuring coherence of a synchrotron based illuminator.

In this section, a brief introduction of an at-wavelength holography technique developed to solve several key technical issues in EUV lithography is presented. The applications of holography considered here include interferometry, holographic aerial image recording, and holographic microscopy.

1.3.1 Interferometric characterization of EUV lithographic optics

The size of the printable features and robustness of the imaging process depends on the wavefront quality of the imaging optics. In order to achieve lithographic quality performance from an optical system it has been shown that a system wavefront quality of 0.02 waves rms (0.27 nm at a wavelength of 13.4 nm) is required [29]. This requirement places stringent demands on the wavefront metrology used to characterize and align the system. Ideally, the precision and accuracy of the interferometer used for optical metrology should be significantly better than the wavefront under test. The accuracy should be at least 0.01 wave rms or better. To address this problem, the phase-shifting point diffraction interferometer (PS/PDI) [37] has been developed. The PS/PDI uses pinhole-diffraction to produce coherent spherical beams used as the probe and reference waves.

The PS/PDI is a common-path interferometer based on the original point diffraction interferometer [34-36]. Because even highly monochromatized EUV sources have very short coherent lengths, less than a few tens of microns, common-path interferometer techniques are required for testing EUV lithographic optics [35]. The PS/PDI measures test optic system wavefront by interfering the system response to a spherical probe beam with a spherical reference wavefront. Because the PS/PDI requires spatially coherent radiation, it is most practically implemented using high-brightness undulator synchrotron radiation, capable of generating nearly coherent light at EUV wavelengths [38].

As a more commercially viable alignment tool, a visible light interferometer, the phase-shifting diffraction interferometer (PSDI), has been developed. The visible light interferometer clearly has advantages over the EUV PS/PDI in optical shop testing, due to its compact size, easy access, and non-vacuum operational condition. Other advantage of the

visible light interferometer is its greater convenience in testing single and uncoated elements, and the visible light interferometer is also easier to perform the final alignment of the optic. However, unlike the EUV PS/PDI, the visible light interferometer requires extremely high accuracy in measuring wavefront quality due to its large operational wavelength (λ = 532 nm). Even though the visible light interferometer can successfully measure wavefront quality of EUV optics under the condition that the multilayer coating is nearly perfect, the EUV interferometer is required for optic's final alignment with extremely high accuracy at its operational wavelength. The EUV PS/PDI has played a crucial role in the calibration and validation of the visible light PSDI. Detailed comparisons between the visible and EUV interferometers are discussed in section 2.5.4.

Noting that the interferograms recorded by the PS/PDI are essentially holograms of the system point-spread function, it becomes evident that the PS/PDI is simply a special case of a more general holographic system.

1.3.2 EUV holographic aerial image recording

As opposed to characterizing the system wavefront to predict imaging performance, it is also possible to directly characterize the coherent imaging performance of lithographic optical systems using holographic techniques. In holography, when a suitably coherent and well-known reference wavefront interferes with an arbitrary wavefront emanating from some object distribution, electric field information, including amplitude and phase can be recorded. This holographic information can be used to reconstruct the original object distribution. This holographic technique can be used to record aerial images produced by an optical system, thus directly characterizing the optic's coherent imaging performance. From the coherent

imaging performance, incoherent imaging can be readily predicted without printing in photoresist.

Utilizing the holographic aerial image recording technique, the spatial coherence of an illuminator can also be measured. In lithographic imaging systems, the *k*-factors, and hence resolution and DOF (Eq. 1-1 and 1-2), depend on the partial coherence of the illumination [39]. Since *k*-factors determine the performance of the lithographic system, it is important to characterize the coherence of the illuminator. Holographic techniques can be used to record the image of an illumination beam using a single point source element of a copy of that beam as the reference. In reconstruction, this will produce an image of only the mutually coherent portion of the illumination beam, hence the coherence area is measured.

1.3.3 Holographic microscopy

Using the holographic techniques described above to implement a holographic microscope, defects in multilayer EUV mask blanks can be directly characterized. Critical defects on the reflective mask can directly transfer to the wafer, thus a significant concern for the commercial viability of EUV lithography is defect control on the requisite reflective multilayer masks. Because there are no known methods to correct defects in and on a multilayer, it is crucial to identify the defects providing feedback for the development of a nearly zero-defect multilayer mask fabrication process.

Because both amplitude and phase information is recorded with the holographic technique, it is suitable for the direct characterization of both phase and amplitude defects on the multilayer EUV mask blanks. In the holographic microscope, two probe beams are scanned across the mask blank, when one beam encounters a defect in the mask and the other

beam encounters a clean area of the mask, the light scattered by the defect is recorded as a hologram using the second beam as the reference.

1.4 THESIS ORGANIZATION

This thesis is concerned with the at-wavelength characterization of key components of EUV lithography systems including mask blanks, imaging optics, and an illuminator, using well-known holography techniques. The motivation for this study is to aid the development of key components of EUV lithography.

The PS/PDI as used to measure wavefront quality of EUV lithographic optics is considered in Chapter 2. Most of the study presented in this thesis is based on the PS/PDI system, so it is important to understand the basics of the PS/PDI. In Chapter 3, modification of the PS/PDI to implement a Fourier-transform holography system is introduced. The resulting 100-nm resolution aerial image recording technique used to characterize the coherent imaging performance of a prototype EUV lithographic optic is described. The coherence measurement of a synchrotron-based illuminator using the Fourier-transform holography system is presented in Chapter 4. In Chapter 5, applications of the holographic technique to characterize defects on EUV multilayer mask blanks are demonstrated. Various sized amplitude programmed defects are characterized. Finally, in Chapter 6, the results of this thesis are summarized.

Chapter 2

Phase-shifting point diffraction interferometer

2.1 INTRODUCTION 15

2.2 PHASE-SHIFTING POINT DIFFRACTION INTERFEROMETER (PS/PDI): GENERAL DESCRIPTION 17

2.3 AT-WAVELENGTH CHARACTERIZATION OF EUV PROTOTYPE LITHOGRAPHIC OPTICS 19
2.3.1 EUV light source: beamline condenser system 19
2.3.2 PS/PDI configuration 22
2.3.3 Optical system under test: 10×-Schwarzschild optics 27

2.4 INTERFEROGRAM ANALYSIS METHOD 30

2.5 RESULTS OF THE PS/PDI MEASUREMENT 32
2.5.1 Alignment of 10× optics at wavelength 35
2.5.2 Chromatic effects due to multilayer coating 36
2.5.3 Flare measurements 38
2.5.4 Comparison with visible light interferometry 39

2.6 ACCURACY OF THE PS/PDI 40
2.6.1 Systematic effects from measurement geometry 40
2.6.2 Experimental method to determine the accuracy of the PS/PDI: a null test 41
2.6.3 Analytical treatment to identify the accuracy of the PS/PDI 42
2.6.4 The lower limit accuracy of the PS/PDI 43
2.6.5 The reference-wavefront-error-limited accuracy and the systematic-error-limited accuracy of the PS/PDI 44

2.7 PS/PDI AS HOLOGRAPHY 47
2.7.1 Reconstruction of the point spread function of the 10× optical systems 49

2.8 CONCLUSION 50

2.1 INTRODUCTION

Wavefront measurements at the operational wavelength of an optical system play an important role in system performance characterization. EUV lithography's requirement for unprecedented optical quality places stringent requirements on the accuracy of interferometers used for optical metrology. Development of at-wavelength high accuracy interferometry to measure sub-nanometer wavefront errors is needed to evaluate multilayer-coated EUV lithographic optics and to help achieve nearly diffraction-limited imaging performance from these optics.

The conventional point diffraction interferometer, shown in Fig. 2-1, has been proposed to test EUV lithographic optics at wavelength. The point diffraction interferometer [34,35] enables direct measurements of wavefront aberrations at the *exit pupil* of the imaging system by interfering an unknown wavefront and a well-known reference wavefront.

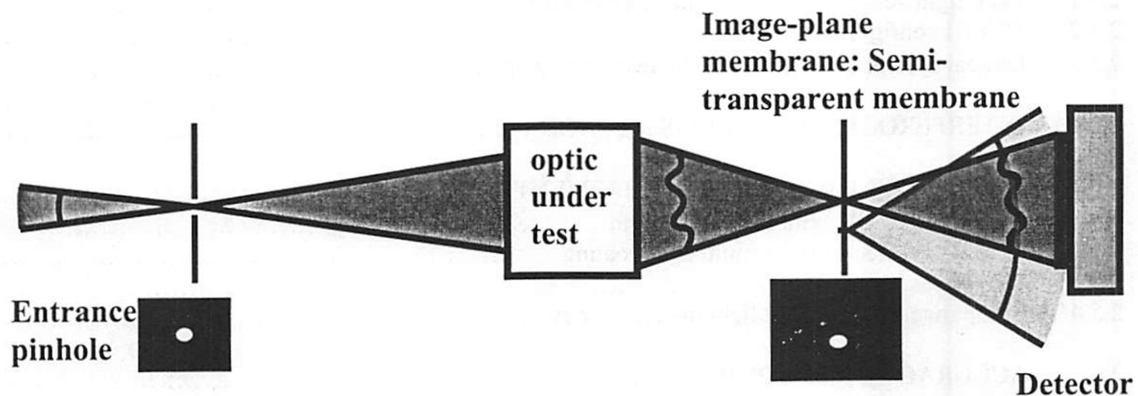

Fig. 2-1 Major components of the conventional point diffraction interferomter. The point diffraction interferometer enables direct measurements of wavefront aberrations at the *exit pupil* of the imaging system by interfering an unknown wavefront and a well-known reference wavefront.

Nearly perfect spherical illumination of the optical system under test is generated by pinhole diffraction. The perfect wavefront picks up aberration from the optical system under test. The unknown aberrated wavefront is transmitted through a thin semi-transparent membrane located near the image plane of the optical system under test. The reference wavefront is generated by diffraction from a sub-resolution pinhole (pinhole size smaller than the center lobe of the optic's point spread function) located in the same membrane. The test wavefront transmitted through the membrane and the reference wavefront diffracted from a sub-resolution pinhole interfere and generate a fringe pattern. This fringe pattern reveals the aberration of the optical system under test.

The point diffraction interferometer is applicable over a wide spectral range with high accuracy by utilizing a diffractive reference wavefront. Since the point diffraction interferometer is a common path interferometer, the coherence length requirement on the light source is relaxed. However, the power of the reference wave, as determined by the amount of flux getting through the pinhole is three to four orders of magnitude smaller than the test wave, therefore, the fringe contrast is very low. Contrast can be improved by using a strong absorbing membrane. However, in this case, the problem would be the fringe throughput.

The phase-shifting point diffraction interferometer (PS/PDI) is a common path interferometer with phase shifting capability derived from the conventional point diffraction interferometer described above [37]. The PS/PDI preserve the advantages of the conventional point diffraction interferometer while having high fringe contrast and throughput as well as a phase shifting capability. This is achieved by introducing a simple

diffraction grating in the path of the illuminating beam. This interferometer has been successfully used to evaluate numerous EUV optics at their operational wavelength [40-52].

In this chapter, the PS/PDI is rigorously described and presented from the point of view of holography.

2.2 PHASE-SHIFTING POINT DIFFRACTION INTERFEROMETER (PS/PDI): GENERAL DESCRIPTION

The conventional point diffraction interferometer described above has some practical limitations due to its low fringe contrast and lack of phase-shifting capability. The PS/PDI design preserves the advantages of the conventional point diffraction interferometer yet allows phase-shifting capability and higher throughput. Because the PS/PDI is a common-path interferometer, it is stable, resistant to vibration, and appropriate for light sources with moderate longitudinal coherence.

The configuration of the PS/PDI is depicted in Fig. 2-2(a). The PS/PDI consists of an entrance pinhole, a transmission grating, a pair of pinholes in the image-plane mask, and a CCD detector. Spatially coherent spherical wave illumination is provided by diffraction from the entrance pinhole. The transmission grating serves as a *small-angle beam-splitter* providing the test and reference beams required for the interferometry. The optic under test focuses the various grating orders to the image plane. One pinhole in the image plane generates the reference beam by spatial filtering one of the grating diffracted orders. The test beam, on the other hand, propagates, largely unaffected, through a relatively large second pinhole, or window, as shown in Fig. 2-2(a). The rest of the grating orders are blocked by the opaque membrane containing the pinholes. The test and reference beams propagate to the mixing (CCD) plane where they overlap to create an interference pattern. The

interferogram is thus a comparison of the test beam and the ideally spherical reference wave. Phase shifting can be achieved by translation of the grating, which produces a controllable relative phase-shift between adjacent diffracted orders of the grating. Translation of the grating by one grating period produces a first diffraction order phase shift of one full cycle, while the phase of the zeroth diffraction order remains fixed.

Errors in the grating line placement can be filtered if the first order of the grating is used as the reference beam. However, because the first-order beam is weaker than the zeroth order when using an amplitude grating as is done in this thesis, and because pinhole filtering can attenuate the beam significantly, using the first-order beam as the reference can lead to low fringe contrast.

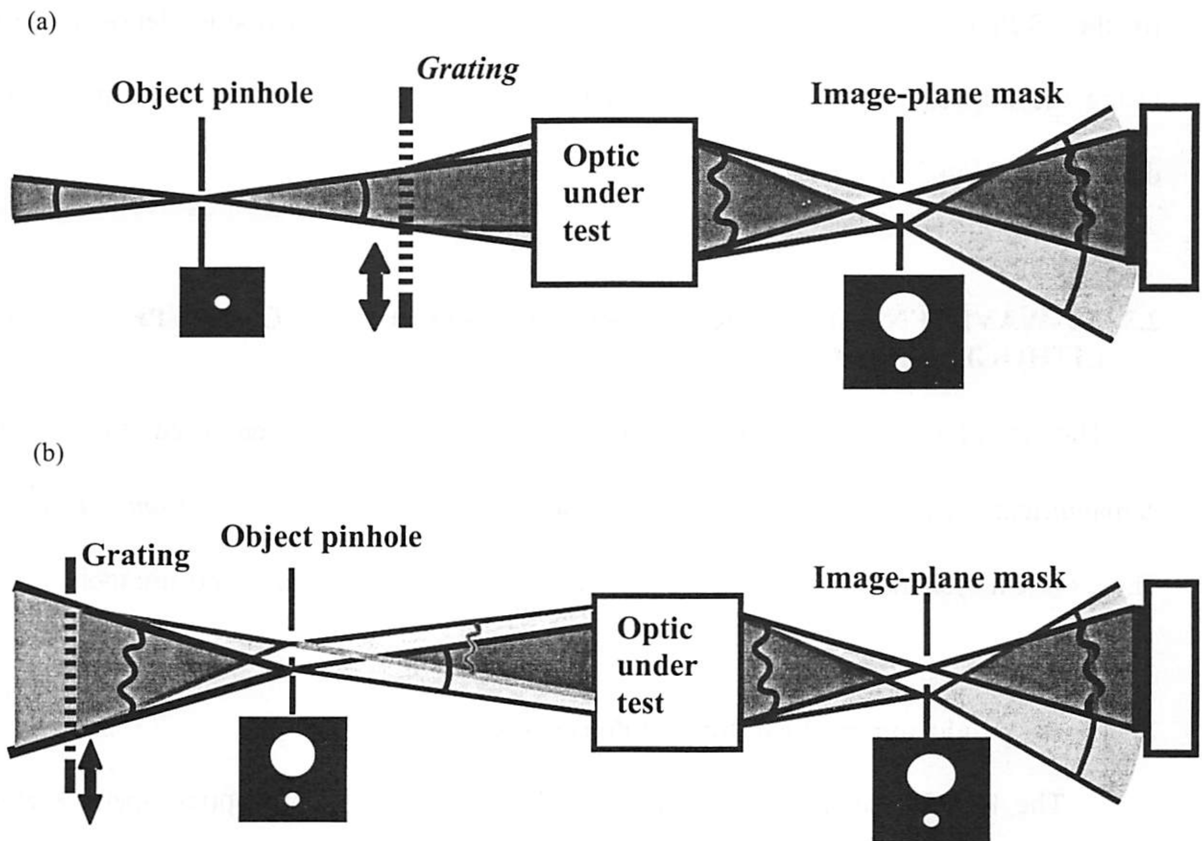

Fig. 2-2 Two different PS/PDI configurations. (a) The PS/PDI design for EUV lithographic optics testing. The grating enables phase-shifting capability as well as providing increased throughput. (b) The up-stream grating PS/PDI used in 193-nm applications. The grating is placed before the entrance pinhole to eliminate grating induced errors.

In order to improve the fringe contrast while maintaining grating line-placement error suppression, an alternate configuration of the PS/PDI [37,40,41] has been proposed with the grating placed before the object plane [Fig. 2-2(b)]. Since the reference and test beams are each spatially filtered once, fringe contrast exceeding 90% is readily achieved [40,42]. Also, the fact that the spatial filtering is performed after passage through the grating allows for the suppression of grating-line-placement errors. This design, however, is limited to use in a situation where the beam delivery system illuminating the object plane can provide a small image spot relative to the grating-induced beam separation at the object plane. This is not the case for the PS/PDI described in Fig. 2-2(a) where a synchrotron undulator beamline (discussed in section 2.3.1) is used as the beam delivery system. However, it can be the case for the PS/PDI at 193-nm where a conventional ArF laser and fused silica lenses are used. Using the upstream grating configuration (Fig. 2-2(b)), the PS/PDI at 193-nm has been demonstrated [54,55].

2.3 AT-WAVELENGTH CHARACTERIZATION OF EUV PROTOTYPE LITHOGRAPHIC OPTICS

The PS/PDI configuration described in Fig.2-2(a) has been used to test 10× demagnification, multilayer coated, Schwarzschild optical systems at *13.4-nm wavelength.* These optical systems are designed for the prototype EUV lithography exposure tools.

2.3.1 EUV light source: beamline condenser system

The PS/PDI for at-wavelength testing of EUV lithographic optics operates at the undulator beamline 12.0.1 of the Advanced Light Source (ALS) at Lawrence Berkeley National Laboratory (LBNL). The fundamental properties and description of the undulator

structure is illustrated in greater detail elsewhere [38]. The 8-cm period (λ_n) undulator magnet structure with 55 magnet periods (N) provides high-brightness EUV radiation tunable from 5 nm to 25 nm in wavelength at the beamline 12.0.1. As described in Fig. 2-3, the beamline optics include grazing incident mirrors, a grating monochromator, exit slits, and a Kirkpatrick-Baez (K-B) illuminator [38].

The acceptance half angle (numerical aperture) of the undulator radiation is set by the size of the acceptance aperture which is located 16.7 cm from the exit of the undulator, and it is approximately 48 μrad. The grazing incident monochromator selects the desired wavelength, and a K-B illuminator is used to reimage the partitially coherent EUV source to the entrance of the PS/PDI system with demagnification and serves as a condenser system. The focal plane of the condenser system (K-B system) serves as the entrance plane for various experiments. About 60× demagnification of the undulator source is achieved with the beamline optics. The K-B system illuminates the PS/PDI system with ~ 0.006 numerical aperture (NA) and generates a spot size of ~11 μm (H) × ~5 μm (V).

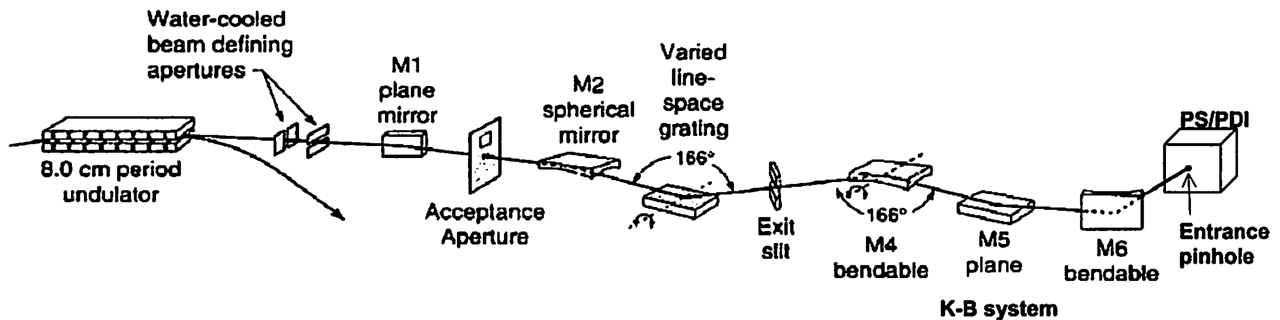

Fig. 2-3 Configuration of the beamline optics at beamline 12.0.1. Beamline 12.0.1 of the Advanced Light Source at the Lawrence Berkeley National Laboratory is used to illuminate the PS/PDI system with high flux coherent EUV radiations. The beamline optics include grazing incident mirrors, a grating monochromator, and a focusing K-B system. [Part of this figure is obtained from P.J. Batson at the Center for X-ray Optics.]

The exit slit is used to select the desired bandwidth from the grating monochromator. The natural bandwidth of the undulator is set by the number of magnet periods, $\Delta\lambda/\lambda = 1/N = 1/55$. The spectral bandwidth, $\Delta\lambda/\lambda$, as narrow as 1/1100 can be achieved by narrowing down the exit slit. The spectral bandwidth is directly related to the longitudinal (temporal) coherence of the source [57, 58], which is given by

$$l_{coh} = \frac{\lambda}{2} \cdot (bandwidth) = \frac{\lambda}{2} \cdot (\frac{\lambda}{\Delta\lambda}) \qquad \text{(Eq.2-1)}$$

where l_{coh} is the coherence length for a given spectral bandwidth. For the beamline 12.0.1, the coherence length ranges from 0.37 μm to 7.37 μm depending on the exit slit width. The PS/PDI system should not be limited by the coherence length, thus the spectral bandwidth, $\lambda/\Delta\lambda$, of 500-1000 is typically used for the PS/PDI experiments. The coherence length must be larger than the maximum optical path length difference between two point sources (For our particular case, the maximum path length difference is ~0.3μm).

In order to perform interferometry, the undulator beamline is required to deliver the spatially coherent EUV radiation to the PS/PDI system. The measured coherence area at the K-B focus is approximately 8 μm (V) × 6 μm (H) elliptical shape [56]. The measurement of the coherence area at the K-B focus is demonstrated in Chapter 4 of this thesis. An entrance pinhole with size smaller than the coherence area at the K-B focus can generate a spherical wavefront with a high degree of spatial coherence. Figure 2-4 shows an Airy pattern produced by pinhole diffraction with a 0.75-μm diameter pinhole located at the K-B focus.

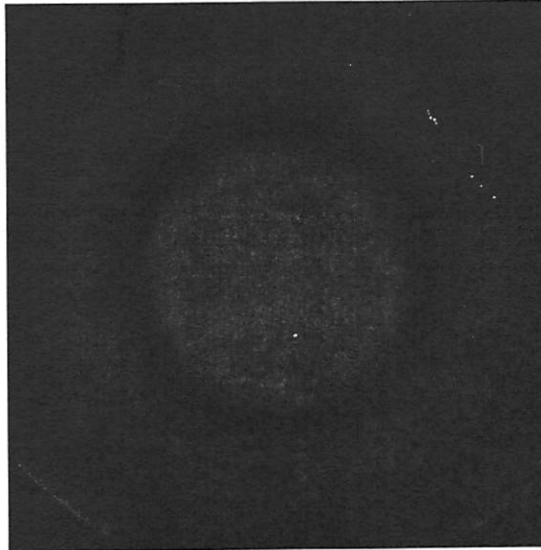

Fig. 2-4 A log scale image of diffraction pattern generated by 0.75-μm entrance pinhole at 13.4 nm. The EUV power at the K-B focus with 8μm by 5 μm elliptical shape is ~15 mW. This high contrast diffraction ring illustrates the nearly perfect spatial coherence of the diffracted beam.

This high contrast diffraction ring illustrates the nearly perfect spatial coherence of the diffracted beam.

2.3.2 PS/PDI configuration

The setup of the PS/PDI system for wavefront testing of 10×-Schwarzschild optics is depicted in Fig. 2-5(a), and a photograph of the entire experimental system is shown in Fig. 2-5(b). Detailed descriptions and specifications of the PS/PDI are presented in references [40, 41].

The system is designed to test optics in their operational vertical orientation. The vertical illumination is steered with a 45° multilayer turning mirror. The K-B condenser system described above focuses the EUV radiation to the object plane of the 10×-Schwarzschild optic, where a sub resolution (resolution in the object side of the 10× optic) entrance pinhole is located. The spatially coherent spherical wavefront is generated by

spatial filtering provided by the object-plane pinhole (entrance pinhole). The entrance pinhole is a commercially available 0.75 μm diameter laser drilled pinhole and made of 12-μm thick aluminum. The entrance pinhole is held by the kinematic 3-D translation mount, also called "Hector's Magic Flange" (HMF) [40], to help align the entrance pinhole to the K-B focus.

(a)

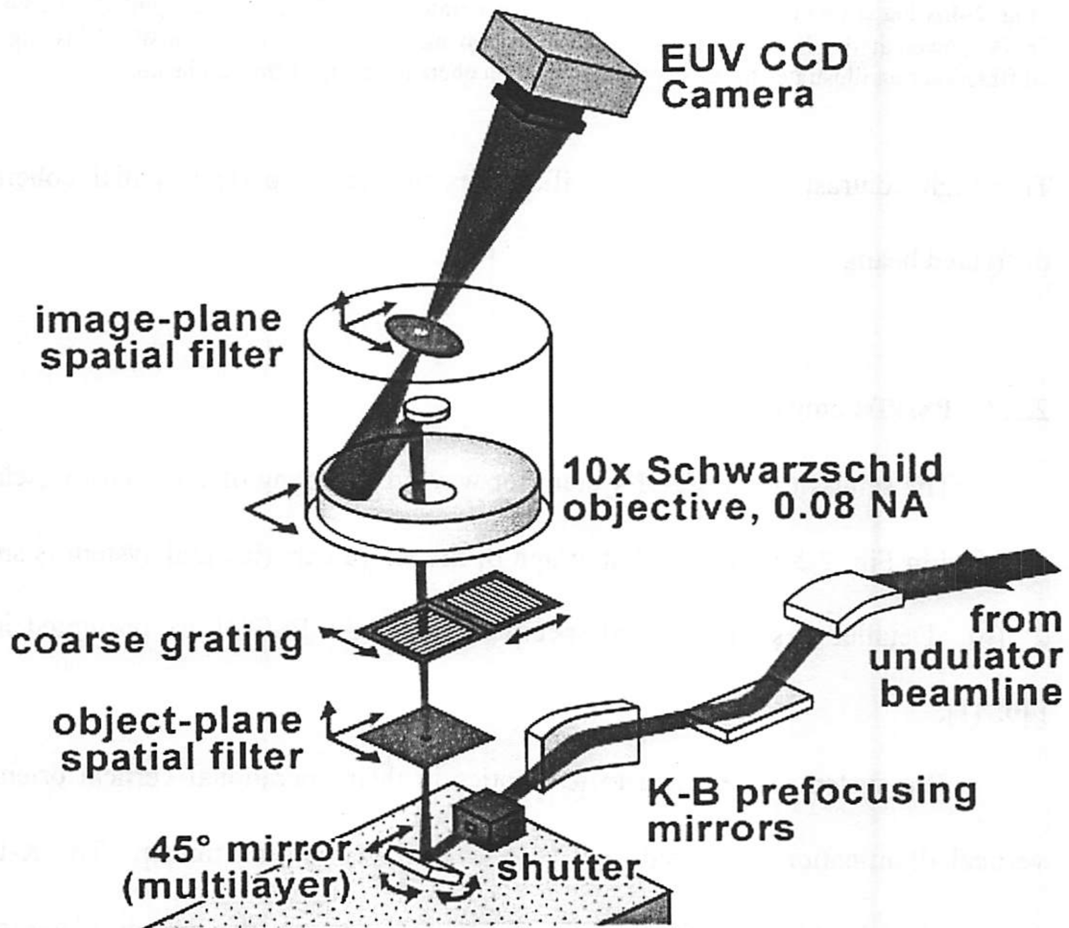

Fig. 2-5 (a) The schematic diagram of the experimental setup. The system is designed to test optics in their operational vertical orientation. The vertical illumination is steered with a 45° multilayer turning mirror. [The picture is obtained from K.A. Goldberg at the Center for X-Ray optics.]

(b)

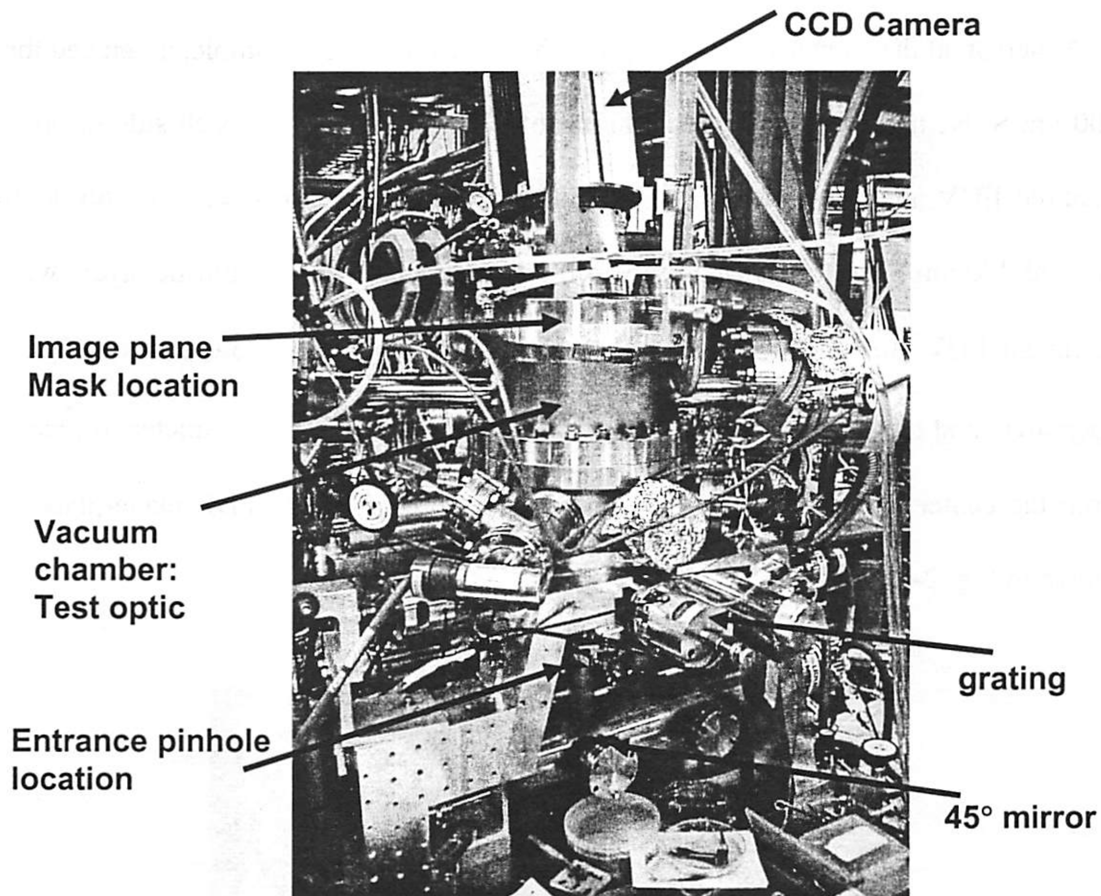

Fig. 2-5 (b) a photograph of the entire experimental system. The entire PS/PDI system described above is operated under vacuum (base pressure of ~10^{-7} torr).

A coarse grating is placed between the entrance pinhole and the test optic. The grating serves as a small angle beam splitter by diffracting the wavefront into multiple orders. The grating is typically 18-μm pitch and is made of a 225-nm thick gold absorber pattern on a 100-nm thick Si_3N_4 membrane with 5 × 5 mm^2 open area. To enable phase shifting, the grating is held with a 1-D translation stage with motion in the direction perpendicular to the grating ruling.

At the image plane of the test optic, an image-plane mask is placed. The image-plane mask contains two spatial filtering windows used to select two of the multiple diffracted orders. The mask is fabricated using electron beam lithography and reactive ion etching by E. Anderson at the Center for X-ray optics. The mask pattern is completely etched through a 100 nm Si_3N_4 membrane and then 100 nm of Ni is evaporated on each side to provide the required EUV attenuation [59-61]. EUV attenuation lengths of nickel and nitride are 34.3 nm and 270 nm respectively; therefore 200 nm Nickel and 100 nm nitride layers will give a sufficient EUV attenuation. The test beam window is typically a 3.0 μm × 3.0 μm square open area, and the reference pinhole, typically 50 nm to 150 nm in diameter, is placed 5 μm from the center of the test window. An SEM picture of the PS/PDI image-plane mask is shown in Fig. 2-6.

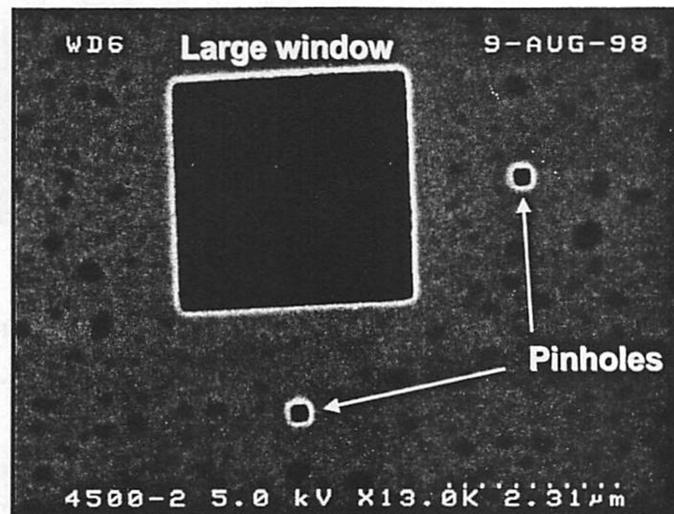

Fig.2-6 SEM picture of the image plane mask. The mask pattern is completely etched through a 1000 Å Si_3N_4 membrane and then 1000 Å of Ni is evaporated on each side. The test beam window is typically a 3.0 μm × 3.0 μm square open area, and the reference pinholes, typically 50 nm to 150 nm in diameter, are placed 5 μm from the center of the test window. There are two reference pinholes for two directional measurements depending on the grating orientation.

The test beam passes through the large window substantially preserving the aberration imparted by the test optic while the reference beam is spatially filtered by the sub resolution (resolution in the image side of the optic) pinhole. Since the test beam is compared with the spherical reference wavefront diffracted from a pinhole, the quality of the reference beam determines the ultimate accuracy of the system. The accuracy of the PS/PDI is discussed in section 2-6 of this chapter.

The interference pattern formed by the test and reference beams is recorded at the CCD (charge-coupled device) camera. The recording plane, or CCD camera plane, is located near the system exit pupil plane (approximately 3cm behind the exit pupil plane). Even though the CCD camera is not exactly placed at the exit pupil, it is close enough such that it does not significantly affect the final measurement results [40,41]. Therefore, the reconstructed phase and amplitude information from the interferograms reveal the quality of the imaging optical system under test at its exit pupil. The CCD camera is a back-illuminated, back-thinned, EUV CCD detector consisting of a 1-inch-square array of 1024 × 1024 pixels [62,63]. The dynamic range of the detector is 2^{14}= 16384 levels at the maximum scan rate of 800 kHz. The exposure time is controlled by the shutter placed after the exit slit of a beamline monochromator.

The entire PS/PDI system described above is operated under vacuum (base pressure of $\sim 10^{-7}$ torr). A small amount of oxygen ($\sim 10^{-4}$ torr) is supplied to the vacuum chamber to prevent carbon contamination of the pinholes [41]. An example of a typical interferogram obtained with the PS/PDI is shown in Fig. 2-7, along with a cross-section plot illustrating the high fringe contrast. By analyzing the interferogram, wavefront aberration of the test optics at the exit pupil of the system can be extracted.

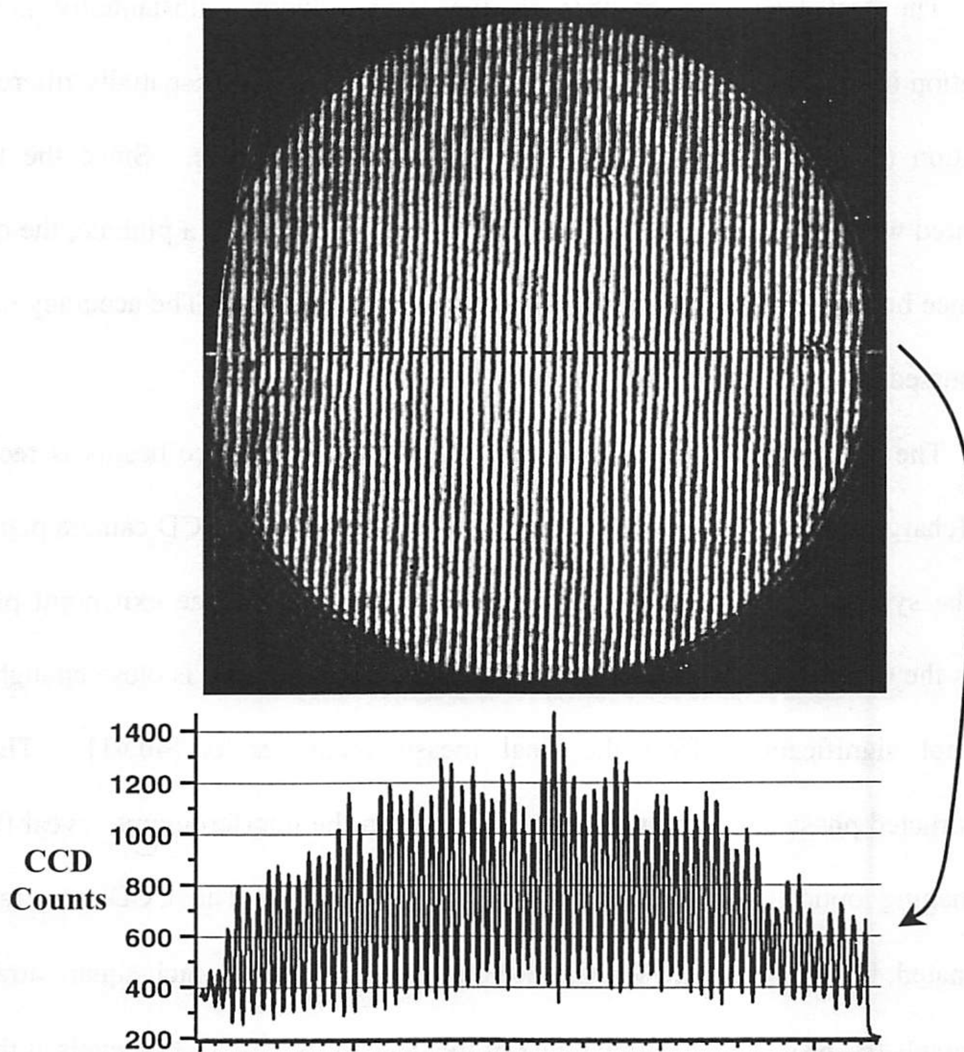

Fig. 2.7 An example interferogram obtained from the PS/PDI system along with a line out plot. This interferogram is obtained with Camera B2 optic. The numbers on the y-axis of the line out plot correspond to the counts on the CCD camera. [The cross-section plot is provided by K.A. Goldberg at the Center for X-ray optics.]

2.3.3 Optical system under test: 10X-Schwarzschild optics

The PS/PDI described here has been designed to test Schwarzschild optical systems. These two-mirror, 10× demagnification optical system are extensively used as EUV lithography research and development tools. The design and photograph of a 10X Schwarzschild optic is shown in Fig. 2-8 (a) and (b) respectively. The detailed design

parameters and specifications are discussed elsewhere [64]. The Schwarzschild optic consists of two concentric spherical mirrors, primary and secondary mirrors. Both mirrors are coated with 40 Mo/Si multilayer pairs optimized for 13.4 nm wavelength operation. In order to compensate for varying incidence angles, the primary mirror is coated with a graded multilayer.

The full NA of the 10×-Schwarzschild optics is approximately 0.29. However, for lithography, these optics are typically used with only off-axis sub-apertures with NAs ranging from 0.06 to 0.088. The off-axis NA is determined by an aperture plate on the primary mirror. The smaller sub-aperture is used in order to minimize wavefront aberrations over a larger field of view than could be obtained using the full annular aperture. This system with 0.08 NA has a theoretical resolution limit for dense features of about 100 nm. The corrected field size is ~400-μm in diameter in the image plane.

Since the PS/PDI has been implemented, it has been used to test five different EUV 10×-Schwarzschild optics (10×I, 10×-Berkeley, Camera A, Camera B1, and Camera B2 in chronological order of their fabrication). They have the exact same design but the substrate finish and coating quality vary.

The 10×I optic is the original optic used in the 10×-microstepper developed at the Sandia National Laboratory for initial studies of EUV lithography [64]. 10×I optic was fabricated in 1993-1994, and the multilayer coatings were done at AT&T Bell Laboratories.

The 10×-Berkeley was used in the initial development of the EUV PS/PDI system. Subsequently, 10× - Berkeley optic was used to perform high quality EUV imaging experiments at Sandia National Laboratory (SNL). This optic was fabricated in 1994 and also coated at AT&T.

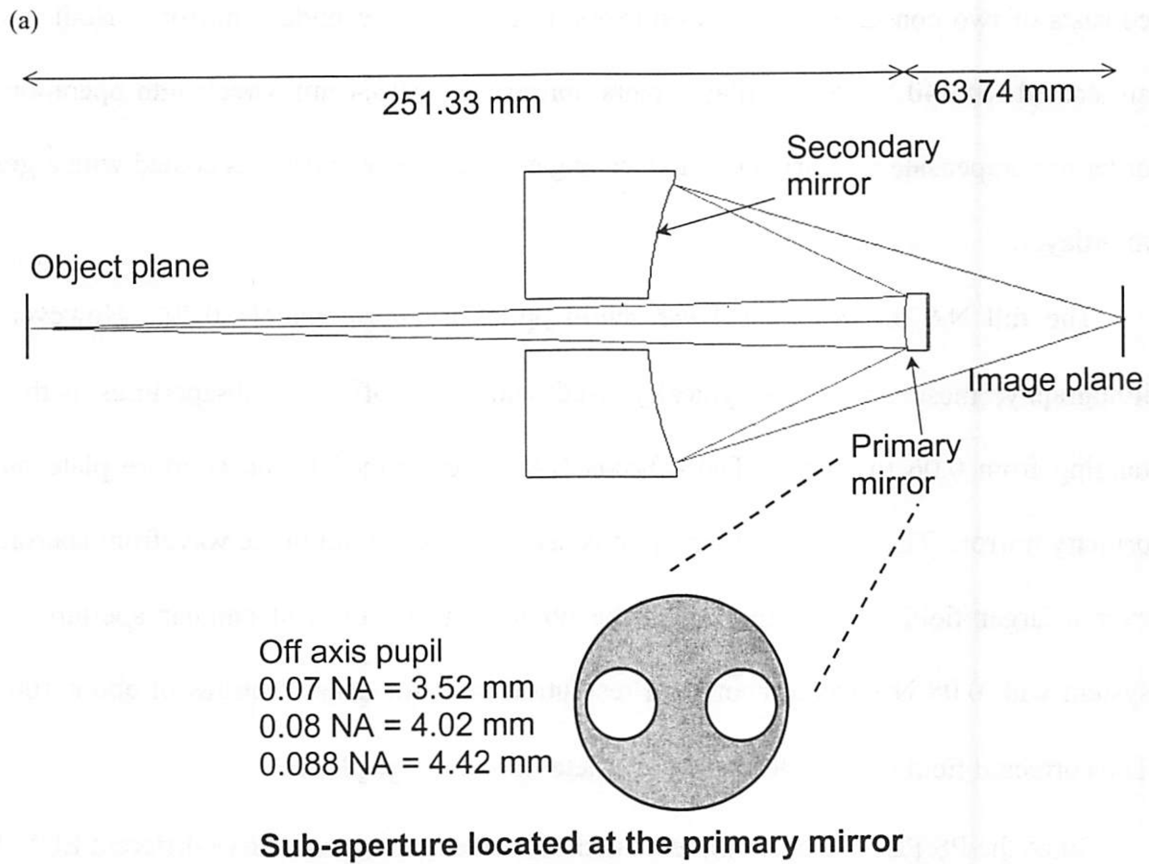

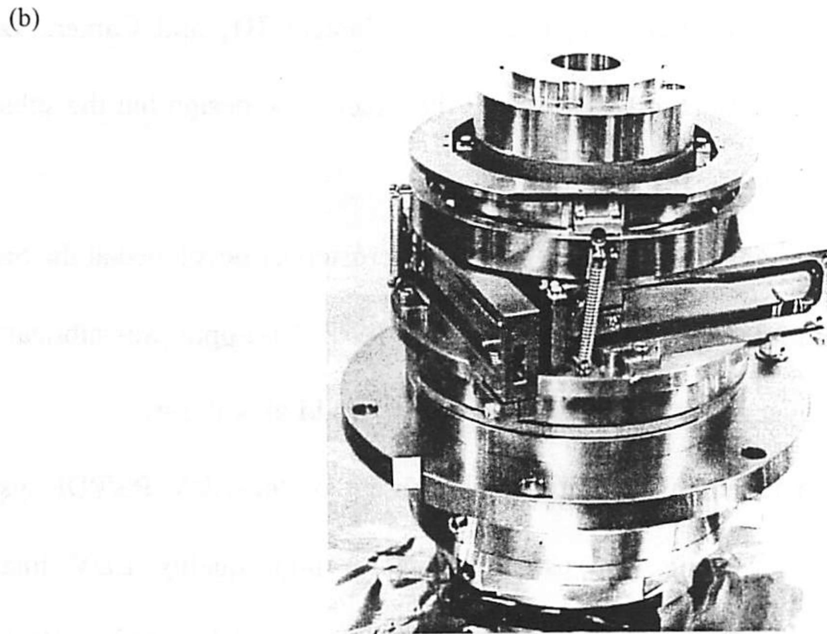

Fig. 2-8 (a) Design of 10× Schwarzschild optics. The full aperture NA is 0.29. These optics are typically used with off-axis subapertures limiting the NA to less than 0.088. (b) A photograph of a 10×-Schwarzschild optic.

Camera A was more recently fabricated and designed to meet the figure specifications of the Projection Optics Box (POB), which is the 4 mirror EUV optic to be used in the first α-class EUV stepper [65]. This optic was fabricated in 1997-1998 and coated at Lawrence Livermore National Laboratory (LLNL).

Camera B1 and Camera B2 are the most recently fabricated optics developed to meet both the figure *and* finish specifications of the Projection Optics Box (POB). These optics were fabricated in 1998 and also coated at Lawrence Livermore National Laboratory. Both optics are currently used in the two EUV microsteppers installed at SNL [66]. Features as small as 50 nm have been printed in the photoresist with these high quality optics.

2.4 INTERFEROGRAM ANALYSIS METHOD

Various methods exist for extracting wavefront data from recorded interferograms. The detailed descriptions of interferogram analysis methods are rigorously described in the references [40,41,67]. The two most common methods are Fourier-fringe analysis and temporal phase-shifting analysis methods.

The recorded interferogram can be mathematically written as

$$I(x,y) = I_1(x,y) + I_2(x,y) + 2I_3(x,y) \cdot \cos(2\pi \overline{f}_c \cdot \overline{x} + \Phi(x,y) + \Delta) \qquad \text{Eq. 2-2a}$$

$$I_3(x,y) = \sqrt{I_1(x,y)} \cdot \sqrt{I_2(x,y)} \qquad \text{Eq. 2-2b}$$

where I_1 and I_2 are intensities of the reference and the test waves respectively, $\Phi(x,y)$ is the phase aberration in the test beam, and Δ is the arbitrary constant phase term. Eq. 2-2a can be rewritten as

$$I(x,y) = I_1 + I_2 + \text{Re}[I_3 \cdot e^{i\Phi(x,y)} \cdot e^{i(2\pi \bar{f}_c \cdot \bar{x} + \Delta)} + I_3^* \cdot e^{-i\Phi(x,y)} \cdot e^{-i(2\pi \bar{f}_c \cdot \bar{x} + \Delta)}] \qquad \text{Eq. 2-3}$$

The Fourier-fringe analysis method involves taking Fourier transform of Eq. 2-3 from space domain to spatial frequency domain, allowing the $I_3 \cdot e^{i\Phi(x,y)}$ term to be readily extracted by virtue of it being modulated onto a spatial carrier. After extracting the necessary term, it is trivial to get the wavefront aberration, *Φ(x,y)*, by way of inverse Fourier transform back to space domain. As is evident, this technique can be performed using a single interferogram but requires a spatial carrier.

Alternatively, a phase-shifting technique can be used to retrieve wavefront aberrations from multiple interferograms with known constant phase terms, Δ. In this case, the spatial carrier is not necessary, however, by design the PS/PDI system always has a spatial carrier. This method requires varying the relative phase shift between the test and reference wavefront. In the PS/PDI, this is achieved by translating the beam-splitting grating. For example, recording four interferograms in sequence with π/2 phase shift under constant experimental conditions, each interferogram becomes Eq.2-2a or Eq. 2-3 with Δ of 0, π/2, π, and 3π/2. In this case, the phase term, *Φ(x,y)*, can be extracted as follows:

$$\tan(\Phi(x,y)) = \frac{I(x,y,\Delta = \frac{3\pi}{2}) - I(x,y,\Delta = \frac{\pi}{2})}{I(x,y,\Delta = 0) - I(x,y,\Delta = \pi)} \qquad \text{Eq.2-4}$$

$$\Phi(x,y) = \tan^{-1}\left(\frac{I(x,y,\Delta = \frac{3\pi}{2}) - I(x,y,\Delta = \frac{\pi}{2})}{I(x,y,\Delta = 0) - I(x,y,\Delta = \pi)}\right) \qquad \text{Eq.2-5}$$

As seen in Eq.2-4 and 2-5, the common intensity terms are canceled out, and no Fourier transforms are required for the phase-shifting method. However, the accurate control of the phase steps and intensity are challenging problems for the phase-shifting method [40,41]. Many different algorithms for the phase-shifting method can be devised for specific applications [67]. Primary advantages for the phase-shifting method are improved accuracy, robustness, and high sensitivity compared to the single interferogram Fourier-fringe analysis method.

After obtaining the wavefront information, phase unwrapping will be required, if the phase variations exceed 2π. The analysis methods described above produce a modulo-2π version of the wavefront phase map. To find the continuous wavefront information, the 2π phase jumps must be resolved. After phase unwrapping, the wavefront phase maps are often fitted to a set of Zernike polynomials [67].

2.5 RESULTS OF THE PS/PDI MEASUREMENT

The EUV PS/PDI measurement results of the five 10×-Schwarzschild optics [40-52] are summarized in Figs. 2-9 through 13. Column (a), (b), and (c) in Figs. 2-9 through 13 show EUV transmitted intensities, example interferograms, and wavefront phase maps, respectively. The wavefront results are based on the temporal phase-shifting analysis method. A summary of the measurement results is listed in Table 2-1. The measurements cover an NA of 0.08 for 10×-I, 0.07 for 10×-Berkeley, and 0.088 for Camera A, Camera B1 and Camera B2. The 10×-I optic has the lowest wavefront quality (wavefront error of 2.2nm rms), whereas the best wavefront qualities are observed with the two most recently fabricated

optics, Camera B1 and B2 (wavefront error of less than 0.6nm). As substrate finish and multilayer coating techniques develop over the time, the wavefront quality of the EUV optics continues to improve.

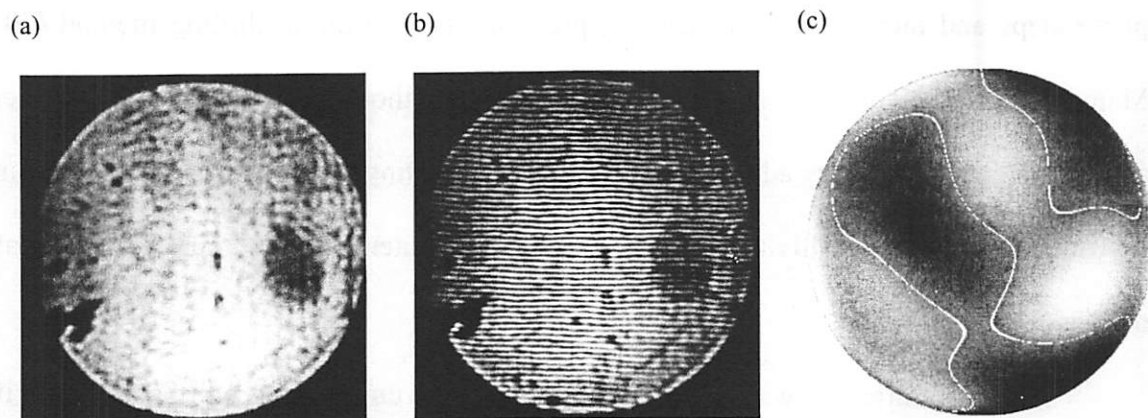

Fig. 2-9 (a) Transmitted intensity image, (b) example interferogram, and (c) resulting wavefront phase map for 10×I optic. Numerous small defects and blemishes are revealed in the transmitted intensity image. A number of long scratches which may be the by-products of the polishing technique used in the preparation of the substrates are observed for the 10×-I optic. The phase-shifting interferogram analysis method has been used to identify the wavefront aberrations. The 10×-I reveals the lowest wavefront quality (wavefront error of 2.2nm rms).

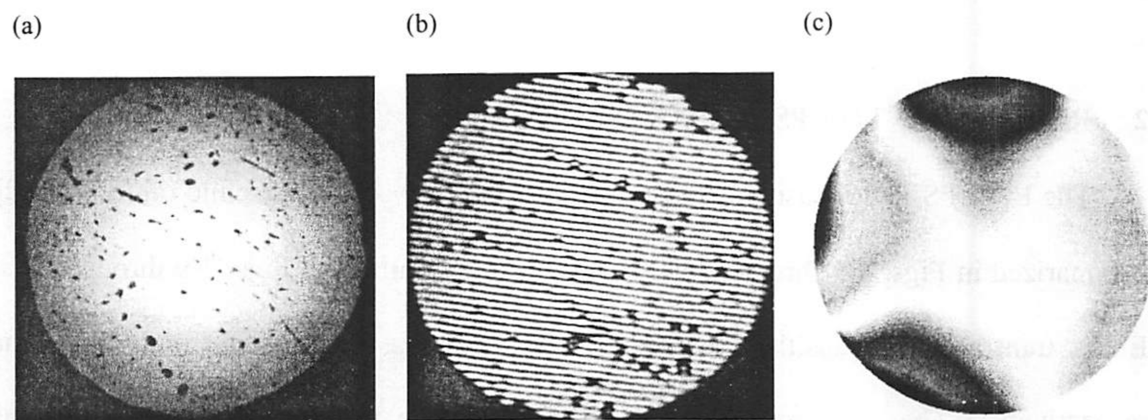

Fig. 2-9 (a) Transmitted intensity image, (b) example interferogram, and (c) resulting wavefront phase map for 10×Berkeley optic. 10×-Berkeley contains numerous small, 100-μm scale defects, which are probably due to residue from a wet cleaning process. The phase-shifting interferogram analysis method has been used to identify the wavefront aberrations. 10×-Berkeley reveals the wavefront error of 1.2nm rms over 0.07NA.

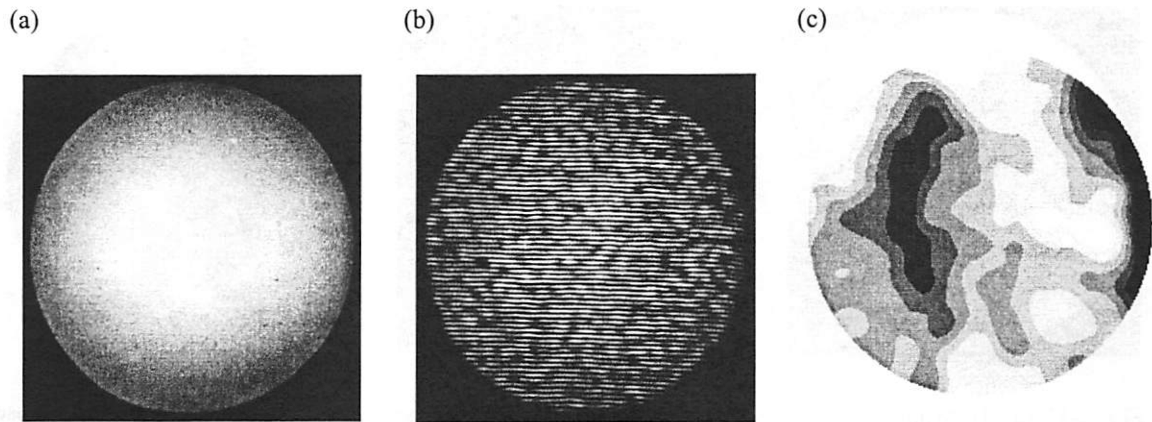

Fig. 2-10 (a) Transmitted intensity image, (b) example interferogram, and (c) resulting wavefront phase map for Camera A optic. The clean transmitted intensity image indicates the substrate polish and finish are better than 10X-I and 10X-Berkeley optics. The phase-shifting interferogram analysis method has been used to identify the wavefront aberrations. Camera A reveals the wavefront error of 0.99 nm rms over 0.088NA.

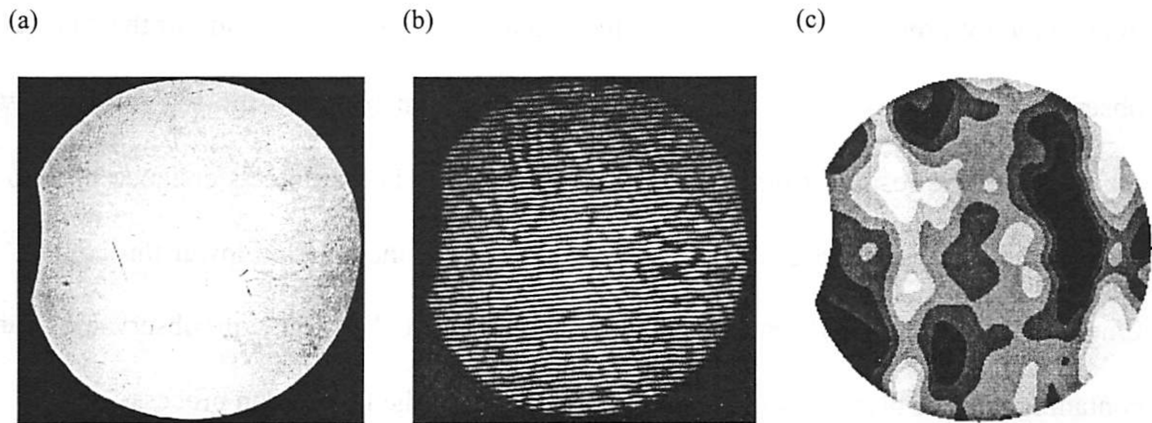

Fig. 2-11 (a) Transmitted intensity image, (b) example interferogram, and (c) resulting wavefront phase map for Camera B1 optic. The clean transmitted intensity image again indicates the substrate polish and finish are better than 10X-I and 10X-Berkeley optics. The phase-shifting interferogram analysis method has been used to identify the wavefront aberrations. Camera B1 reveals the wavefront error of 0.62 nm rms over 0.088NA.

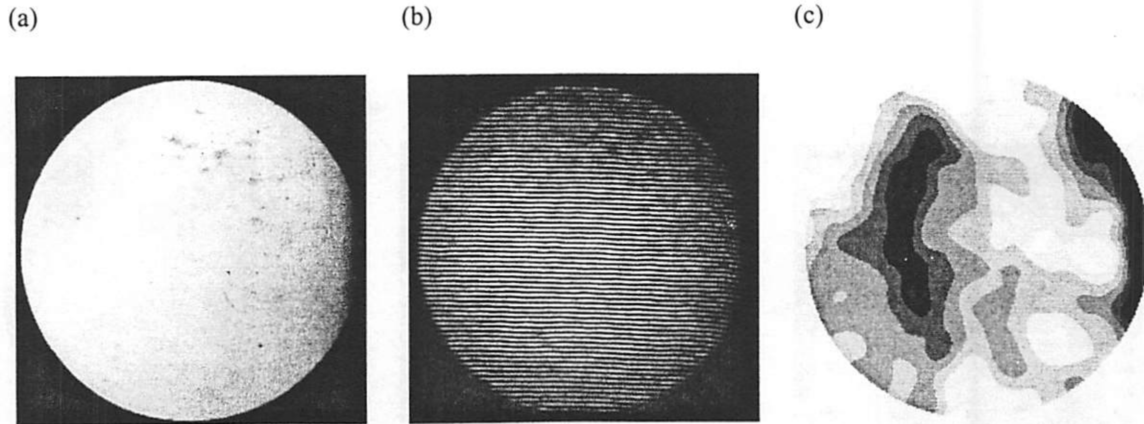

Fig. 2-12 (a) Transmitted intensity image, (b) example interferogram, and (c) resulting wavefront phase map for Camera B2 optic. The clean transmitted intensity image indicates the substrate polish and finish are better than 10X-I and 10X-Berkeley optics. The phase-shifting interferogram analysis method has been used to identify the wavefront aberrations. Camera B2 reveals the wavefront error of 0.60 nm rms over 0.088NA.

Numerous small defects and blemishes are revealed in the transmitted intensity images of the 10×-I and 10×-Berkeley optics [Figs. 2-9(a) and 2-10(a)]. A number of long scratches which may be the by-products of the polishing technique used in the preparation of the substrates is observed for the 10×-I optic. 10×-Berkeley contains numerous 100-μm scale defects, which are probably the residue from a wet cleaning process. These defects enhance high to mid spatial frequency scattering and result in lower contrast imaging and lower throughput. The Camera A, Camera B1, and Camera B2 are virtually free of observable surface contaminations or blemishes indicating improvement of the fabrication process.

2.5.1. Alignment of 10X optics at wavelength

One use for interferometry is to support final alignment of the optics for best imaging performance [71]. The EUV PS/PDI has been used for this purpose.

Mirror alignment adjustments are made via two screws that control the tilt of the primary mirror. Misalignment of the primary mirror introduces astigmatic error to the final

wavefront [51]. The wavefront error minimization is achieved by steering the primary mirror until the astigmatism error is minimized. The wavefront of Camera B2 before alignment is shown in Fig. 2-14(a), and its imaging performance is shown in Fig. 2-14(b). After aligning the optic based on PS/PDI measurements such that the astigmatism is minimized, the final wavefront quality is dramatically improved. The improved wavefront map for Camera B2 is shown in 2-15(a) and its improved imaging result of 100-nm elbow patterns is shown in Fig. 2-15(b).

2.5.2. Chromatic effects due to multilayer coating

In addition to measuring wavefront qualities, the PS/PDI may be used to characterize chromatic wavefront effects [40-41, 45-46, 50]. Because the mirrors are coated with multilayers, it allows reflections for certain bandwidth [19,68]. For 40 bilayer multilayer coatings, the bandwidth ($\Delta\lambda$) is ~0.6 nm. The wavefront quality for the optic within the bandwidth should stay the same in the presence of high quality multilayer coating.

The EUV PS/PDI has the ability to separate substrate effects from coating effects by probing the system wavefront as a function of wavelength. The tunable undulator source described in section 2.3.1 has been used to scan the operational wavelengths from 13.0 to 13.8 nm. If the difference in the measured wavefronts for different wavelengths within the bandwidth of the multilayer coating is small, it indicates the wavefront error is mostly from the substrate. Particularly, for Camera B1 and B2, small chromatic effects indicate high quality multilayer coatings, and most of the wavefront errors are from the substrates [50]. The coating–induced errors are much larger for older optics like 10×-I and 10×-Berkeley,

indicating that the wavefront errors come from combinations of the substrate and multilayer coating quality [40].

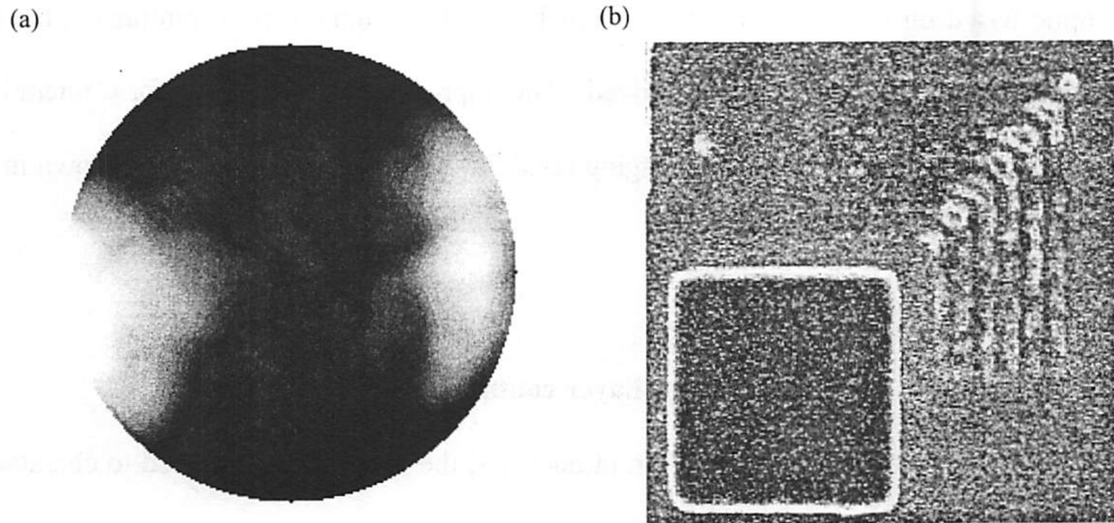

Fig. 2-14 (a) Wavefront map before alignment of Camera B2. The wavefront error of 2.38nm rms and 2.31 nm rms astigmatism errors have been measured over 0.088NA. (b) The imaging results with the before-alignment optic. The 100-nm elbow pattern is not printed on the photoresist. [The SEM picture is provided by SNL]

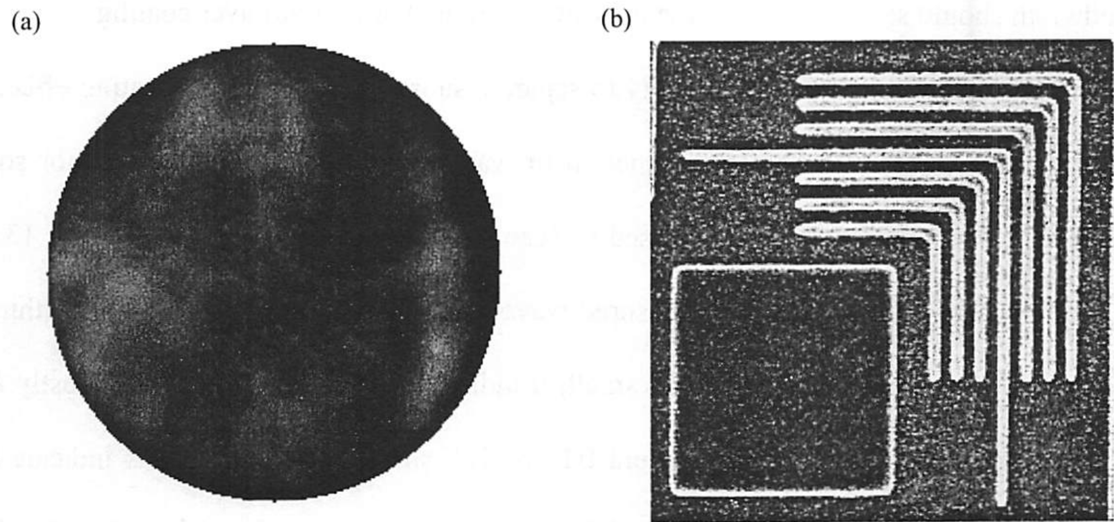

Fig. 2-15 (a) Wavefront map after alignment of Camera B2. The wavefront error of 0.6 nm rms and 0.03 nm rms astigmatism errors have been measured over 0.088NA. (b) The imaging results with the after-alignment optic. The 100-nm elbow pattern is clearly printed on the photoresist. [The SEM picture is provided by SNL]

2.5.3. Flare measurements

The capability of the PS/PDI has recently been extended to measuring both the wavefront quality and flare of optics [50,72]. "Flare" refers to light scattering within the imaging optics field of view, which affects the image contrast and line edge roughness at the image plane. It originates from mid-spatial frequency mirror surface roughness (1 μm to 1 mm period surface roughness), and it can be characterized if the wavefront metrology data from the PS/PDI contains enough spatial frequency bandwidth [72]. The measurement bandwidth is simply determined by the size of the image plane test window. Using a dual-domain method, along with an extended image plane window, it is possible to measure flare with the PS/PDI [73]. Flare is as important as wavefront quality (the low-spatial frequency contents) in lithographic systems, and it determines the imaging contrast of the optic.

Flare measurement results for the three most recently fabricated 10×-Schwarzschild optics are listed in Table 2-2. Camera B1 and Camera B2 were developed to meet a flare specification of less than 5 % in a 4-μm line [66], and results show that this specification goal has been met. Camera A, on the other hand, which had no flare specification, was measured to have 30 % flare.

10× optics	Flare in a 4-μm line (%)	Numerical Aperture (NA)
Camera A	30	0.088
Camera B1	3.9	0.088
Camera B2	3.2	0.088

Table 2-2 Flare results of three recently fabricated 10X Schwarzschild optical system. The flare has been measured with the modified PS/PDI system. Camera A has the largest flare amount. Camera A and B satisfies the finish requirements as lithographic optical systems.

2.5.4. Comparison with visible light interferometry

As a more commercially viable alignment tool, a visible light interferometer, the phase-shifting diffraction interferometer (PSDI), has been developed at LLNL [69,70]. Under the condition that the multilayer coating is nearly perfect, the visible light interferometer can successfully measure wavefront quality of EUV optics with extremely high accuracy [69, 70]. The EUV PS/PDI has played a crucial role in the calibration and validation of the visible light PSDI.

Cross-comparison experiments have shown favorable agreement between EUV and visible-light wavefront measurements in three separate 10× optics. For Camera A, Camera B1, and Camera B2, rms differences of less than 0.5 nm and peak-to-valley differences of less than 6.0 nm between the visible light interferometer and the EUV PS/PDI have been reported [52]. Considering the alignment difficulties for both interferometers, these results are within the current experimental error budget and indicate high accuracy of both interferometers [52].

The visible light interferometer clearly has advantages over the EUV PS/PDI in optical shop testing, due to its compact size, easy access, and non-vacuum operational condition. Other advantage of the visible light interferometer is its greater convenience in testing to test single and uncoated elements. However, unlike the EUV PS/PDI, the visible light interferometer requires extremely high accuracy in measuring wavefront quality due to its large operational wavelength (λ = 532 nm). The EUV wavefront is determined both by geometric figure of the substrates and multilayer coating qualities. The visible light tends to reflect from the surface of the multilayer mirror, thus it cannot see the phase effects of multilayer coating. If the multilayer coating is not perfect, the visible interferometer results

may lead to incorrect wavefront measurements. For this reason, at wavelength interferometry is a more complete tool to test EUV lithographic optics.

2.6 ACCURACY OF THE PS/PDI

Significant effort has been directed towards the accuracy characterization of the PS/PDI [40,74-76]. The main principle of Point Diffraction Interferometry is the generation of the reference wavefront by pinhole diffraction. By investigating the quality of the reference wavefront over the measurement numerical aperture (NA), the accuracy of the interferometry can be identified. As a general principle, a higher quality spherical wavefront within a given NA can be achieved by using smaller pinholes. However, determination of the accuracy with a given pinhole size needs more rigorous study.

The accuracy of wavefront measuring interferometers such as the PS/PDI is limited by several factors; the two most important factors are systematic and random errors from the quality of the reference beam and systematic effects from the measurement geometry [74]. The systematic effects from the measurement geometry can, in principle, be easily identified and removed, while the error from the reference wavefront is a more difficult problem. The accuracy of the PS/PDI, which largely depends on the quality of the reference wavefront, can be identified with experiments and simulations [74-76].

2.6.1 Systematic effects from measurement geometry

When interfering two laterally displaced spherical wavefronts, a hyperbolic fringe pattern is obtained. This hyperbolic fringe pattern results in apparent coma error in the reconstructed wavefront since a plane-wave reference is normally assumed [75]. By

knowing the lateral separation of two wavefronts and measurement NA, the geometric coma can be identified and removed. The geometric coma is given by $0.17s \cdot NA^3$ for a two beam separation of s. For example, 0.031λ coma error is expected for 5-μm pinhole separations and 0.08 NA measurement geometry.

Another geometrical error may arise from CCD camera tilt with respect to the optical axis of the system, and this leads to astigmatism in the reconstructed wavefront [75]. Careful mechanical alignment of the CCD can eliminate this geometrical error.

2.6.2 Experimental method to determine the accuracy of the PS/PDI: a null test

The accuracy of the PS/PDI depends on the quality of a single reference wavefront, but it is almost impossible to measure a single reference wavefront. The closest form of measuring a reference wavefront quality is a null test in which two similar wavefronts are compared. Such a null test, used to identify the systematic and random errors of the PS/PDI, has recently been performed.

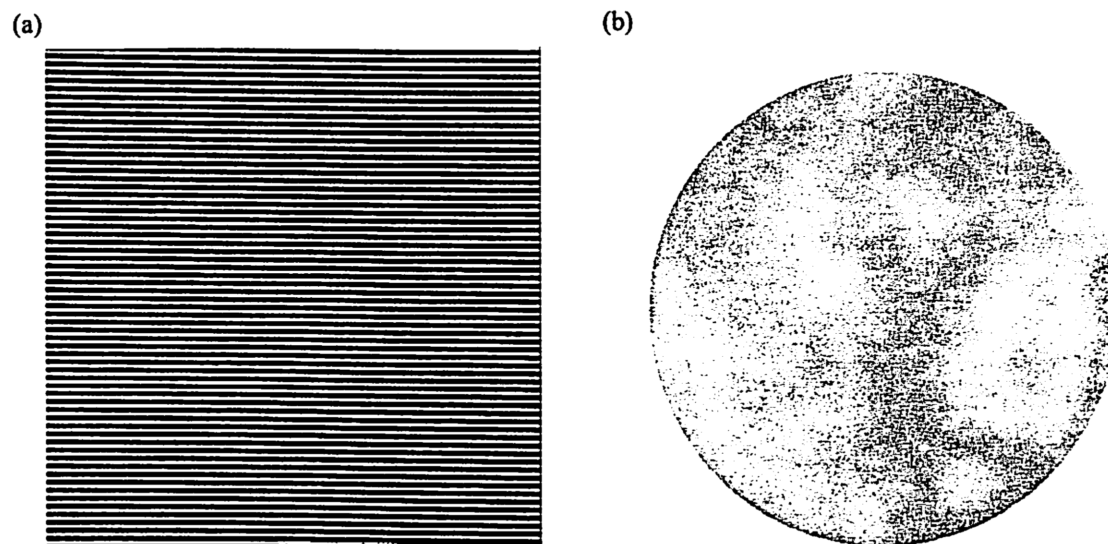

Fig. 2-16 (a) Null-test interferogram. Extremely straight fringe pattern reveals high accuracy of the PS/PDI. (b) Reconstructed wavefront map. Approximately 0.5-Angstrom wavefront error has been measured after subtracting the geometric effects.

In order to perform the null test, the image-plane mask in the PS/PDI, which contains a large window and a sub-resolution pinhole as shown in Fig. 2-5(a), is replaced with a two-pinhole mask containing two sub-resolution pinholes. In the null experiments, two high quality spherical wavefronts generated by pinhole diffraction, instead of the test and reference waves as the conventional PS/PDI experiments, interfere at the CCD. If the diffracted spherical wavefronts are perfect, the resulting interferogram should give nearly zero wavefront errors after subtracting the geometric effects discussed in section 2.6.1. Thus, the interfering fringe patterns reveal the accuracy of the PS/PDI. The extremely straight fringes from interfering two high quality spherical wavefronts is shown in Fig. 2-16(a) and the resulting wavefront phase map is shown in Fig. 2-16(b). The null test demonstrated the PS/PDI to have a *systematic-error-limited accuracy* of 0.0028 waves (0.0038 nm or $\lambda/357$) after removing the systematic effects from the measurement geometry [75]. The 10×-I optic with wavefront error of 0.164λ rms over 0.08 NA was used for this experiment.

2.6.3 Analytical treatment to identify the accuracy of the PS/PDI

As mentioned above, the accuracy of the PS/PDI is mostly determined by the quality of the single reference wavefront. In addition to experimental measurements, investigation of the single reference wavefront was performed through scalar diffraction calculations and computer simulations (TEMPEST simulation tool) [76].

A scalar diffraction calculation is used for the first approach of the pinhole diffraction problem. Even though this method simplifies some physical parameters, it yields a

reasonable first-order approximation of pinhole diffraction using Fraunhofer far-field diffraction theory [77].

More complete studies of the pinhole diffraction problem are based on computer simulations using the TEMPEST modeling package. In TEMPEST, the Maxwell equations are solved by the finite difference time-domain (FDTD) method, where the electric and magnetic field nodes are spatially and temporally staggered over a three dimensional topography of interest [78-79]. The 3-D pinhole structure and inclusion of the polarization of the incident light, which are neglected in the scalar diffraction calculation, motivate the use of TEMPEST for pinhole-diffraction calculations. Simulation treatment addresses diffraction through pinholes in a highly absorptive medium with a cylindrical shape that serves as a reasonable physical models for the experimental pinholes used in the EUV PS/PDI. The TEMPEST simulations use realistic 3-D pinhole dimensions and input fields derived from the PS/PDI results for the measured wavefront characteristics of the 10× optics.

2.6.4 The lower-limit accuracy of the PS/PDI

Assuming the pinhole location to be at the center of the focal spot, the *lower-limit reference wavefront error* of the PS/PDI can be obtained. Deviation of the pinhole position from the center of the Airy pattern is expected to introduce more errors to the diffracted wavefront, thus the pinhole located exactly at the center of the spot represents

the highest accuracy condition. Table 2-3 summarizes the *lower-limit reference wavefront error* obtained from the TEMPEST simulations and the scalar diffraction calculations as a function of the effective pinhole size, and the corresponding plot is shown in Fig.2-17. The square and triangle marked lines represent TEMPEST simulation results and scalar

diffraction calculations, respectively. The PS/PDI accuracy goal is ~ 0.01 waves (λ/100) [29]. In order to meet this accuracy goal, the calculations show that the largest pinhole size that can be used in the PS/PDI image-plane mask is about 160 nm for measurement over 0.08 NA. The accuracy obtained by the simple case can be used to select the maximum pinhole size to satisfy the desired accuracy for the given test optic.

Effective pinhole size (nm)	Lower-limit reference wavefront error (wave) from TEMPEST simulations	Lower-limit reference wavefront error (wave) from scalar diffraction calculations
60	0.0003 ±0.0001	0.0001 ±0.0001
70	0.0004 ±0.0001	0.0002 ±0.0001
80	0.0005 ±0.0002	0.0006 ±0.0001
100	0.0010 ±0.0003	0.0010 ±0.0002
120	0.0020 ±0.0004	0.0030 ±0.0003
140	0.0030 ±0.0004	0.0050 ±0.0005
150	0.0050 ±0.0006	0.0080 ±0.0007
160	0.0080 ±0.0010	0.0100 ±0.0010

Table 2-3 Summary of the lower-limit accuracy obtained from the scalar diffraction calculations and TEMPEST simulations. Assuming the pinhole location to be at the center of the focal spot, the *lower-limit reference wavefront error* of the PS/PDI can be obtained. In order to meet the minimum accuracy goal, the pinhole size smaller than 160 nm has to be used in the PS/PDI.

2.6.5 The reference-wavefront-error-limited accuracy and the systematic-error-limited accuracy of the PS/PDI

The *reference-wavefront-error-limited accuracy* is the accuracy of the PS/PDI determined solely by the quality of a single reference wavefront. The *reference-wavefront-error-limited accuracy* is considered to be the ultimate accuracy of the system if other sources of errors are ignored. The *reference-wavefront-error-limited accuracy* has been characterized in simulations by placing the pinhole near the focal spot and identifying the diffracted wavefront quality.

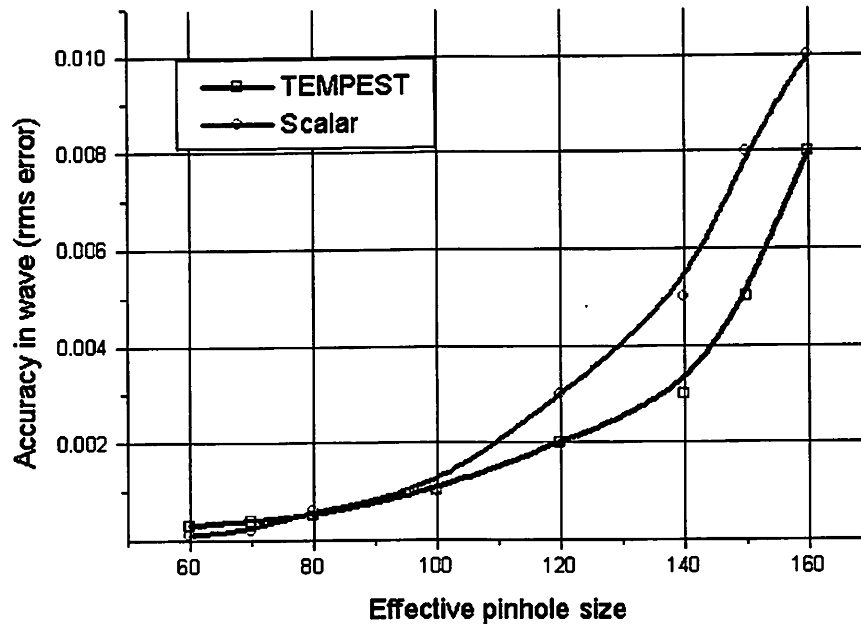

Fig. 2-17 The plot of the *lower-limit reference wavefront error* of the PS/PDI obtained from the scalar diffraction calculations and TEMPEST simulations.

Multiple simulations and calculations as a function of pinhole position and size have been performed, and the averaged results are listed in Table 2-4 for 80-nm, 100-nm, 120-nm, and 140-nm effective pinhole sizes. According to the *reference-wavefront-error-limited accuracy* results, approximately $\lambda/200$ accuracy can be achieved with the 140-nm pinhole size, and accuracy of $\lambda/500$ over 0.08 NA is possible with 100-nm pinhole size. The corresponding plot of the *reference-wavefront-error-limited accuracy* is shown in Fig. 2-18, and the square and triangle marked lines represent TEMPEST simulation results and scalar diffraction calculations, respectively.

The *systematic-error-limited accuracy* is the accuracy obtained from the null test. The null test can be also simulated with TEMPEST and scalar diffraction calculation to obtain simulated *systematic-error-limited accuracy* results. In simulations, two diffracted

wavefronts generated by the same sized and randomly located pinhole pair generate interferograms.

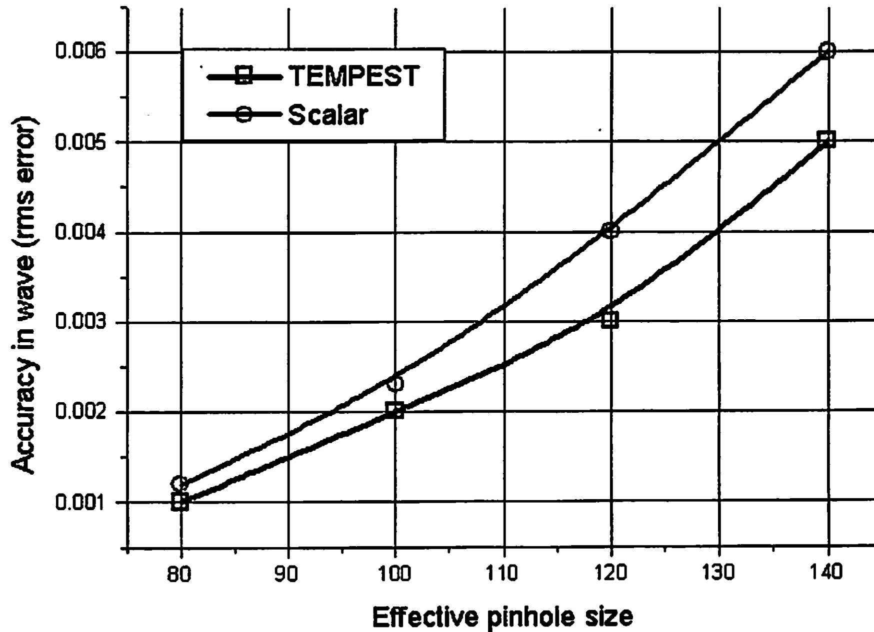

Fig. 2-18 The plot of the *reference-wavefront-error-limited accuracy* of the PS/PDI obtained from the scalar diffraction calculations and TEMPEST simulations.

Effective pinhole size (nm)	Reference-wavefront-error-limited accuracy from TEMPEST simulations (wave)	Reference-wavefront-error-limited accuracy from scalar diffraction calculation (wave)	Systematic-error-limited accuracy from TEMPEST simulations (wave)	Systematic-error-limited accuracy from scalar diffraction calculations (wave)	Systematic-error-limited accuracy from null experiments (wave)
80	0.0010 ±0.001	0.0012 ±0.0005	0.001 ±0.001	0.002 ±0.001	0.0028 ±0.0001
100	0.0020 ±0.001	0.0023±0.0005	0.002 ±0.001	0.003 ±0.001	0.0041 ±0.0003
120	0.0031 ±0.001	0.0041 ±0.001	0.005 ±0.002	0.006 ±0.001	0.010 ± 0.001
140	0.0053 ±0.002	0.0061 ±0.001	0.006 ±0.002	0.007 ±0.002	0.012 ± 0.001

Table 2-4 The results from the null experiments, TEMPEST simulations, and the scalar diffraction calculations for the PS/PDI accuracy. The *reference-wavefront-error-limited accuracy* and the *systematic-error-limited accuracy* obtained from the simulations are compared to the experimental results. The simulated results tend to have smaller rms error compare to the experimental results. Since there are subtler problems in the experiment, the experiemntal results indicate more rms error.

The results, from the null experiments, TEMPEST simulations, and scalar diffraction calculations, are compared in the Table 2-4. The *systematic-error-limited accuracy* of the PS/PDI from the TEMPEST simulation is determined to be 0.001 waves (λ/1000 or 0.01 nm), 0.002 waves (λ/500 or 0.02 nm), 0.003 waves (λ/300 or 0.045 nm), and 0.005 (λ/200 or 0.067 nm) for 80-nm, 100-nm, 120-nm, and 140-nm effective pinhole size pairs respectively over 0.08 NA. The accuracy of the PS/PDI from the null experiment is found to be 0.0028 waves (λ/357, 0.038 nm), 0.0041 waves (λ/244 or 0.055 nm), 0.010 waves (λ/100 or 0.13 nm), and 0.0012 waves (λ/83 or 0.16 nm), for 80-nm, 100-nm, 120-nm, and 140-nm effective pinhole size pairs respectively over 0.08 NA [75]. The corresponding plot of the *systematic-error-limited accuracy* is shown in Fig. 2-19.

The simulated results tend to have smaller rms errors compare to the experimental results. Even though some discrepency exist in the results, the simulations can be used to reinforce the experimental results. By adding some possible errors affecting the accuracy in the experiment, the simulation results can be brought even closer to the experimental results. Some of these higher order error sources include detector noise, two wavefront shearing, and pinhole shapes [76].

2.7 PS/PDI AS HOLOGRAPHY

When a coherent reference wave interferes with light *diffracted* by or *scattered* from an object, a hologram of the object wave is recorded. From this hologram both amplitude and phase information of the object wave can be obtained. For the PS/PDI, the reference wave is the pinhole-diffracted beam and the object wave is the test beam (Fig. 2-20). Thus, the

PS/PDI interferogram can be interpreted as a hologram of the point spread function (PSF) of the optical system.

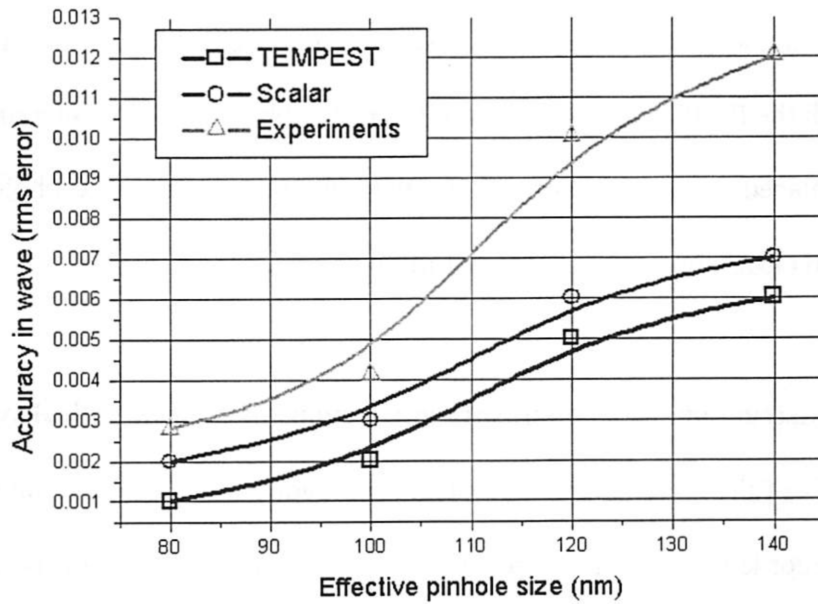

Fig. 2-19 The plot of *systematic-error-limited accuracy* of the PS/PDI obtained from the scalar diffraction calculations, TEMPEST simulations, and the null experiments.

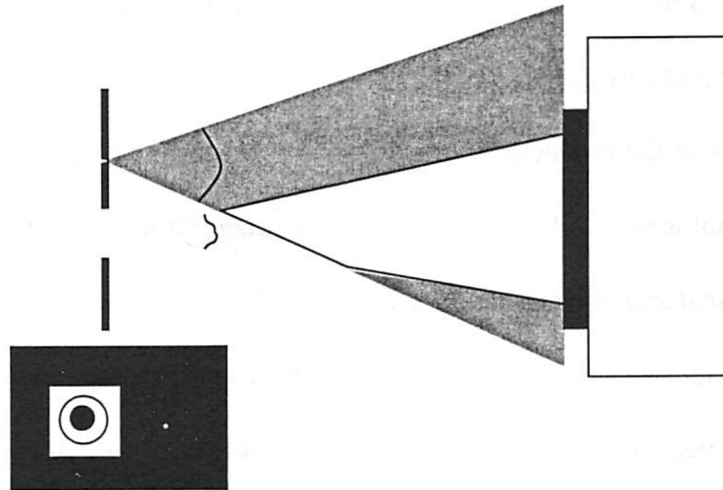

Fig. 2-20 Schematic diagram describing the interferogram as a Fourier transform hologram. The interferogram recorded in the PS/PDI system can be interpreted as a hologram of the point spread function (PSF) of the optical system. Since the recording device is located at the Fourier-transform plane of the image plane, the hologram is a Fourier transform type.

Considering the entrance pinhole as a point source, the image of that pinhole produced by the optical system is the PSF. Thus, the test wave at the recording plane is the far-field (Fraunhofer region) propagated PSF of the system. As seen in Fig. 2-20, the test wave interferes with the reference spherical wave at the CCD plane, thus, the interferogram obtained with the PS/PDI is a hologram of the PSF. Noting that the reference-wave origin is laterally displaced from the large window, the hologram is an off-axis hologram. The PSF and pupil wavefront form a Fourier-transform pair [77].

2.7.1. Reconstruction of the point spread functions of the 10× optical systems

The PSFs of the imaging optical systems are readily obtained from the interferograms or holograms recorded during interferometry. The Fraunhofer diffraction is related by Fourier transform [77]. Therefore, the test and the reference waves are simply the Fourier transforms of the system PSF and a point source respectively, and their interference pattern is a Fourier-transform hologram [77]. The detail descriptions of Fourier-transform holography are treated in Chapter 3 of this thesis.

Owing to the characteristics of Fourier-transform holography, Fourier transforming the recorded hologram yields the reconstructed image of the system PSF. This is similar to the Fourier-transform interferogram analysis method described in section 2-4. The Fourier-transform interferogram analysis methods reconstruct the system PSF and then propagate that to the exit pupil plane to retrieve the wavefront information at the exit pupil. Recalling Eq. 2-3, which is a mathematical representation of the hologram,

$$I(x,y) = I_1 + I_2 + I_3 \cdot e^{i\Phi(x,y)} \cdot e^{i(2\pi \bar{f}_c \cdot \bar{x} + \Delta)} + I_3^* \cdot e^{-i\Phi(x,y)} \cdot e^{-i(2\pi \bar{f}_c \cdot \bar{x} + \Delta)} \qquad \text{Eq. 2-3}$$

where $\Phi(x,y)$ indicates phase deviations from a spherical wavefront at the CCD plane (noting that the CCD plane is approximately at the system exit pupil plane). By taking the Fourier transform of Eq.2-3, the Fourier transform of $I_3 \cdot e^{i\Phi(x,y)}$ and its conjugate terms represent the system PSF. Using this method, the PSFs of five different 10×Schwarzschild optics have been reconstructed from interferograms obtained with the PS/PDI and are shown in Figs. 2-21(b) through (f) in log scale. For an aberration-free imaging system with a circular exit pupil, the system PSF should be in the form of an Airy pattern as shown in Fig. 2-21(a) [77]. These PSFs contain not only the wavefronts figure errors, which correspond to the low spatial frequency terms, but some flare information, which represents frequency terms up to 1.5-μm radius in the image plane. Degraded Airy patterns are observed for 10×-I and 10×-Berkeley optics, whose wavefront aberrations are relatively large, and better airy patterns are observed for Camera B1 and B2 indicating high quality wavefronts.

In summary, the system PSF can be reconstructed by taking a Fourier transform of the interferogram obtained from the PS/PDI, and the interferogram can be interpreted as a Fourier-transform hologram of the system PSF.

2.8 CONCLUSION

The phase-shifting point diffraction interferometer (PS/PDI) has been developed to test EUV prototype lithographic optics at the operational wavelength of 13.4 nm with extremely high measurement precision and accuracy. Five different EUV optics have been tested with the PS/PDI, and the wavefront errors as small as λ/20 rms have been measured. Besides the wavefront quality measurements, investigations of multilayer effects, comparisons with the

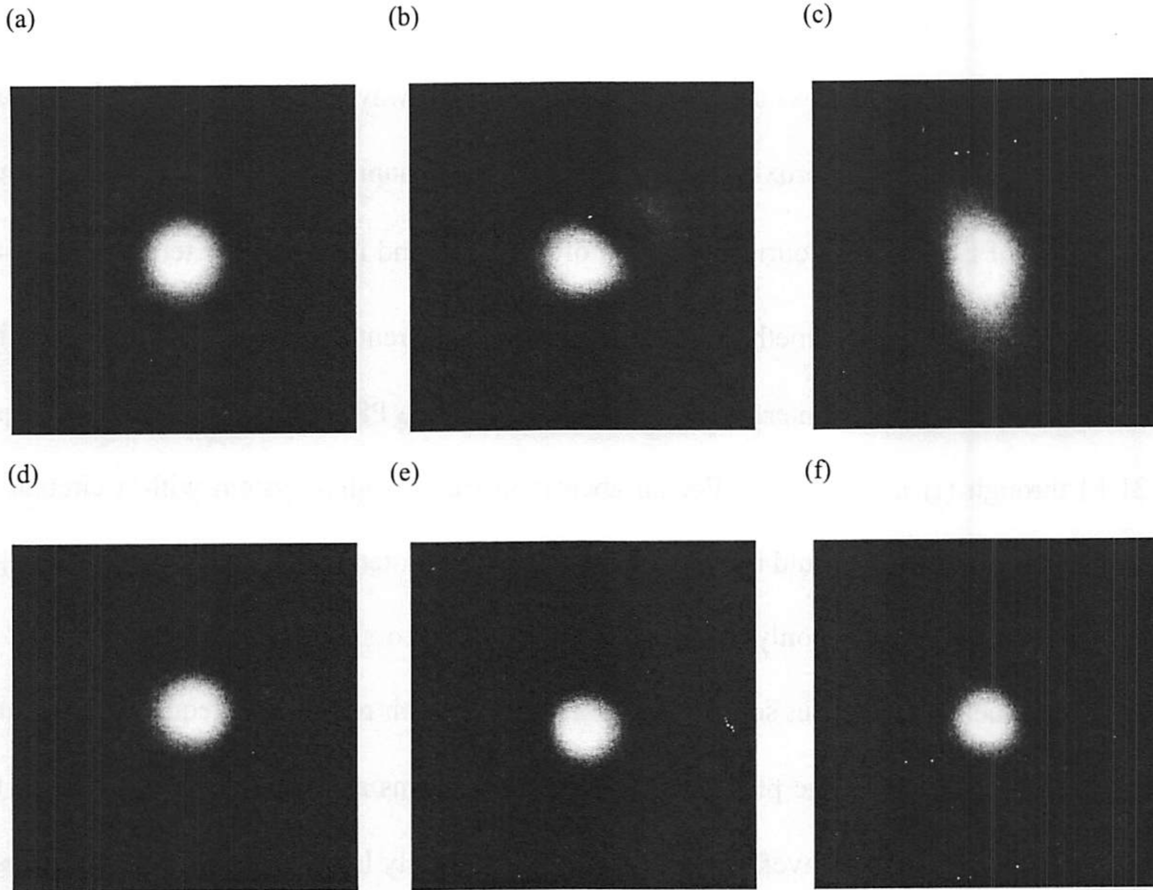

Fig. 2-21 (a) PSF of a perfect optical system. For a circular exit pupil, the PSF is essentially an Airy pattern. PSFs of (b) 10×-I, (c) 10×-Berkeley, (d) Camera A, (e) Camera B1, and (f) Camera B2 optics. Degraded Airy patterns are observed for 10×-I and 10×-Berkeley optics, whose wavefront aberrations are relatively large, and better airy patterns are observed for Camera B1 and B2 indicating high quality wavefronts.

visible light interferometer, and flare characterizations have been successfully performed with the PS/PDI. The accuracy of the interferometer has been verified by way of experiments and electromagnetic simulations. The *systematic-error-limited accuracy* of the PS/PDI has been found to be 0.0028λ (λ/357) and 0.002λ (λ/500) with the experiments and simulations respectively. The interferograms recorded with the PS/PDI can be interpreted as a hologram of the PSF of the optical system, and a simple Fourier transform is required to reconstruct the system PSF.

Chapter 3

EUV holographic aerial image recording

3.1 INTRODUCTION....53

3.2 EUV HOLOGRAPHY SYSTEM DESCRIPTION....54

3.3 FRESNEL AND FOURIER TRANSFORM HOLOGRAPHY....55

3.4 EXPERIMENTAL SET-UP....59
3.4.1 Alignment procedure....62

3.5 RECORDING HOLOGRAMS AND ANALYSIS....64
3.5.1 Determination of the window-pinhole separation....66
3.5.2 Resolution of the reconstructed holography....66

3.6 EXPERIMENTAL RESULTS....68
3.6.1 A circular aperture....68
3.6.2 Through focus studies....69
3.6.3 More complicated objects....71

3.7 SIMULATION OF THE COHERENT IMAGING PERFORMANCE OF CAMERA A....75

3.8 EFFECT OF FLARE IN THE HOLOGRAPHIC IMAGE RECORDING SYSTEM....79

3.9 ATTENUATED PHASE-SHIFTING OBJECT....84
3.9.1 Fabrication of the attenuated phase-shifting object....84
3.9.2 Holographic characterization of the attenuated phase-shifting object....87

3.10 CONCLUSION....89

3.1 INTRODUCTION

By using the PS/PDI described in the previous chapter, the wavefront quality of lithographic optical systems can be measured at the system operational wavelength. From the system wavefront, the imaging performance can be predicted analytically. However, it is often preferable to obtain direct measurements of imaging performance. Here I describe an at-wavelength holographic image recording technique developed to monitor the coherent imaging performance of high-quality EUV lithographic optical systems. This system is used to characterize the imaging performance of a 10× Schwarzschild objective with a variety of amplitude and phase objects.

As described in the previous chapter, the PS/PDI can be viewed as recording a Fourier-transform hologram of the optic PSF. Extending this idea, the holograms of more complicated objects can be recorded. In holography, when a suitably coherent reference wavefront interferes with an arbitrary wavefront emanating from some object distribution, electric field information, including amplitude and phase, can be recorded. This holographic information can be used to reconstruct the original object distribution. Holography may also be applied to recording a virtual object distribution such as an aerial image produced by an optical system, thus characterizing the optic's coherent imaging performance. An advantage of using holography to monitor the coherent imaging performance is that electric-field information including phase and amplitude, rather than simply intensity, can be obtained [80,81]. The holographic aerial image recording technique is also attractive due to its compactness and its ability to monitor the image without printing in photoresist. Although this holographic method imposes a coherent imaging condition on the system under test,

while lithographic printing typically employs partially coherent light, the partially coherent imaging performance can be predicted from the coherent image [57, 82].

3.2 EUV HOLOGRAPHY SYSTEM DESCRIPTION

In this study, lensless Fourier-transform holography is employed to record the aerial images produced by a 10×-Schwarzschild optical system. This system is readily implemented by modifying the EUV phase-shifting point diffraction interferometer (PS/PDI).

(a)

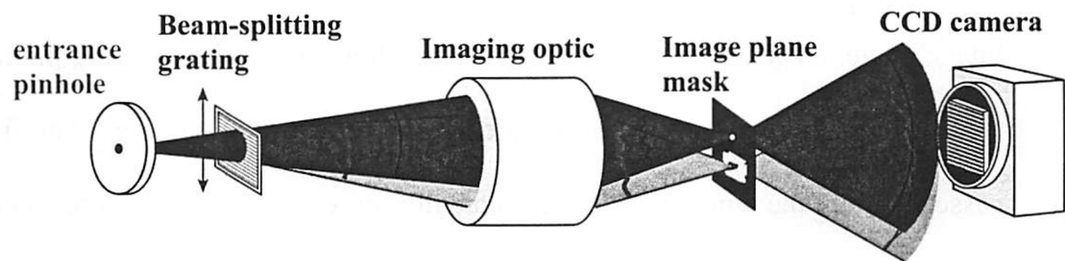

(b)

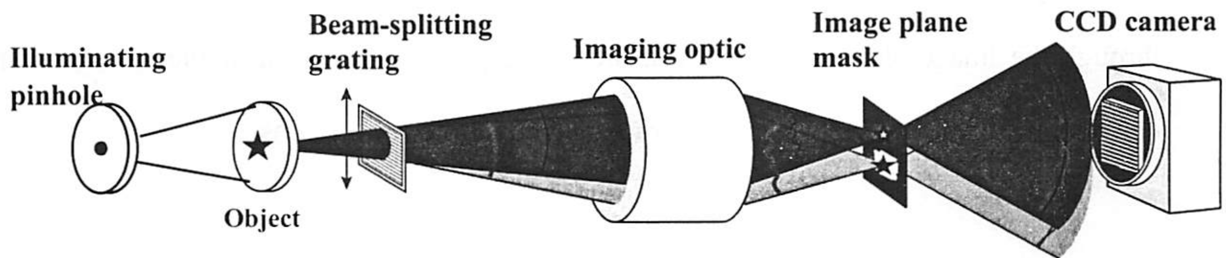

Fig. 3-1 (a) The PS/PDI system. The entrance pinhole is used as a point source object, and the system records the Fourier transform hologram of the PSF of the optical system under test. (b) Fourier-transform holography technique for recording lithographic aerial images. The object is illuminated with a coherent spherical wave generated from the sub-resolution illuminating pinhole.

Comparisons between the PS/PDI system to record the wavefront of the imaging system and the EUV holography system to record aerial images are described in Figs. 3-1(a) and (b). The entrance pinhole used as a point source object in the PS/PDI system is no longer used as an object for the holography system. Instead, the pinhole is pushed back and used to illuminate a more complicated object with a coherent spherical wavefront. The pinhole size is chosen to produce relatively uniform intensity illumination to the object plane mask. The rest of the holography system is identical to the PS/PDI configuration shown in Fig. 3-1.

The transmission grating inserted between the object and the optical system under test acts as a beam splitter, producing multiple, laterally displaced, images of the object in the image plane. A mask containing a square window and spatial-filtering pinhole is placed in the image plane to select two of the orders diffracted by the grating. The first-order image passes through the window and will eventually serve as the object beam, whereas the zeroth-order image is made to fall on the pinhole filter providing the spherical reference wave. The two beams propagate to the CCD camera where they overlap producing a hologram. The hologram captures a record of the aerial image produced by the optic under test as seen through the image-plane window, thus, the image plane distribution of the various shaped objects can be characterized by reconstructing the recorded holograms.

3.3 FRESNEL AND FOURIER TRANSFORM HOLOGRAPHY

Fresnel and Fourier transform holography can be described analytically using Fresnel and Fraunhofer diffraction theory. Fresnel holography corresponds to the case where the recording plane lies within the Fresnel diffraction region of the object distribution. When the recording plane resides in the Fraunhofer region of the object (these two planes will be

defined shortly.), the Fourier-transform holography condition is met. For Fourier-transform holography, the light from each point on the object interferes with the reference beam to create a sinusoidal fringe pattern with a complex valued spatial frequency that is unique to that object point.

Figure 3-2 shows the schematic diagram describing Fresnel and Fourier-transform holography. *plane a* and *plane b* in Fig. 3-2 correspond to the object and recording planes, respectively. According to the Huygens-Fresnel principle [77], the electric field, propagated from *plane a* to *plane b*, $U_b(x,y)$ can be written as

$$U_b(x,y) = c \cdot \int_{-\infty}^{\infty} u_a(\xi,\eta) \cdot \exp\left\{\frac{k}{2z}[(x-\xi)^2 + (y-\eta)^2]\right\} d\xi \cdot d\eta \qquad \text{Eq.3-1}$$

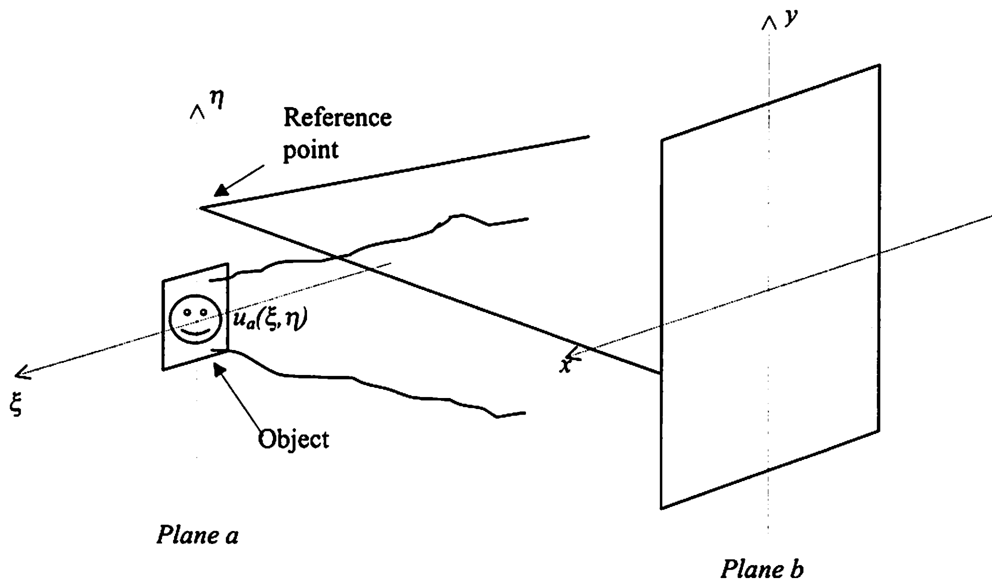

Fig. 3-2 Schematic of Fresnel/Fourier transform holography. Fourier-transform holography is a simplified form of Fresnel holography depending on the position of the recording plane. (Common z-axis is used.)

Applying the paraxial approximation*, Eq. 3-1 becomes

$$U_b(x,y) = c \cdot e^{j\frac{k}{2z}(x^2+y^2)} \cdot \int_{-\infty}^{\infty} \left\{ u_a(\xi,\eta) \cdot e^{j\frac{k}{2z}(\xi^2+\eta^2)} \right\} \cdot e^{-j\frac{k}{2z}(x\xi+y\eta)} d\xi \cdot d\eta \qquad \text{Eq. 3-2}$$

where $u_a(\xi,\eta)$ is electric field of an object in *plane a*, z is the distance between *plane a* and *plane b*, and k is a wave number, $2\pi/\lambda$. Equation 3-2 can be simplified by noting that Eq. 3-2 is essentially a Fourier transform of the object field distribution multiply by the Fresnel diffraction term, $e^{j\frac{k}{2z}(\xi^2+\eta^2)}$. Thus, Eq. 3-2 becomes

$$U_b(x,y) \ \alpha \ e^{j\frac{k}{2z}(x^2+y^2)} \cdot F.T. \left\{ u_a(\xi,\eta) \cdot e^{j\frac{k}{2z}(\xi^2+\eta^2)} \right\} \qquad \text{Eq.3-3}$$

If the Fresnel phase term, $\exp(\frac{k}{2z}(\xi^2+\eta^2))$, is large enough such that it significantly affects the calculation, $U_b(x,y)$ is in the Fresnel diffraction regime of $u_a(\xi,\eta)$. If the maximum value of the Fresnel phase term is sufficiently smaller than 1 rad, this term can be approximated to be zero and dropped out of the integral. In this case, $U_b(x,y)$ lies in the Fraunhofer diffraction regime of $u_a(\xi,\eta)$.

In Fresnel holography, the object and reference waves can be described using Eqs. 3-2 and 3-3. For simplicity the reference wave is assumed to originate from a point source, also in *plane a*, laterally displaced from the optical axis. The reference can thus be written as a

* The paraxial region of an optical system is a thin threadlike region about the optical axis which is so small that all angles made by the rays may be set equal to their sines and tangents. The paraxial approximation can be used in the paraxial region to simplify the calculations.

displaced delta function, $\delta(\xi - s, \eta)$ in *plane a*. The reference wave at the recording plane, *plane b*, can, thus, be written as

$$U_b(x,y)_{ref} = c \cdot e^{j\frac{k}{2z}(x^2+y^2)} \cdot e^{j\frac{k}{2z}(s^2)} \cdot e^{j\frac{k}{2z}(xs)} \qquad \text{Eq. 3-4}$$

The reference and the object waves described Eq. 3-2 and 3-4 interfere at the recording plane and generate a Fresnel hologram.

When *plane b* lies in the Fraunhofer regime, the object and the reference waves in *plane b* can further simplified as

$$U_b(x,y)_{obj} \;\alpha\; e^{j\frac{k}{2z}(x^2+y^2)} \cdot F.T.\{u_a(\xi,\eta)\} \qquad \text{Eq. 3-5}$$

$$U_b(x,y)_{ref} \;\alpha\; e^{j\frac{k}{2z}(x^2+y^2)} \cdot e^{j\frac{k}{2z}(xs)} \qquad \text{Eq. 3-6}$$

The object and reference waves at the recording plane are 2-D Fourier transforms of the object field and the point source respectively, hence Fourier-transform holography. Because this Fourier transform is achieved without the use of a lens, this type of holography is further known as lensless Fourier-transform holography. The $e^{j\frac{k}{2z}(x^2+y^2)}$ term in both equations indicates the spherical wavefront nature of the object and reference waves.

Combining the object and reference waves described above, general forms of the Fresnel hologram, $H_{Fresnel}$, and Fourier transform hologram, $H_{Fourier}$, recorded at *plane b* can be written as follows for the case described in Fig. 3-2.

$$H_{Fresnl}(x,y) = \left| (e^{j\frac{k}{2z}(s^2)} \cdot e^{j\frac{k}{2z}(xs)}) + F.T.\left\{ u_a(\xi,\eta) \cdot e^{j\frac{k}{2z}(\xi^2+\eta^2)} \right\} \right|^2 \qquad \text{Eq. 3-7}$$

$$H_{Fourier}(x,y) = \left| (e^{j\frac{k}{2z}(xs)}) + F.T.\{u_a(\xi,\eta)\} \right|^2 \qquad \text{Eq. 3-8}$$

In order to retrieve the object distribution, $u_a(\xi,\eta)$, from the holograms described in Eq. 3-7 and 8, a reverse diffraction model is necessary. The recording and reconstruction processes for Fourier-transform and Fresnel holograms are further discussed in sections 3.5 and 5.2, respectively.

3.4 EXPERIMENTAL SET-UP

The experimental setup for EUV holographic aerial image recording is depicted in Fig. 3-3. EUV radiation is provided by the undulator beamline described in section 2.6. Near the focal plane of the K-B, an illumination pinhole is used as a spatial filter to provide uniform and coherent illumination of the object. The spot size generated by the K-B system in the pinhole plane is approximately 20-μm in diameter with the ~15 μm × 10 μm elliptical coherence region. The pinhole size is chosen such that the diffracted beam from the pinhole generates a coherent spherical wavefront with uniformity of better than 10% in the object

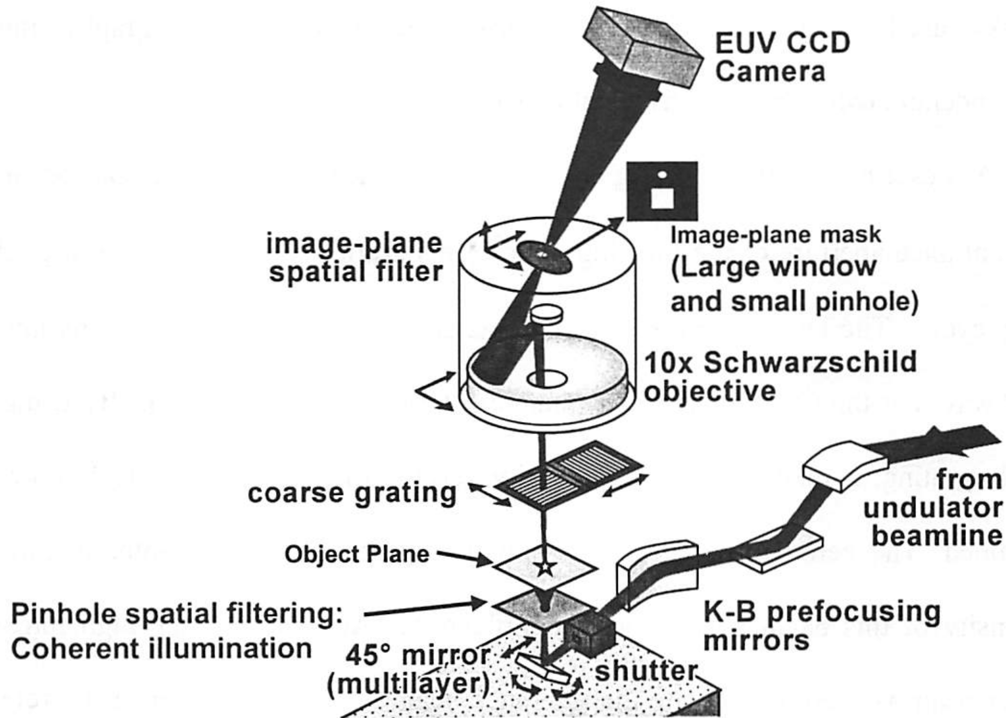

Fig. 3-3 Experimental configuration of the lensless Fourier-transform holography system. Coherent illumination at 13.4nm wavelength is provided by pinhole diffraction of the undulator beam. The illuminating pinhole is located below the object plane.

plane located 15 mm above the pinhole plane. The illumination pinhole is a commercially available 1.5-μm laser-drilled pinhole with 12-μm thickness. The pinhole is mounted in the modified HMF allowing 3-D positioning. The 15-mm separation and the 1.5-μm circular pinhole produce an illumination beam size of ~400-μm (null-to-null) in the object plane.

The object-plane mask can be readily replaced allowing various structures to be studied. The object mask is mounted in the same HMF such that the illuminating pinhole and the object mask are coupled together. The coupling between the illuminating pinhole and the object mask makes the alignment procedure extremely tedious and difficult (section 3.4.1).

The binary object masks used in this study were fabricated using electron-beam lithography at the *Center for X-ray Optics Nanowriter facility*. Ni is used as the absorber material patterned on top of a 100-nm thickness Si_3N_4 membrane. The phase-shift enhanced

masks used in this study were fabricated using optical lithography methods, and molybdenum (Mo) was used as the attenuating phase-shift material.

As described above, a grating beam-splitter is placed between the object-plane mask and the entrance aperture of the imaging optic. This grating is typically 18 μm pitch with 20% duty cycle. The low duty cycle (mostly opened) is used to help balance the intensity of the two waves at the CCD plane (after pinhole filtering of the reference). By using a low duty cycle grating, a relatively higher intensity zeroth-order beam than the first-order beam is obtained. The zeroth order beam is spatially filtered by a sub-resolution pinhole, so the intensity of this beam gets reduced significantly. Accordingly, the high intensity zeroth-order beam is used to generate the reference beam. Thus, the power of the reference beam can be matched to the first order beam, the object beam, by using a low duty cycle grating.

Owing to diffraction from the grating, multiple images of the object are formed at the image plane. At the image plane, the image-plane mask consisting of two windows is placed. The image-plane mask is fabricated using electron beam lithography and reactive ion etching. The mask pattern is completely etched through a 1000 Å Si_3N_4 membrane and then 1000 Å of Ni is evaporated on each side to provide the required EUV attenuation. The test beam window is a 3 μm × 3 μm square open area, and the reference pinhole, typically 50 nm to 150 nm in diameter, is placed 4.5 μm from the center of the window. The center-to-center separation is 1.5 times the window width in order to prevent any overlap between the holographic image and the zero order image. Since the image passes through the window, the lateral extent of the recorded image is restricted by the size of window.

A CCD detector is placed in the far-field region (128 mm away from the image plane). The Fresnel phase term can be safely neglected to record the Fourier-transform hologram,

because the CCD plane is located in the Fraunhofer region*** and the reference beam is a spherical wave originated from the image plane.

3.4.1 Alignment procedure

The alignment of the holography system described above is often a difficult and time-consuming task. The first step of the alignment procedure is to obtain proper illumination of the optic. In this step, the object mask is not in its place. Proper illumination of the optic can be achieved by steering the beam with the 45° mirror and repositioning the illumination pinhole. Figure 3-4(a) shows the intensity pattern when the optic is properly illuminated. The illumination pattern on the exit pupil of the optic can be monitored with the CCD camera. Once the proper illumination is established, the object must be aligned to the illumination.

Because the illuminating pinhole and the object mask are mounted in the same mechanical fixture, the object mask must be brought to the center of the illuminating beam without moving either the pinhole or the 45° mirror, in order to maintain proper illumination of the optic. Before aligning the actual mask, a pre-alignment object, a large circular aperture, is used. This pre-alignment technique is employed because it is more convenient to identify the diffraction pattern of a known object rather than some arbitrary object pattern. An Airy pattern is observed for the diffraction pattern of the pre-alignment circular aperture.

If the peak of the illumination beam with and without the circular aperture as seen in Fig. 3-4(b) coincide with each other, it can be concluded that the object mask is positioned correctly near the center of the original illuminating beam. Figure 3-4(c) depicts a situation

*** For an aperture of linear dimension D, the Fraunhofer approximation will be valid provided $z > 2sqr(D)/\lambda$ [77]. In our case, z is approximately 0.9mm. The CCD is located 128mm, thus this satisfies the requirement.

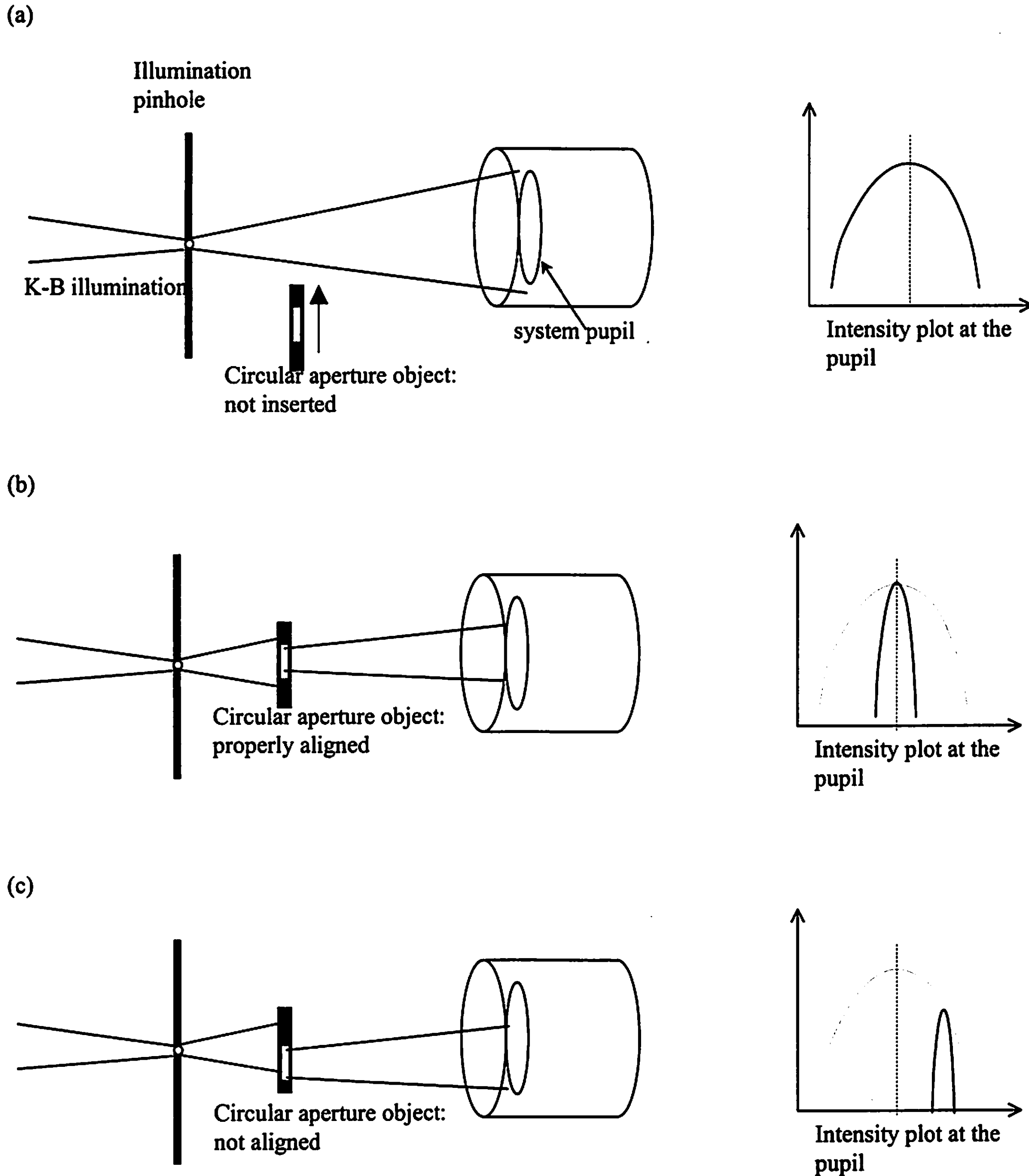

Fig. 3-4 Alignment procedures. (a) Diagram showing the proper alignment of pinhole and 45 degree turning mirror. The peak of the intensity plot coincides with the center of the pupil. The illumination pattern can be monitored with the CCD camera placed near the image plane of the exit pupil. (b) When the pre-alignment circular aperture is properly aligned to the center of the illuminating beam, the peak intensity positions with and without the aperture coincide. (C) When the alignment of the pre-alignment circular aperture is off from the center of the illuminating beam, their intensity peaks do not coincide.

where the pre-alignment mask is not properly aligned to the illuminating beam. After the circular-object position is properly set, the actual object can be aligned to the circular object offline using an optical microscope.

After alignment of the object, the image-plane mask must be aligned. The image-plane mask can be moved in three directions allowing the image field to be steered through the large window without obstruction. Next, the beam-splitting grating is introduced. Because the grating pitch is matched to the window-pinhole separation and the object distribution is relatively large, no additional alignment is required for the reference beam. Due to the strong attenuation of the reference beam, exposure times required to record quality holograms lie in the 2 to 5 minutes range.

3.5 RECORDING HOLOGRAMS AND ANALYSIS

Recording and reconstruction of the Fourier-transform hologram for aerial image recording experiments is described as follows. The electric field distribution of the aerial image, centered in the test window, is written as $u(\xi,\eta)$. Propagating this distribution to the CCD plane located in the far field yields $U(x,y)$. Similarly, $T(x,y)$ is the far-field propagation of $t(\xi,\eta)$, which is simply a point source representing the reference pinhole. Noting that far-field (Fraunhofer) diffraction can be expressed as a Fourier transform, $U(x,y)$ and $T(x,y)$ are simply Fourier transforms of $u(\xi,\eta)$ and $t(\xi,\eta)$, such as

$$U(x,y) = F.T.\{u(\xi,\eta)\} \quad \text{Eq. 3-9}$$

$$T(x,y) = F.T.\{t(\xi,\eta)\} \quad \text{Eq. 3-10}$$

Therefore, the intensity pattern recorded at the CCD can be written as

$$I_{CCD}(x,y) = |U(x,y) + T(x,y)|^2 = U \cdot U^* + T \cdot T^* + U \cdot T^* + T \cdot U^* \quad \text{Eq. 3-11}$$

The reference field is generated by pinhole diffraction, thus *T(x,y)* is approximated to be the Fourier transform of a delta function, which is a plane wave. Because the reference pinhole is displaced by s from the center of the image field in the image plane, *T(x,y)* can be written as:

$$T(x,y) = F.T\{\delta(\xi - s, \eta)\} = T_0 \cdot \exp(j2\pi \frac{s}{\lambda z} x) \quad \text{Eq. 3-12}$$

The hologram represented by Eq. 3-11 contains information of the image field distribution. This image field can be recovered by way of a Fourier transform. Taking the Fourier transform of Eq. 3-11 and invoking the Fourier transform convolution property yields

$$F.T.\{I_{CCD}\} = u \otimes u^* + t \otimes t^* + u \otimes t^* + t \otimes u^* \quad \text{Eq. 3-13}$$

where $u = F.T.\{U(x,y)\}$ and $t = F.T.\{T(x,y)\}$ and $\otimes$ indicates convolution. Constants and coordinate scaling factors have been neglected. The first and the second terms in Eq. 3-13 are the autocorrelation functions of the image and reference fields ,respectively, and the third and fourth terms are the image field and its complex conjugate convolved with the reference

field at the image plane. The autocorrelation functions correspond to an unwanted zero-order image. Since the reference field at the image plane, $t(\xi,\eta)$, is a displaced delta function, the third and fourth terms yield the image field information, $u(\xi,\eta)$ and $u^*(\xi,\eta)$, displaced by $\pm s$ from the center of the zero-order image.

3.5.1 Determination of the window-pinhole separation

Adequate separation between the pinhole and window center is required in order to prevent the reconstructed image-field information, $u(\xi,\eta)$, from overlapping with the zero-order image. The maximum size of the image field distribution at the image plane is determined by the size of the test window as described above. In Eq. 3-13, the first term, which is an autocorrelation function of the image field, has a maximum width of twice of the test window size. Because the reference is a delta function, the third and fourth terms have a maximum width of the test window size. In order to prevent the overlap between the first term and the third term, the displacement must be larger than 1.5 times of the maximum image field size, which in this case is the size of the test window. The minimum separation between the pinhole and window is described graphically in Fig. 3-5.

3.5.2 Resolution of the reconstructed holography

The resolution of the holographic aerial image recording technique depends on the reference pinhole diffraction, thus the pinhole size ultimately determines the smallest features which can be holographically reconstructed. The spatial components of the object field interfere with the reference wave emanating from a point source-like pinhole at the CCD plane. Smaller features tend to scattered into higher angles according to the diffraction

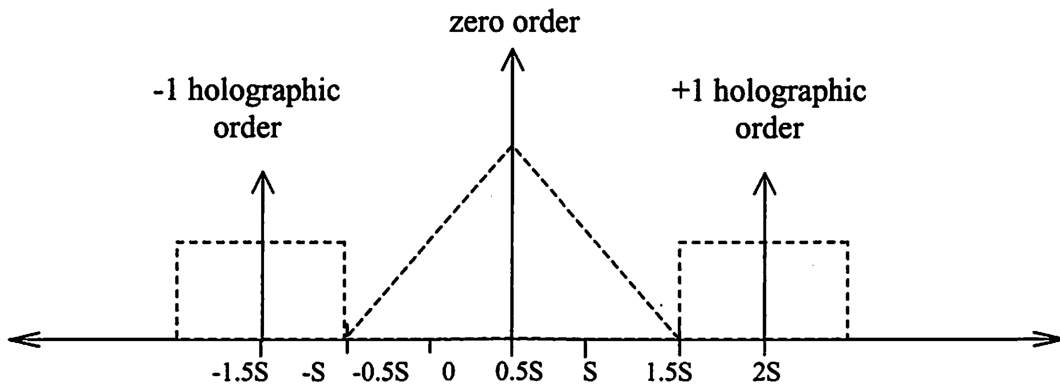

Fig. 3-5 One-dimensional view of the spatial-frequency spectrum of the recorded hologram, derived from the autocorrelation of the object-plane distribution (window-pinhole pair). Complete separation of the zero-order and the holographic orders requires the pinhole to window-center separation to be, at least, 1.5 times the window width.

principle. In order to capture the spatial components corresponding to smaller features of the object at the CCD plane, the diffracted angle from the pinhole has to be sufficiently large. Therefore, the smallest feature can be reconstructed from the Fourier transform holography depends on the pinhole diffraction angle. This can be readily seen by noting that the NA of the holographic recording is limited by the NA of the reference beam.

In the experiment described here, pinhole sizes of ~100 nm in diameter have been used. The diffraction angle determined by these pinholes corresponds to ~0.09 NA, yielding a holographic resolution limit of ~100 nm. It is interesting to note that the resolution is simply equal to the reference pinhole size.

The fact that the resolution is equal to the reference pinhole size also becomes evident by examining Eq. 3-13. The third or fourth term of Eq.3-13 is used to reconstruct the image field distribution. The original image field is convolved with the point source, and the resolution of the convolution integral depends on the convolution kernel, which in this case a

pinhole source. Thus, the size of the pinhole determines the resolution of the system. For example, if the pinhole is infinitely small (a delta function), a complete reconstruction of the image field distribution can be obtained.

3.6 EXPERIMENTAL RESULTS

The system described here has been used to characterize the coherent imaging performance of a recently fabricated 10×-reduction EUV Schwarzschild objective, Camera A (section 2.3.3). The wavefront quality of the Camera A is ~λ/13 rms over 0.088 NA at a wavelength of 13.4 nm. This particular optic suffers from about 30% flare in a 4-μm line due to the roughness of the mirror substrates. The Fourier transform holograms of images of various objects formed by the Camera A are recorded, and the images are holographically reconstructed using the Fourier-transform method. Because the optic is a 10×-demagnification system, the reconstructed images correspond to 10× reduced images of the objects and reveal the imaging performance of the optic.

3.6.1 A circular aperture

The first object considered was a simple 15-μm diameter circular aperture producing a 1.5-μm diameter image. The recorded hologram and its Fourier transform are shown in Figs. 3-6(a) and (b). As described above, the off-axis terms in the Fourier transform represents the image-plane distribution and its complex conjugate, respectively. Sufficient separation between the unwanted DC terms and the reconstructed 1.5-μm image is evident.

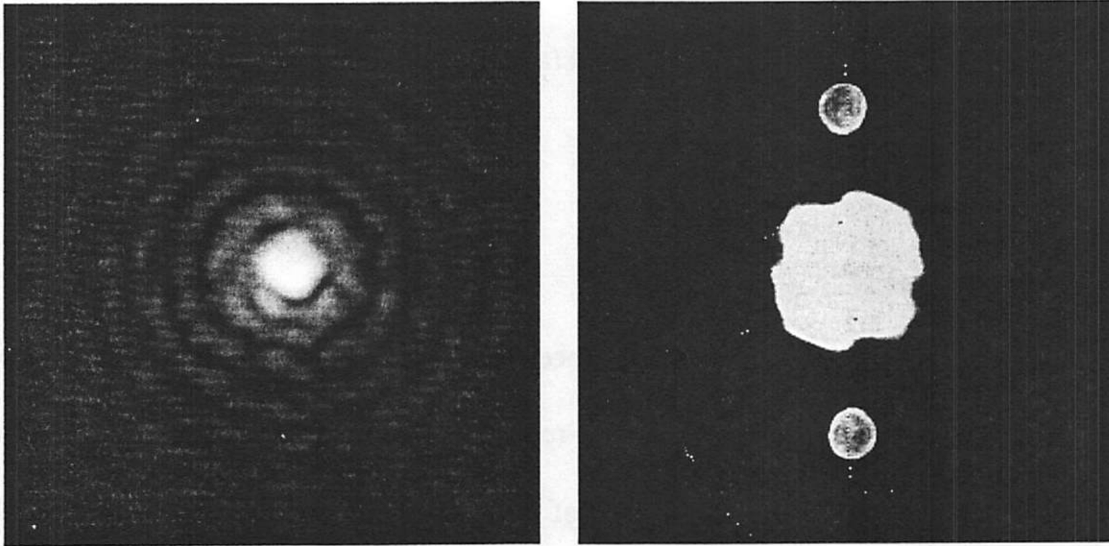

Fig. 3-6 Experimental results for a 1.5-μm image-side diameter circular aperture, (a) shows the recorded hologram and (b) its Fourier transform.

3.6.2 Through focus studies

By changing the longitudinal position of the image-plane mask, holograms of the images at various planes can be recorded. Because the image-plane mask can be moved in z-direction, the Fourier transform holograms of out of focused image can be recorded. This provides for a convenient method of performing through-focus studies. Figure 3-7(a) shows the through-focus images of the 1.5-μm circular aperture reconstructed from the different holograms. At +15 μm defocus, Fresnel ringing is evident. As the longitudinal recording plane moves closer to focus, the edges are observed to sharpen, and the dark spot at the center diminishes. At best focus, the rings observed around the sharp edge are characteristic of the coherent imaging process employed here. As we pass through the best focus and go to −15 μm defocus, images similar to the positive defocus image are observed indicating a low level of astigmatism in this optic. The depth of focus of the optic was found to be ~1.5 μm,

in good agreement with the theoretical value ($\lambda/NA^2 \approx 1.7$ μm). The cross-section plot of the PROLITH [85] aerial-image simulation results of 1.5-μm circular aperture is also shown in Fig. 3-7(b) for comparison purpose.

(a)

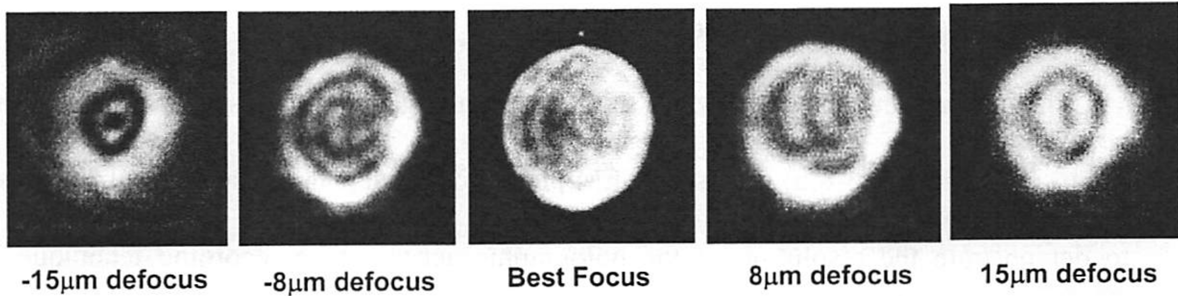

(b)

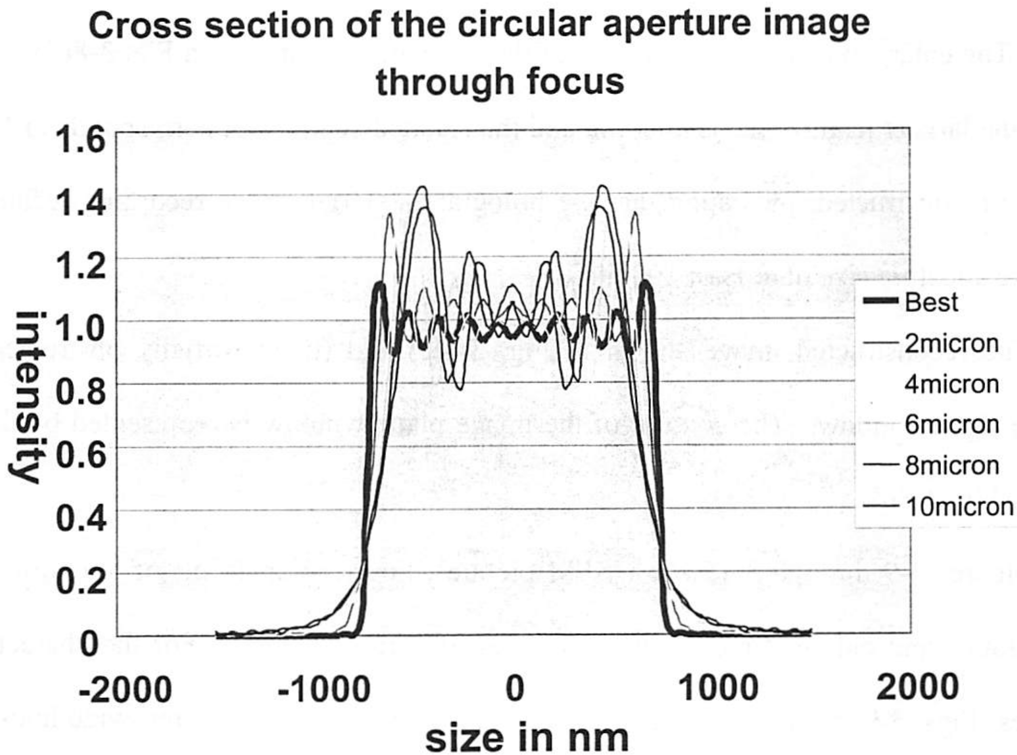

Fig. 3-7 (a) Through focus images of a circular aperture from experiments. At the best focus, the sharp edged circular aperture image is clearly evident along with Fresnel ringing. The almost symmetric image quality through focus indicates the astigmatism to be well controlled in the optic under test. (b) PROLITH aerial image simulations of a circular aperture. The coherent rings are observed through focus.

The coherent rings are observed through focus, which is in good agreement with the experimental results shown in Fig. 3-7(a).

3.6.3 More complicated objects

The next object considered was a star pattern having a continuous size variation from 0.3 μm to 3 μm. Figure 3-8(a) shows the SEM picture of the actual object. This object was used to demonstrate the resolution of the holographic aerial image recording technique. The square located at the center of the pattern is 1 μm × 1 μm. The Fourier transform hologram recorded with the CCD is shown in Fig. 3-8(b), and its Fourier transform is shown in Fig. 3-8(c). The enlarged reconstructed image of the star pattern is shown in Fig. 3-8(d). In Fig. 3-8(d), the largest feature size is 300 nm, and the isolated center spot corresponds to 100 nm is clearly reconstructed, indicating that the holographic aerial image recording technique can resolve a feature size of at least 100 nm.

The reconstructed image shown in Fig. 3-8(c) and (d) is partially obstructed by the image-plane window. The contour of the image plane window is represented by the dotted line in Fig. 3-8(d).

Figures 3-9 through 3-15 show SEM pictures, Fourier transforms of the corresponding holograms, and enlarged reconstructed images of various objects. For the character-based images [Figs. 3-9 through 12], the larger letters are comprised of 200-nm-wide lines, and the small letters of 100-nm-wide lines. Figures 3-13 through 15 show 200-nm equal lines and spaces, 150-nm equal lines and spaces, and 100-nm 1:3 lines and spaces elbow patterns, respectively.

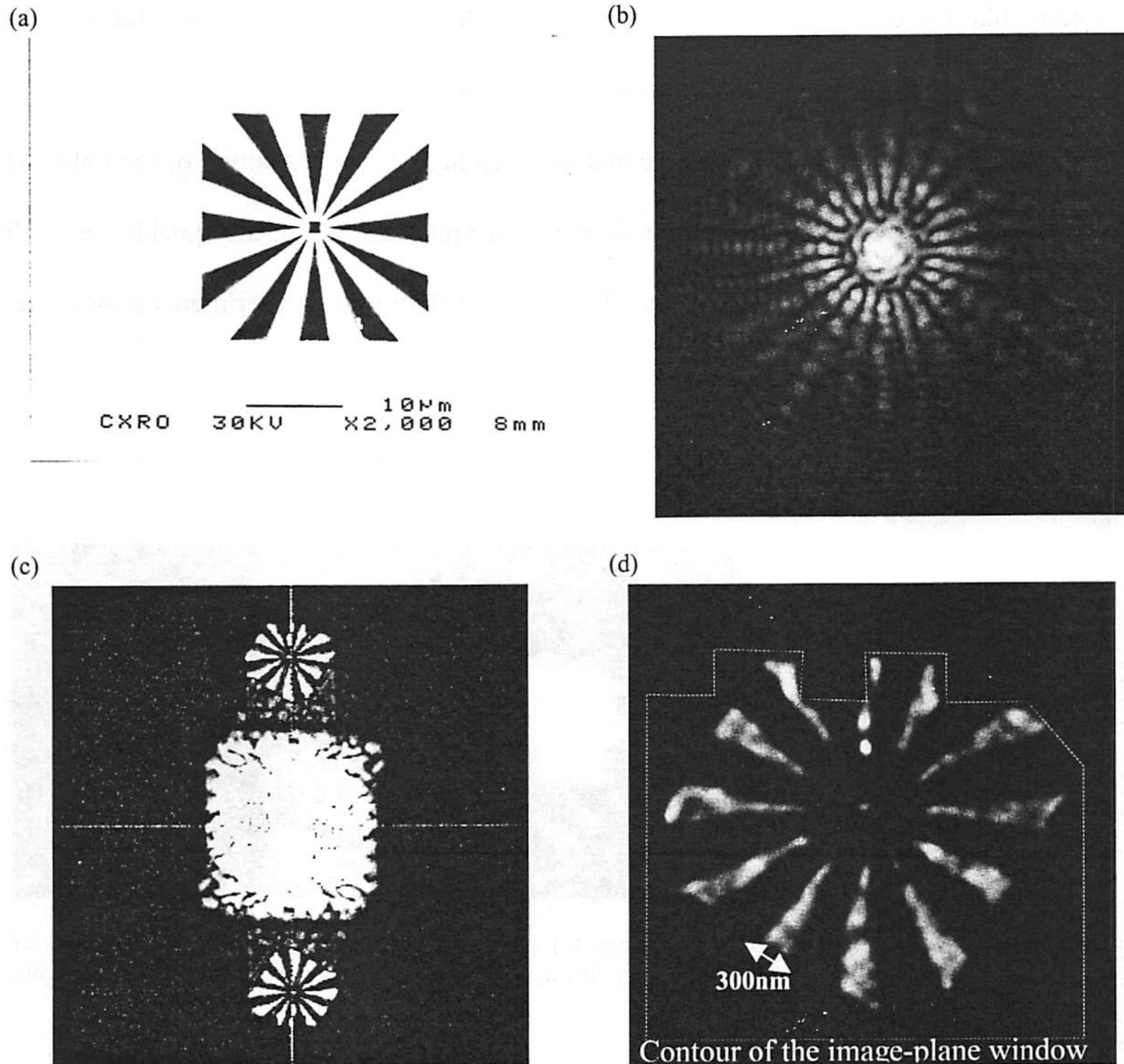

Fig. 3-8 (a) SEM picture of a star-pattern object. (b) The recorded Fourier-transform hologram. (c) Fast Fourier transform (FFT) of the hologram in (b). (d) Enlargement of one of the holographic orders. The spot located at the center of the pattern is 100 nm in diameter. The partial obstruction due to the image-plane window is indicated by the dotted line.

Speckle seen particularly clearly in Fig. 3-15 although present in all the reconstructed images arises primarily due to flare in the optic under test. As described above, the optic used here has previously been determined to suffer from approximately 30% flare in a 4-µm line [72,83]. Flare is caused by mid-spatial frequency roughness on the mirrors, and in conventional incoherent imaging systems leads to image contrast reduction. In coherent

systems like the one considered here, however, scatter leads to speckle with the size set by the diffraction-limited resolution of the optic under test.

Furthermore, with the holographic method used here, if the resolution of the holographic recording is lower than the diffraction-limited test optic resolution, the speckle size will be set by the resolution of the holography. The effect of flare in the experiments is simulated in detail in section 3-9.

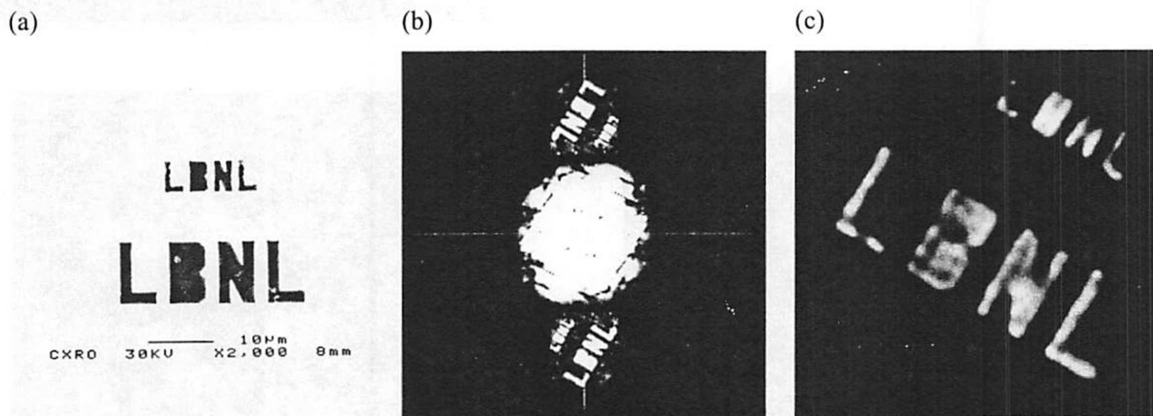

Fig. 3-9 Experimental results for a 'LBNL' logo (a) shows the actual object, (b) Fourier transform of recorded hologram, (c) the enlarged holographic image. The large letters correspond to 200nm in width, and small letters indicates 100nm in width.

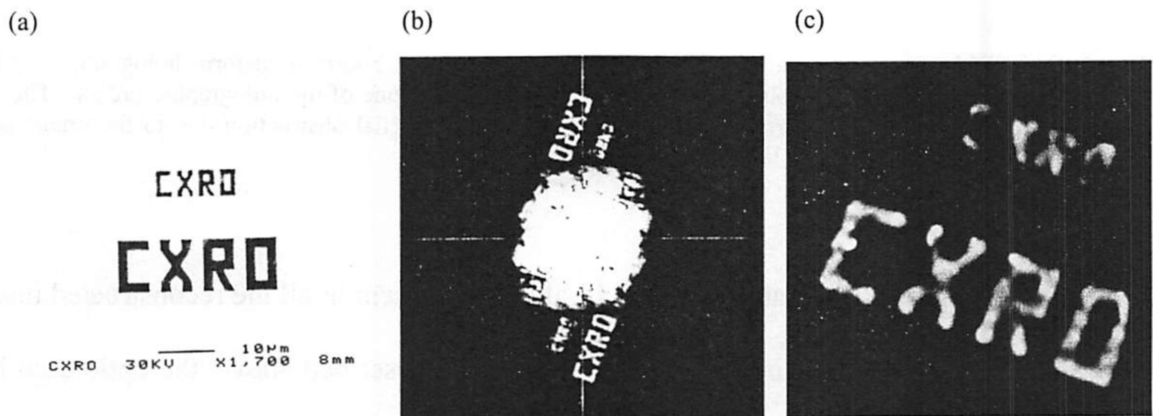

Fig. 3-10 Experimental results for a 'CXRO' logo (a) shows the actual object, (b) Fourier transform of recorded hologram, (c) the enlarged holographic image. The large letters correspond to 200nm in width, and small letters indicates 100nm in width.

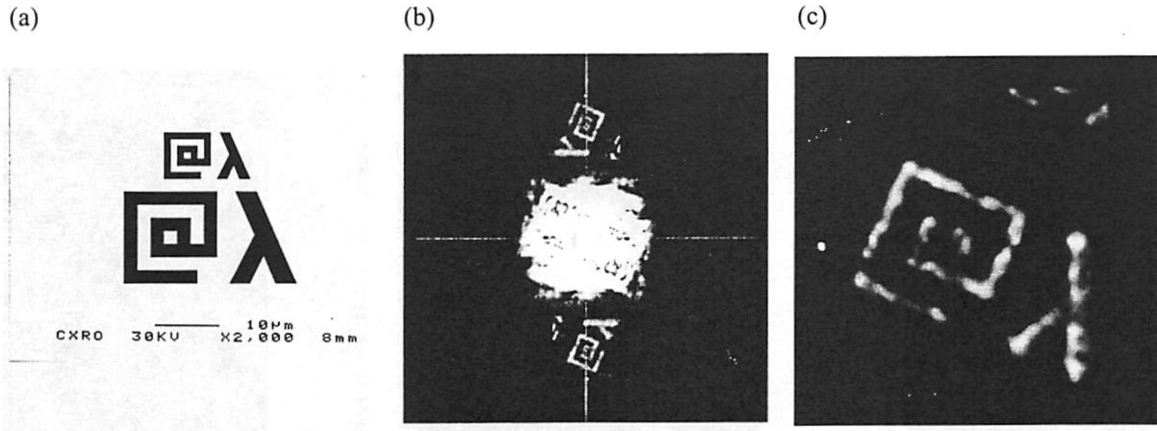

Fig. 3-11 Experimental results for a '@λ' logo (a) shows the actual object, (b) Fourier transform of recorded hologram, (c) the enlarged holographic image. The large letters correspond to 200nm in width, and small letters indicates 100nm in width.

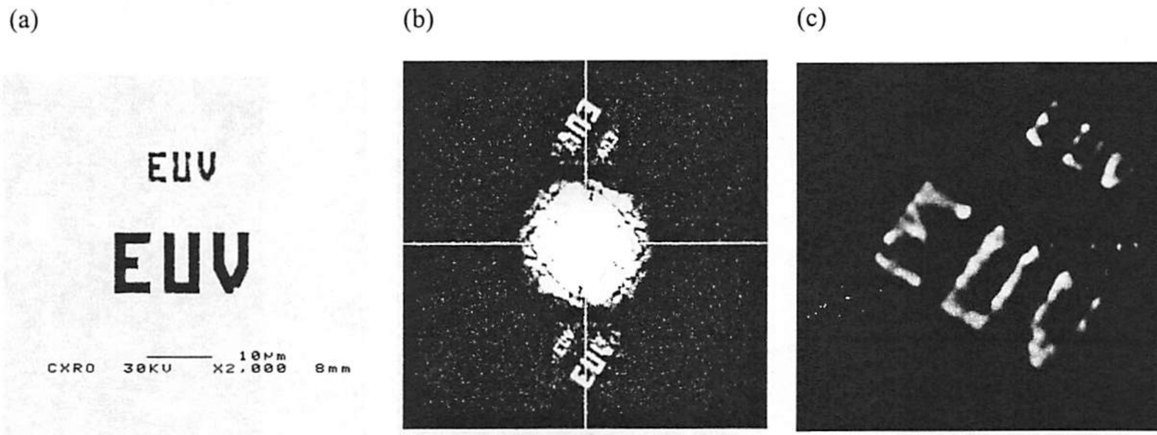

Fig. 3-12 Experimental results for a 'EUV' logo (a) shows the actual object, (b) Fourier transform of recorded hologram, (c) the enlarged holographic image. The large letters correspond to 200nm in width, and small letters indicates 100nm in width.

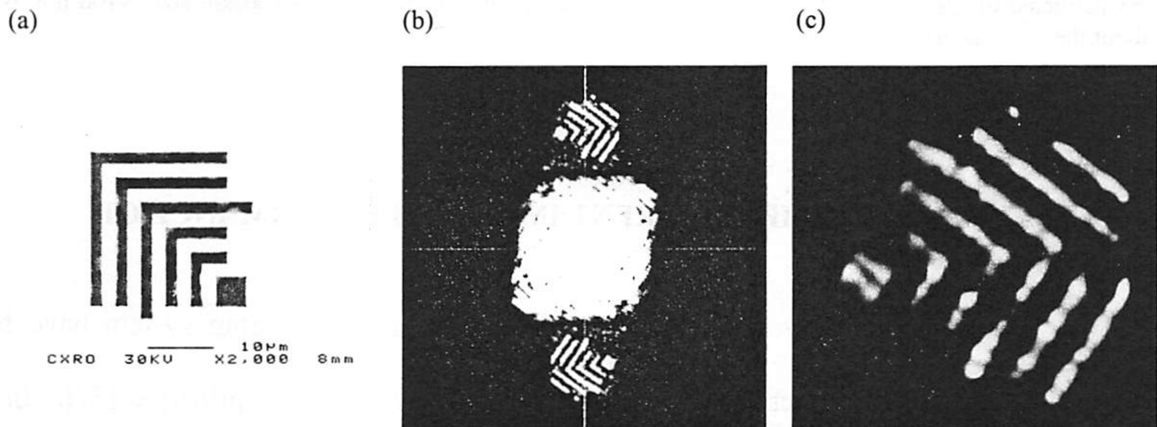

Fig. 3-13 Experimental results for a 200 nm equal lines and spaces elbow pattern (a) shows the actual object, (b) Fourier transform of recorded hologram, (c) the enlarged holographic image.

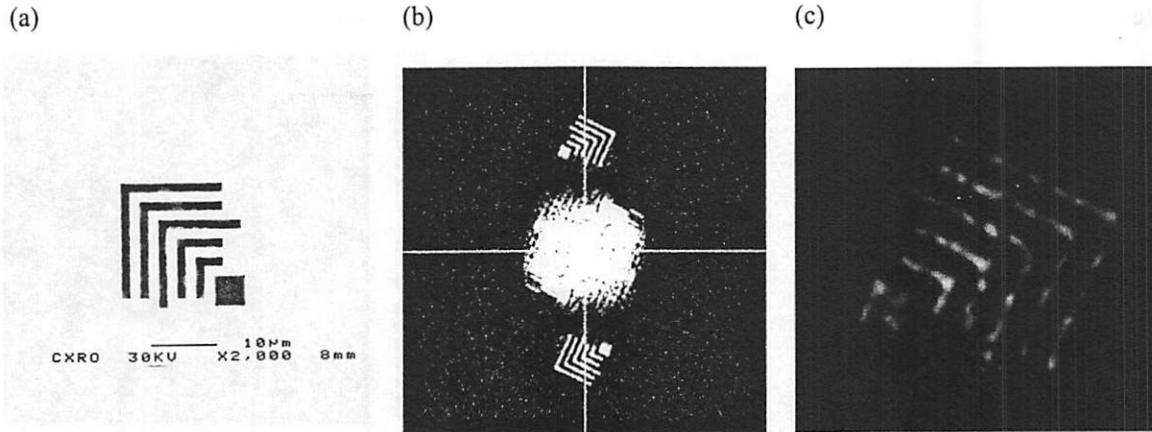

Fig. 3-14 Experimental results for a 150 nm equal lines and spaces elbow pattern (a) shows the actual object, (b) Fourier transform of recorded hologram, (c) the enlarged holographic image.

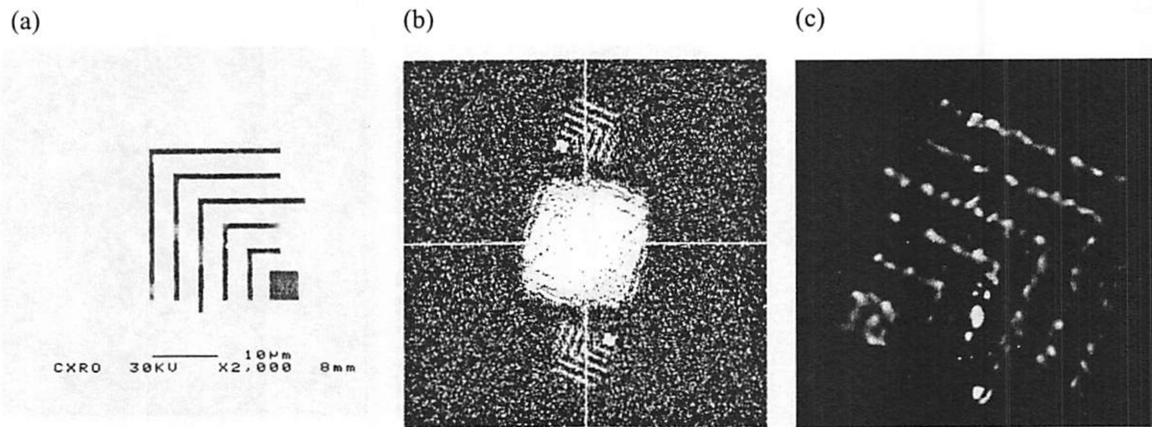

Fig. 3-15 (a) SEM picture of 150-nm 1:3 lines and spaces elbow pattern. (b) Fourier-transform of the recorded hologram. Due to low reference wave power, the signal to noise ratio is poor. (c) Enlarged reconstructed image. The flare of the optic causes speckle in the image. The speckle size, ~100 nm, is about the same as the resolution limit of the system.

3.7 SIMULATION OF THE COHERENT IMAGING PERFORMANCE OF CAMERA A

The results obtained with the holographic aerial image recording system have been verified by way of computer simulation using the Huygens-Fresnel principle [77]. In the simulation, I calculate the coherent aerial image based on the known pupil function of the

optic while ignoring the effect of flare. The wavefront quality at the pupil of Camera A has been well characterized with the previously described PS/PDI system.

Referring to the geometry in Fig. 3-16, suppose that an object is placed a distance z_1 in front of an imaging system and is illuminated by a monochromatic spherical wave. $U_o(\xi,\eta)$ represents the complex field immediately behind the object. The image plane of interest is taken to be a distance z_2 after the exit pupil of the imaging system, and the field in this plane is represented as $U_i(u,v)$. Being a coherent imaging system, the system is linear in electric field; hence, $U_i(u,v)$ can be expressed by the following superposition integral:

$$U_i(u,\upsilon) = \iint_{\infty} h(u,\upsilon;\xi,\eta) U_o(\xi,\eta) \cdot d\xi \cdot d\eta \qquad \text{Eq. 3-14}$$

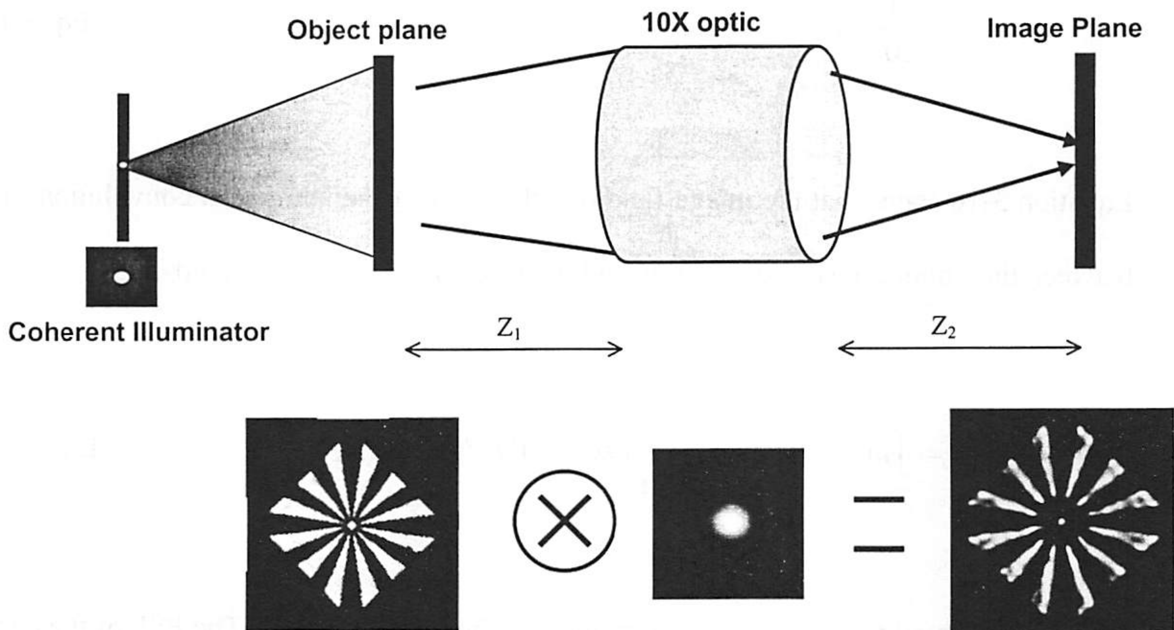

Fig. 3-16 Schematic depicting the simulation parameters. The simulation incorporates both the spherical object illumination and the aberration in the optic while ignoring the effect of flare. The object orientation is also taken into account for the simulations. The optic aberration had been precisely determined using the PS/PDI.

where $h(u,v;\xi,\eta)$ is the impulse response of the system. Thus the properties of the coherent imaging system are completely characterized by the impulse response h. The impulse response function described in Eq. 3-14 can be written as

$$h(u,v;\xi,\eta) = k \cdot \int_{-\infty}^{\infty} p(x,y) \cdot \exp\{-j\frac{2\pi}{\lambda z_2}[(u - M\xi)x + (v - M\eta)]\} dxdy \qquad \text{Eq. 3-15}$$

where $p(x,y)$ is the pupil function and M is the geometric system magnification defined as z_2/z_1. Using Eq. 3-15, Eq. 3-14 can be further simplified yielding

$$U_i(u,\upsilon) = \iint_{\infty} h(u - M\xi, \upsilon - M\eta) \cdot U_o(\xi,\eta) \cdot d\xi \cdot d\eta$$

$$= \frac{1}{M} h(u,v) \otimes U_o(\xi,\eta) \qquad \text{Eq. 3-16}$$

Equation 3-16 states that the image-field distribution is a 2-dimensional convolution integral between the impulse response function and the properly scaled object field, and

$$h(u,v) = \int_{-\infty}^{\infty} p(x,y) \cdot \exp[-j\frac{2\pi}{\lambda z_2}(ux + vy)] dxdy \qquad \text{Eq. 3-17}$$

is the point-spread function (PSF) determined by the pupil function. The PSF of the coherent imaging system can be readily calculated by taking a Fourier transform of the pupil function as seen in Eq. 3-17. In practice, the coherent image calculation is simplified by using the spatial-frequency representation of Eq. 3-16:

$$F.T.\{U_i(u,\upsilon)\} = \frac{1}{M} F.T.\{h(u,v)\} \cdot F.T.\{U_o(\xi,\eta)\} \qquad \text{Eq. 3-18}$$

Figure 3-17 shows the simulation results for the various objects used experimentally. In the simulation, actual SEM picture of the objects used in the experiments with the identical object orientation are used to generate the simulated object distributions. Also, the spherical and nonuniform nature of the experimental illumination is taken into account. The object distributions used in the simulation have been obtained by binarizing digitized SEM images of the experimental reticles. This qualitative agreement between experiments and simulations confirms that the holographic aerial image recording technique can be used to monitor the coherent imaging performance of lithographic

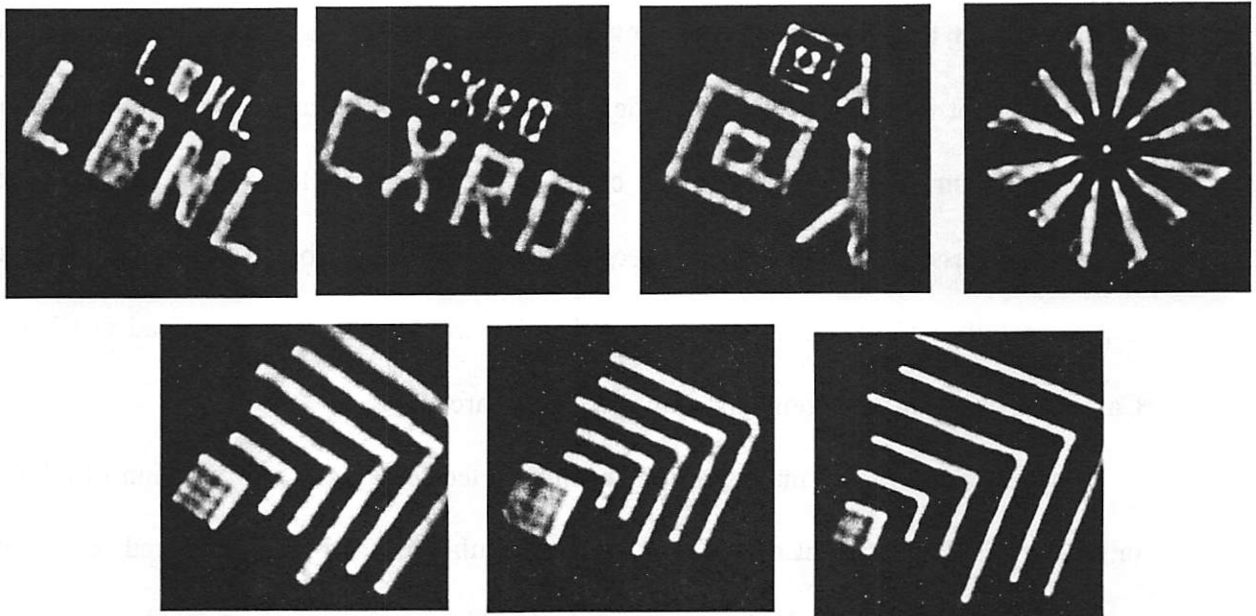

Fig. 3-17 Simulation results for various objects matching those used experimentally. Qualitative agreement with the experimental results is observed. The line edge roughness and the speckle patterns seen in the experiment do not appear in the simulation due to the fact the flare effects have been neglected.

optical systems. The discrepancies between the two results (line edge roughness and speckle-induced background noise observed in the experimental data but not the simulation) are most likely due to neglecting flare in the simulation.

3.8 EFFECT OF FLARE IN THE HOLOGRAPHIC IMAGE RECORDING SYSTEM

The demonstration of the holographic aerial image recording technique has been plagued by a significant level of speckle in the system caused by various sources, including random noise in the hologram, high-frequency phase structure (roughness) on the reticle, and flare in the optic. The speckle effect from random noise in the hologram decorrelates from exposure to exposure and can be mitigated by an averaging process. Experiments have shown the speckle to persist through averaging, thus the speckle is not expected to be dominated by random noise in the hologram. For the reticle to play an appreciable role in the speckle formation, the membrane roughness would have to induce relative phase shifts on the order of 2π. Given that the membrane is only 1000 Angstroms of Silicon Nitride, the image speckle cannot be attributed to the reticle. By process of elimination, flare in the optical system is assumed to be the dominant cause of the speckle. Here I simulate the coherent imaging process in the presence of speckle[**] using the same object distributions employed experimentally and the measured flare of the Camera A optic. As described in Chapter 2, Camera A optic suffers from approximately 30% flare.

For expediency, minimal effort has been directed towards the elimination of edge non-uniformity in the resultant distributions. The simulation has been performed on six of the object distributions shown in the previous section. Figures 3-18 through 23 show

[**] The flare in simulations has been generated by randomly varying speckle-sized amplitude and phase in the exit pupil.

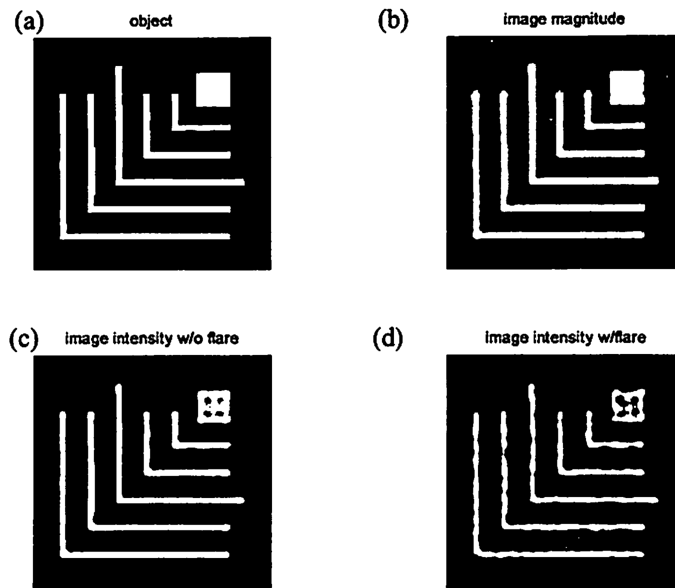

Fig. 3-18 100 nm lines 1:3 lines and spaces elbow pattern simulated with Camera A. (a) Object distribution obtained from an actual SEM picture. (b) Simulated image amplitude without flare. (c) Simulated intensity distribution without flare. (d) Simulated intensity distribution with flare.

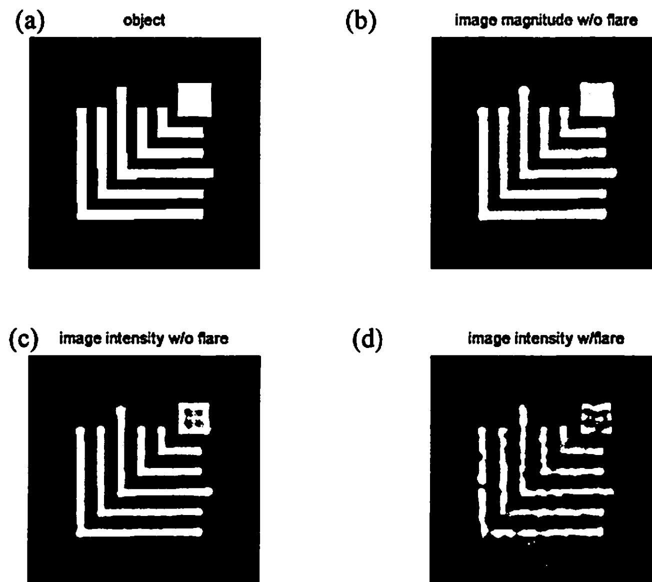

Fig. 3-19 150 nm lines 1:1 lines and spaces elbow pattern simulated with Camera A. (a) Object distribution obtained from an actual SEM picture. (b) Simulated image amplitude without flare. (c) Simulated intensity distribution without flare. (d) Simulated intensity distribution with flare.

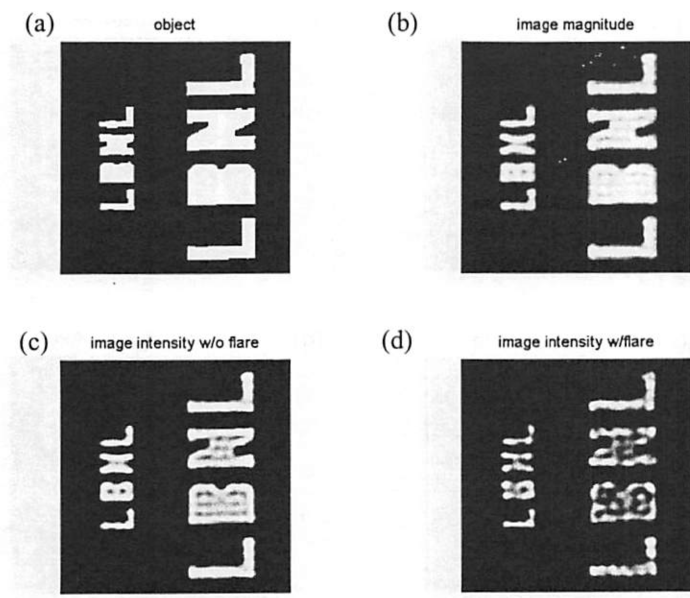

Fig. 3-20 'LBNL' logo simulated with Camera A. (a) Object distribution obtained from an actual SEM picture. (b) Simulated image amplitude without flare. (c) Simulated intensity distribution without flare. (d) Simulated intensity distribution with flare.

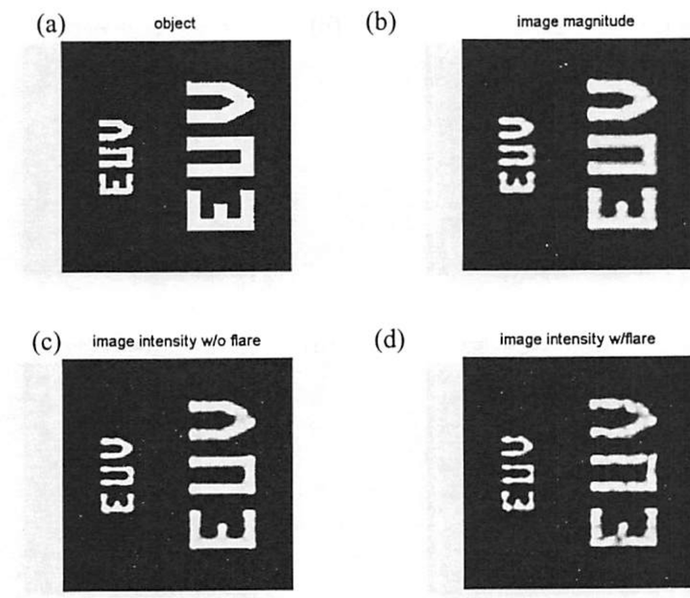

Fig. 3-21 'EUV' logo simulated with Camera A. (a) Object distribution obtained from an actual SEM picture. (b) Simulated image amplitude without flare. (c) Simulated intensity distribution without flare. (d) Simulated intensity distribution with flare.

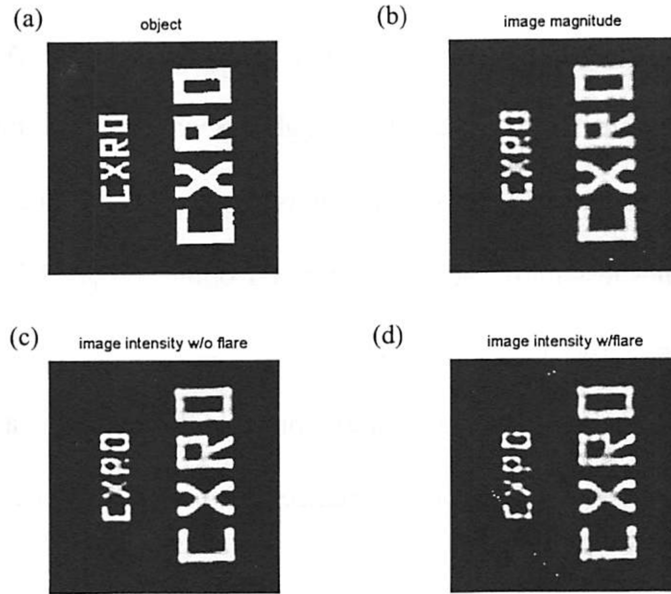

Fig. 3-22 'CXRO' logo simulated with Camera A. (a) Object distribution obtained from an actual SEM picture. (b) Simulated image amplitude without flare. (c) Simulated intensity distribution without flare. (d) Simulated intensity distribution with flare.

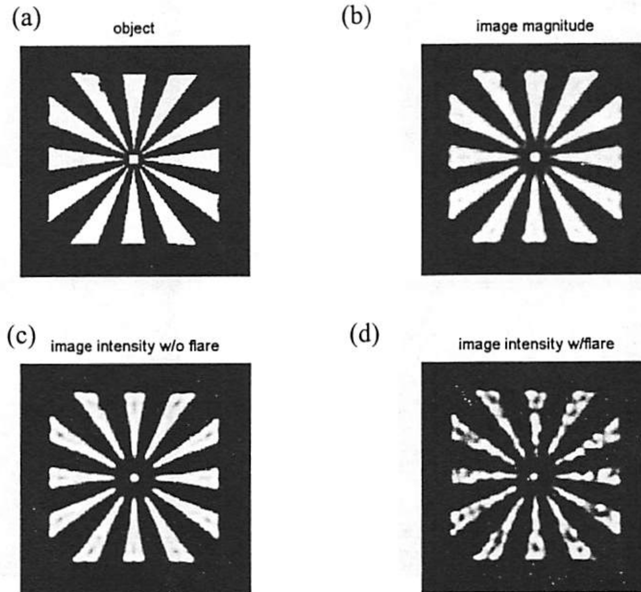

Fig. 3-23 Star resolution pattern simulated with Camera A. (a) Object distribution obtained from an actual SEM picture. (b) Simulated image amplitude without flare. (c) Simulated intensity distribution without flare. (d) Simulated intensity distribution with flare.

the object distribution obtained from SEM pictures, image intensity without flare, and image intensity with flare for the six objects used in the experiments. As seen in the figures, speckle caused by flare results line edge roughness and background noise in the image distribution. For comparison purposes we consider the results one would obtain with an optic having ten times less flare, such as Camera B1 optic. Figure 3-24 shows the simulation results for the star pattern with Camera B1. A significant improvement is evident indicating the flare actually causes the image degradation, and holographic aerial image recording technique can monitor the imaging performances of the optic with a significant amount of flare.

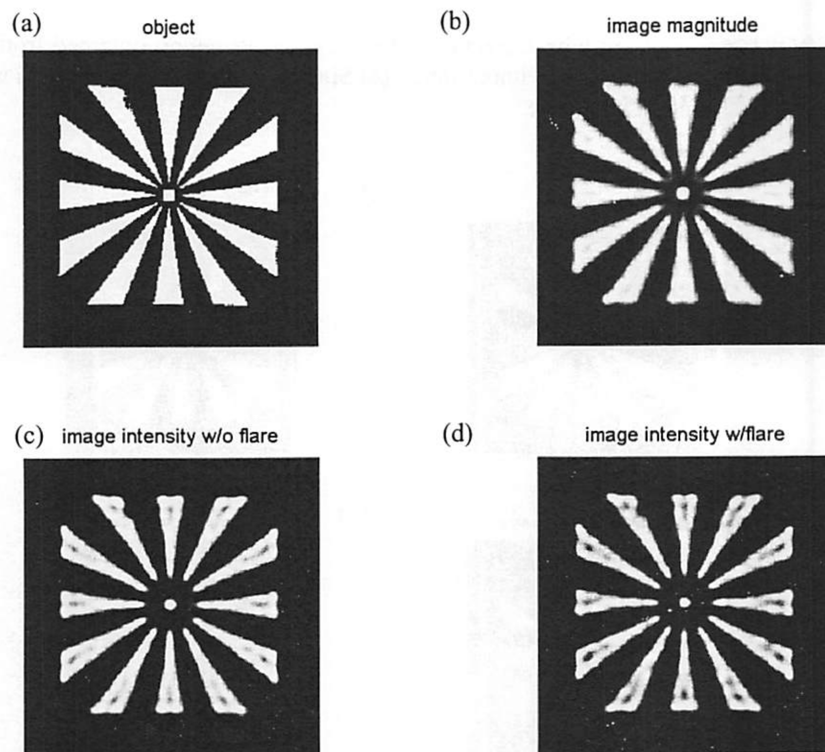

Fig. 3-24 Star resolution pattern simulated for Camera **B1**. (a) Object distribution obtained from an actual SEM picture. (b) Simulated image amplitude without flare. (c) Simulated intensity distribution without flare. (d) Simulated intensity distribution with flare.

3.9 ATTENUATED PHASE-SHIFTING OBJECT

An important property of the holographic aerial image monitoring technique is the ability to measure phase information as well as amplitude. This capability has been studied by way of phase-shift enhanced Molybdenum (Mo) masks. At a wavelength of 13.4 nm, Mo can provide a phase shift of π while maintaining approximately 60% intensity transmission. In this section, the fabrication and characterization of the phase-shifting mask at 13.4 nm wavelength is described.

3.9.1 Fabrication of the attenuated phase-shifting object

Transmission type attenuate phase-shift masks (APSM) have been fabricated using Mo patterns on Silicon Nitride (Si_3N_4) membranes [84]. 1000 Å of low stress, off-stoichiometric (Si rich) LPCVD Si_3N_4 was deposited on both sides of a (100) Si wafer. Silicon nitride on the backside of the wafer was patterned for nitride membrane fabrication. Mo was then deposited on the front side of the wafer by magnetron sputtering. To reduce the residual stress in the Mo film, the sputtering conditions were optimized i.e., plasma power and sputtering pressure were adjusted around 100 W and 90 mTorr. After deposition of the Mo, photolithography and reactive ion etch (RIE) using SF_6 and He gases were used to delineate the mask patterns.

After etching, PECVD oxide was deposited on the Mo patterns to protect them during the next Si wet-etch. The Si wafer was etched in KOH solution from the backside of the wafer, stopping on the Si_3N_4 on the front side. The final structure for the EUV APSM is an 860 Å thick (π phase-shift) patterned Mo layer on a 1000-Å-thick Si_3N_4 membrane.

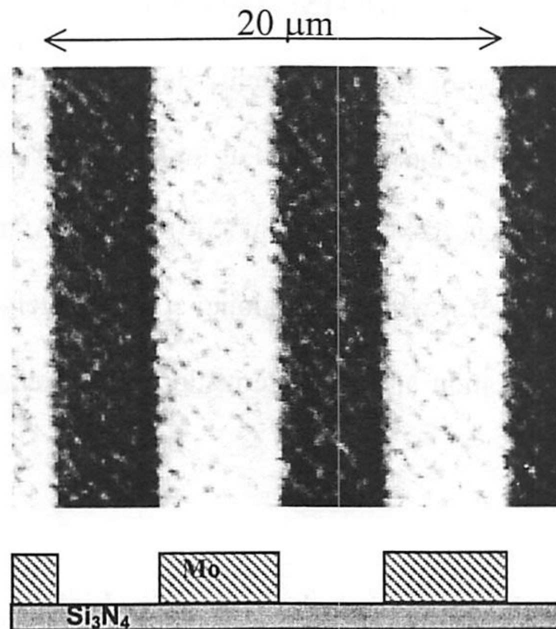

Fig. 3-25 Optical microscope image of the attenuated phase-shift mask. The bright regions indicate the Mo layers.

The visible microscope view of the 5-μm equal lines and spaces APSM is shown in Fig. 3-25, and its cross section is also depicted. The dark lines indicate Si_3N_4 regions and bright lines indicate Mo regions.

After etching of the Mo, the patterns were examined with top down SEM and AFM, to check the profile and thickness of the Mo. Figure 3-26 shows an AFM-scan of the vertical profile as well as an SEM images of the Mo patterns. The measured thickness of Mo, from the AFM scan, was about 800 Å, while the target thickness for π-phase-shift was 860 Å. As shown in Fig. 3-26(b), the Mo pattern edge had a discernable slope with measured width, from the top view SEM image, of about 20 nm. Taking the thickness of the Mo to be 80 nm, the calculated slope angle was about 14° from vertical.

The thickness of the phase-shifter, Mo, decides the phase-shift angle. To check the required tolerance for Mo thickness control, the effect of phase-shift error on the aerial image

of APSM was simulated with PROLITH [85]. Phase-shift angle was varied from 150° to 180°, which means Mo thickness varies from 717 Å to 860 Å. Figure 3-27 shows the result of the simulation. Although there is a significant variation in linewidth of the features, the high-contrast period doubling of the mask pattern is well preserved over this variation in phase-shift. For the purposes of frequency doubling then, the Mo deposition process has large margin of at least ±140 Å.

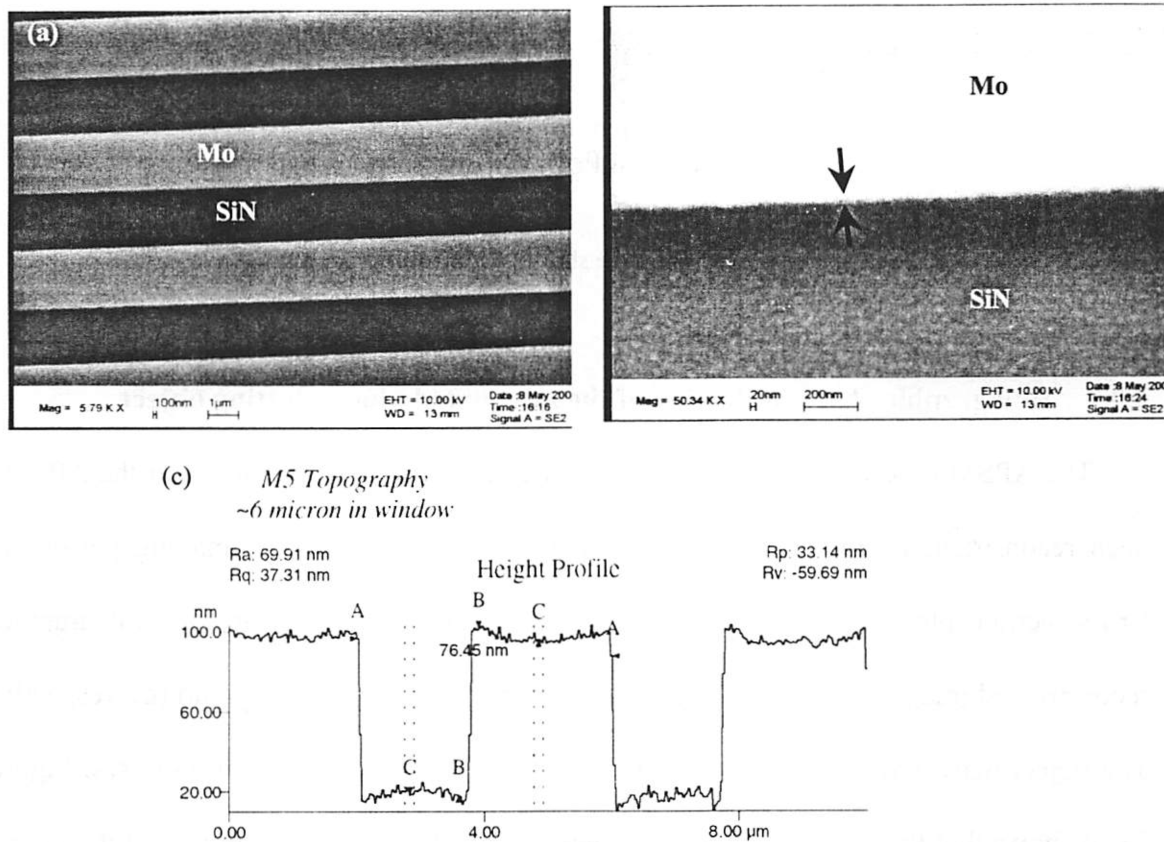

Fig. 3-26 SEM images of Mo patterns on Silicon Nitride: (a) large-field view and (b) magnified view of line edge. Slope width of Mo phase shifter edge is about 20 nm. (c) AFM scanned vertical thickness profile. Measured thickness of Mo was about 80 nm

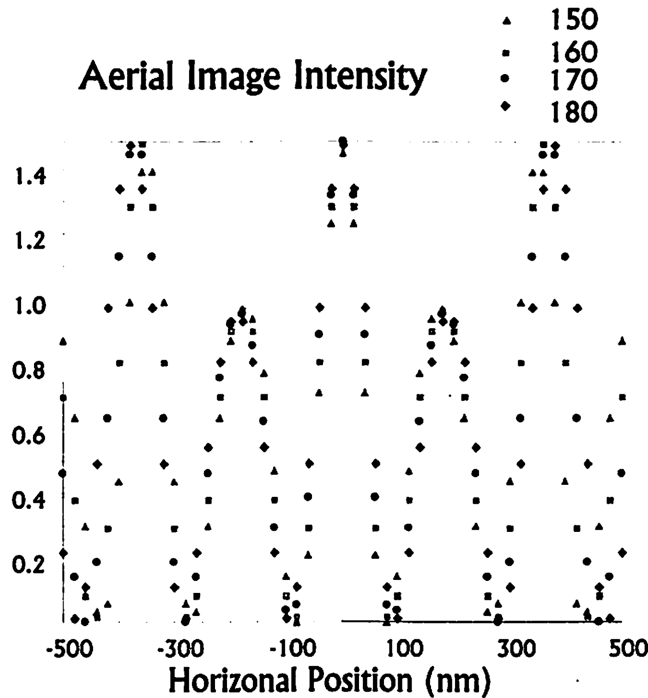

Fig. 3-27 Simulated aerial image intensity for phase shift angle, ranging from 150 to 180 degrees.

3.9.2 Holographic characterization of the attenuated phase-shifting object

The APSM described above has been used as an object, and the image of the APSM has been reconstructed with the holographic method to investigate the imaging performance. Cross-section plots of the electric field, phase, and intensity of the holographically reconstructed image of the phase object are shown in Figs. 3-28(b), (c) and (d), respectively. The object mask cross section is shown in Fig. 3-28(a) for comparison purposes. Figure 3-28(b) shows that the electric field crosses zero at the edges of Mo patterns, and that negative electric field is observed in the Mo regions. When the electric field is negative, the corresponding phase is close to π indicating that proper Mo thickness has been achieved. Measured phase difference between the normal (Si_3N_4 region) and phase-shifting (Si_3N_4 and Mo region) regions ranged from 150-180° as shown in Fig. 3-28(c). Small discrepancies

from π phase shift may be due to phase ringing caused by the limited resolution and imperfections of the Mo layer thickness. This also reveals that by measuring the phase, the Mo thickness can be characterized.

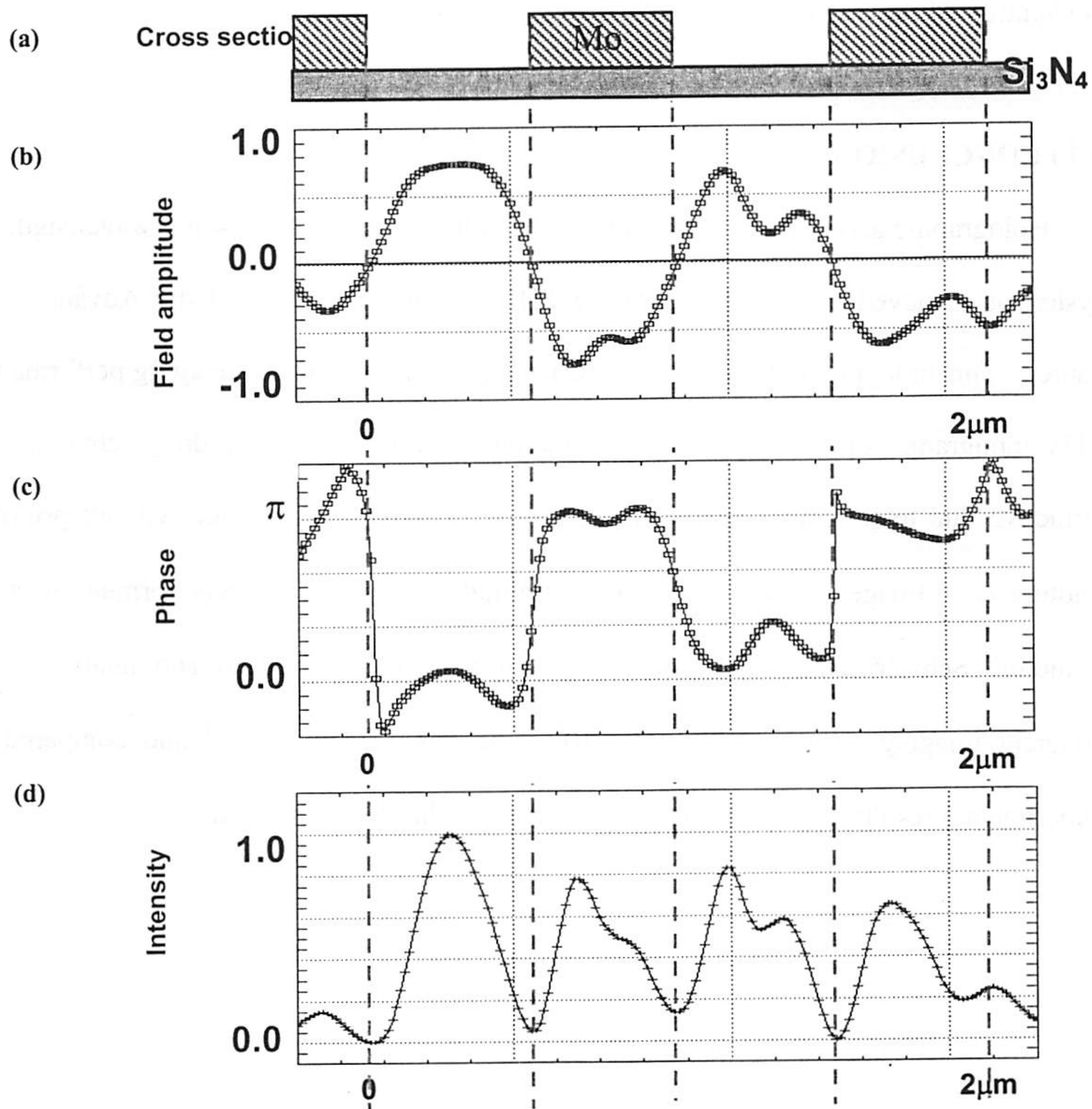

Fig. 3-22 Experimental results obtained with the phase-shift mask. (a) Cross-section view of the actual mask. (b) shows a cross-section plot of the electric-field, which is seen to go negative, and (c)shows the corresponding phase. π phase shifts are observed for Mo regions. (d) shows the intensity pattern obtained by the modulus squared of the plot (b), revealing frequency-doubling effect.

The intensity is the modulus squared of the field, and zero intensity points are observed between the normal and phase-shift regions due to the electric field amplitude crossing zero at the phase step. Thus, frequency doubling is evident when comparing the intensity image and the original object. This APSM is similar to chrome-less phase-shift masks used in conventional lithography to enhance optical resolution [86].

3.10 CONCLUSION

Holographic aerial image recording has been implemented at 13.4 nm wavelength. The system is achieved by modifying the PS/PDI at beamline 12.0.1 of the Advanced Light source. This holographic technique can be used to monitor coherent imaging performance of EUV lithographic optical systems. The holographic aerial image recording technique is also attractive due to its compactness and its ability to monitor the image without printing in photoresist. Images of various binary amplitude and phase objects formed by a 10×-reduction Schwarzschild EUV optical system have been recorded and analyzed. The coherent imaging performance of the 10×-optic has been simulated and compared with experimental results, and good qualitative agreement has been obtained.

Chapter 4

Spatial coherence measurement of synchrotron-based illuminators

4.1 INTRODUCTION..91
4.1.1 Two-pinhole experiment..92
4.1.2 Holographic coherence characterization..95

4.2 HOLOGRAPHIC COHERENCE MEASUREMENT OF SYNCHROTRON-BASED EUV ILLUMINATORS..98
4.2.1 Coherence of the K-B condenser system..100
4.2.2 Coherence of the pinhole illuminator..105

4.3 CONCLUSION..107

4.1 INTRODUCTION

The holographic aerial image recording technique is a powerful tool that can characterize both the amplitude and phase of coherent images. By applying the same idea with simple modifications, the holographic aerial image-recording tool can be further used to measure spatial coherence properties of illuminators. Such methods have been used for many years to characterize a variety of sources [95-102]. Understanding illumination coherence properties is crucial to the design of various systems. Scanning microscopy, crystallography, interferometry, and holography typically require fully coherent radiation while lithography normally utilizes partially coherent radiation. As new instruments and sources are developed at EUV, it is important to be able to quantitatively characterize their illumination coherence prosperities.

For radiation with well-defined propagation and high degree of coherence, like an undulator source, the coherence property can be separately characterized in the longitudinal (temporal) and transverse (spatial) dimensions. For an undulator source, the longitudinal coherence depends on the natural bandwidth of the undulator (N, the number of magnet period) and the monochromator exit slit gap in the beamline as described in section 2.3.1. However, calculating the spatial coherence at the output of a complicated optical system is a significantly more arduous task. The spatial coherence of undulator beamline 12.0.1 at the Advanced Light Source of Lawrence Berkeley National Laboratory, has recently been experimentally determined using the classic two-pinhole interference technique [56, 87], an extension of Young's two-slit experiments [57]. However, this technique requires the

interference pattern to be measured at a multitude of pinhole separations and locations in order to fully characterize the coherence properties.

In this chapter, a holographic technique for measuring coherence is presented and utilized to measure the coherence properties of Beamline 12.0.1 in various configurations. Unlike the two-pinhole method, the holographic method requires only a single measurement to characterize the coherence area. The holographic method effectively measures fringe contrast for all separations in parallel. It should be noted, however, that full coherence characterization in the non-stationary case requires multiple holographic measurement as well.

4.1.1 Two-pinhole experiment

The use of the Thompson and Wolf experiment to measure spatial coherence properties is described in Fig. 4-1. A spatially extended source S illuminates an opaque

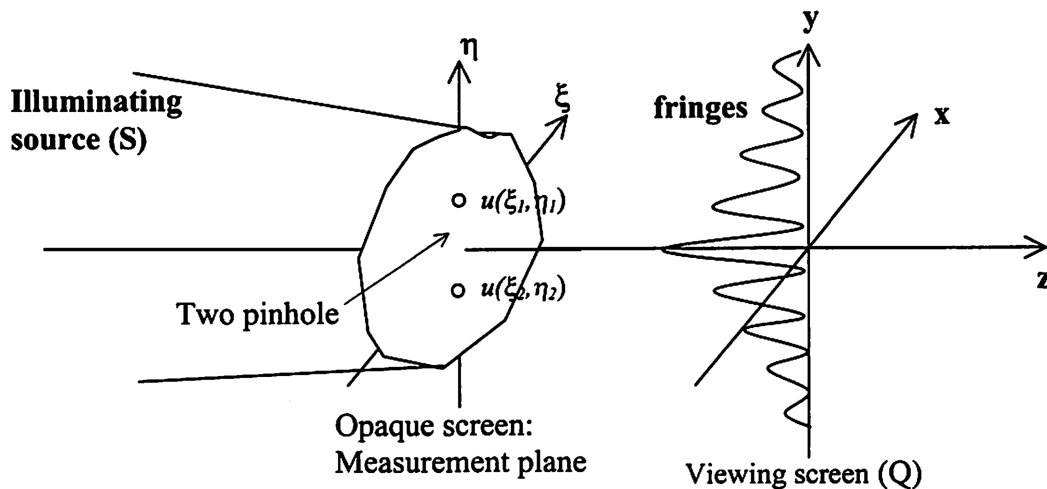

Fig. 4-1 Young's two-pinhole interference experiment. The fringe visibility recorded at the viewing screen indicates the spatial coherence of the illuminating source under the quasimonochromatic condition. In order to measure the coherence properties of the illuminating source, multiple measurements with different pinhole separations and locations are necessary.

screen containing two pinholes, and the viewing screen is placed behind the opaque screen at some distance z. The diffracted spherical wavefronts from the two pinholes generate a fringe pattern where the contrast is proportional to the mutual coherence of the light impinging on the two pinholes. Assuming temporal coherence effects to be negligible, the fringe contrast will be uniform across the viewing screen. This simply requires the coherence length to be large compared to the optical path length differences between the two pinholes and the area of interest on the viewing screen. Under this condition, the viewing screen intensity distribution can be written as

$$I_Q(x,y) = \langle u^*(x,y,t) \cdot u(x,y,t) \rangle, \qquad \text{Eq. 4-1}$$

where

$$u(x,y,t) = K_1 \cdot u(\xi_1,\eta_1,\tau) + K_2 \cdot u(\xi_2,\eta_2,\tau) \qquad \text{Eq. 4-2}$$

$u(\xi,\eta,\tau)$ and $u(x,y,t)$ are the electric fields at the opaque and viewing screen, respectively, and K_1 and K_2 are complex-valued constants. Thus, after manipulation, Eq. 4-1 can be written as

$$I_Q(x,y) = I_1 + I_2 + 2\sqrt{I_1 \cdot I_2} \cdot \mu_{12} \cdot \cos[\frac{2\pi}{\lambda z}(\Delta\xi \cdot x + \Delta\eta \cdot y) + \phi_{12}] \qquad \text{Eq. 4-3}$$

where I_1 and I_2 are the Airy intensity envelopes in the viewing plane due to pinhole diffraction, $\Delta\xi$ and $\Delta\eta$ correspond to the pinhole separation, $\phi_{1,2}$ is a constant phase term, and $\mu_{1,2}$ is the *complex coherence factor* [57]. The *complex coherence factor* is related to mutual intensity, $J_{12} = \langle u(\xi_1,\eta_1,\tau)u^*(\xi_2,\eta_2,\tau)\rangle$, with proper normalization and is a measure

of the mutual coherence of the light impinging on the two pinholes in the opaque screen. The spatial coherence of the light striking the pinhole plane can be obtained by measuring μ_{12} as a function of pinhole separation and position. Assuming stationarity, the position can be fixed and only various separations are required. When $\mu_{12} = 0$, the fringes at the viewing screen vanish, and two waves are said to be mutually incoherent. When $\mu_{12} = 1$, the waves are perfectly correlated and mutually coherent. Values of μ_{12} between 0 and 1 indicate the two waves are partially coherent. The constant phase term, $\phi_{1,2}$, describes the fringe shift relative to the center of the fringe pattern.

The *complex coherence factor*, μ_{12}, can be calculated directly from the fringe visibility.

$$V = \frac{I_{\max} - I_{\min}}{I_{\max} + I_{\min}} = \frac{2\sqrt{I_1 I_2}}{I_1 + I_2}\mu_{12} \qquad \text{Eq. 4-4}$$

assuming the relative intensities of the two waves to be known. This method requires measurements of the visibility at many different pinhole separations. Also, as stated above, the relative intensities of the two beams must be known or guaranteed to be equal.

Using this method, the coherence area of beamline 12.0.1 operating at 13.4 nm wavelength has been measured by C. Chang [56]. The measurements revealed the coherence distances of 6.3 μm and 7.4 μm in the horizontal and vertical directions, respectively, at the focal plane of the K-B illuminating system. The intensity distribution at the K-B focus equals to 11 μm (H) × 5 μm (V) (FWHM), and the natural beamline bandwidth is $\lambda/\Delta\lambda = 55$.

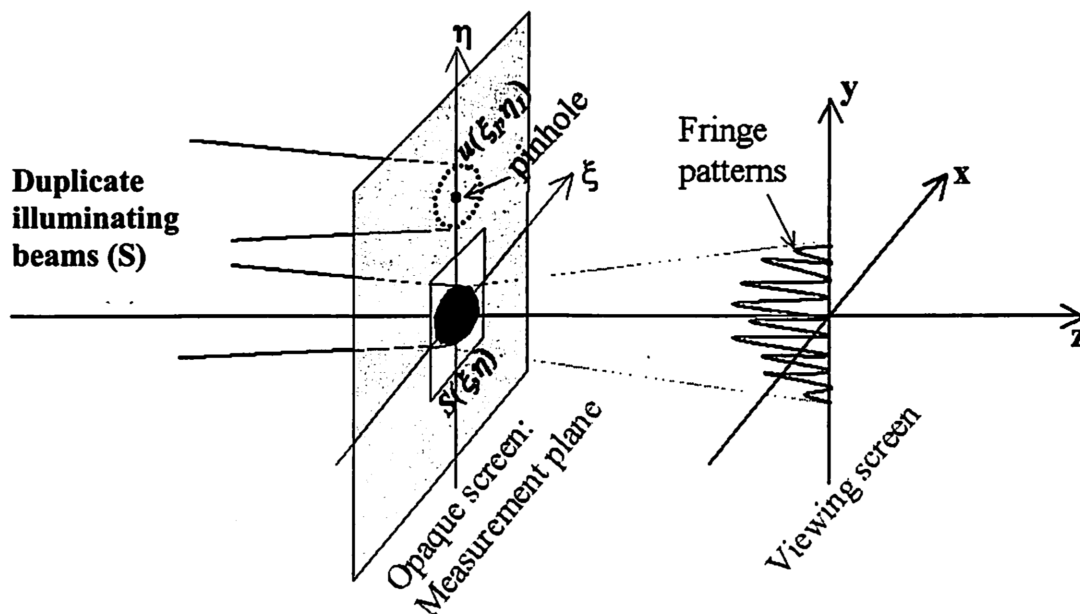

Fig. 4-2 Holographic coherence measurement. A single measurement can be performed to determine the coherence area with respect to the pinhole position. The method can be viewed as performing the two-pinhole test at all pinhole separations in parallel.

4.1.2 Holographic coherence characterization

Spatial coherence properties may also be characterized using the holographic method discussed in Chapter 3. In holography, only those portions of the object coherent with the reference are reconstructed. The holographic coherence measurement experiment is graphically described in Fig. 4-2. Two copies of the illuminations source, S, are required for the holographic method to measure coherence area. One illuminating beam strikes the pinhole, and the other illuminating beam passes through the open window in the opaque screen. Analogous to the aerial image monitoring, an off-axis Fourier-transform hologram of the illumination beam is recorded at the viewing screen.

The reference wave is derived from a single element of the source distribution; for simplicity we assume the central source element to be used. This reference wave is used to

record a hologram of the entire source distribution. Decomposing the source distribution into a series of points, it is evident that the hologram will only reconstruct those source points which are coherent with the reference wave (the central source point). In reality, the process is not binary; rather the reconstructed strength of the various source points will be proportional to the mutual coherence between each arbitrary source point and the central source point.

Alternatively, we can view the hologram as a superposition of fringe patterns created by the interference between the reference (the central source point) and the various other source points. Each source point will yield a unique fringe spatial frequency upon interfering with the reference. The contrast of that fringe pattern will depend on the mutual coherence between the reference and the given source point. This contrast translates to the strength of that particular point in the reconstructed image. The holographic method thus effectively and simultaneously performs the two-pinhole test at all possible pinhole separations. To measure non-stationary coherence properties, the holographic method would have to be repeated at a multitude of pinhole positions relative to the source.

Considering Fig. 4-2, the mathematical representations of the entire source and the central source point are $S(\xi_1,\eta_1)$ and $u(\xi_1,\eta_1) = S(\xi,\eta)\cdot\delta(\xi-\xi_1,\eta-\eta_1)$, respectively, where d is the duplicate source separation. Thus, using Eq.4-3, the mathematical representation of the fringe pattern or hologram captured on the viewing screen, $I_{QH}(x,y)$, can be written as

$$I_{QH}(x,y) = \int_1 \partial\Delta\xi\cdot\partial\Delta\eta\cdot I_{11} + 2\cdot J_{12}\cdot\cos[\frac{2\pi}{\lambda z}((d+\Delta\xi)\cdot x + (d+\Delta\eta)\cdot y) + \phi(\Delta\xi,\Delta\eta)]$$

Eq. 4-5

where $I_{11} = \langle u(\xi_1,\eta_1)\cdot u^*(\xi_1,\eta_1)\rangle$, $J_{12} = \langle u(\xi_1,\eta_1)\cdot u^*(\xi_2,\eta_2)\rangle$, $\Delta\xi=\xi_1-\xi_2$, $\Delta\eta=\eta_1-\eta_2$, and $\phi(\Delta\xi,\Delta\eta)$ is a constant phase factor. The mutual intensity, J_{12}, is essentially a mutual coherence function under quasimonochromatic conditions [57] for each source point located at (ξ_2,η_2). Reconstruction of the hologram, $I_{QH}(x,y)$, by taking Fourier-transform yields the total mutual intensity, $J_{12}(\xi_1,\eta_1;\xi_2,\eta_2)$. Therefore, the reconstructed mutual intensity represents the coherence properties of the illuminating source. This is almost equivalent to measuring fringe visibility in the two-pinhole experiments for all separations in parallel as explained above. The *complex coherence factor* for the holographic method, μ_{hol}, can be found by using the mutual intensity function, J_{12}, normalized with the illuminating beam intensity profiles, such as

$$\mu_{hol} = \frac{J_{12}}{\sqrt{I_1(\xi_1,\eta_1)\cdot I_2(\xi_2,\eta_2)}} \qquad \text{Eq. 4-6}$$

where $I_1(\xi_1,\eta_1)=J_{11}$ is the intensity at the central source point, and $I_2(\xi_2,\eta_2)=J_{22}$ is the intensity at the arbitrary point in the source. Therefore, if the intensity of the illuminating source is known, the *complex coherence factor* can determined.

4.2 HOLOGRAPHIC COHERENCE MEASUREMENT OF SYNCHROTRON-BASED EUV ILLUMINATORS

A schematic diagram of the holographic coherence measurement experiment is shown in Fig. 4-3. The experiment was performed at the EUV undulator beamline 12.0.1 at the

Advanced Light Source described in section 2.3.1. The experimental set-up is similar to the holographic aerial image recording experiments described in Chapter 3.

The setup in Fig. 4-3 is used to characterize the spatial coherence properties in the object plane of the holographic aerial image recording system. Two EUV illuminators are considered: a K-B condenser system and a pinhole illuminator (Fig. 4-4).

The reconstructed image from the hologram recorded on the CCD provides the 10× demagnified mutual intensity function of the illuminating source. The coherence area of the illuminating source can be determined from the reconstructed mutual intensity function normalized by the known intensity distribution.

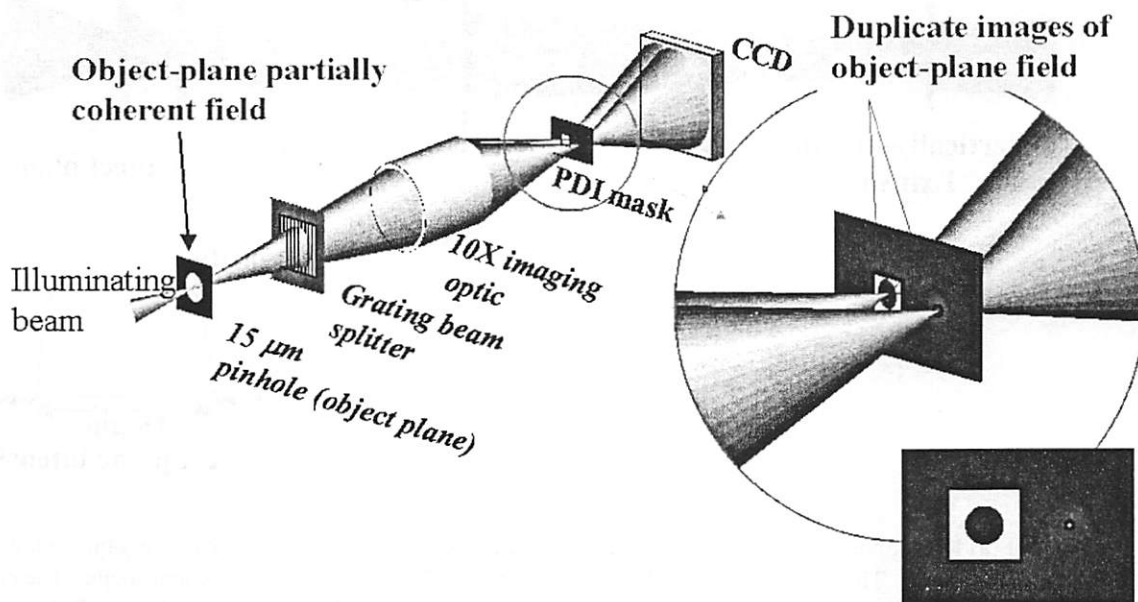

Fig. 4-3 Schematic diagram of the coherence characterization experiment. The hologram of the illuminating source is formed at the CCD camera. By reconstructing the hologram, the coherence area of the illuminating beam can be extracted.

(a)

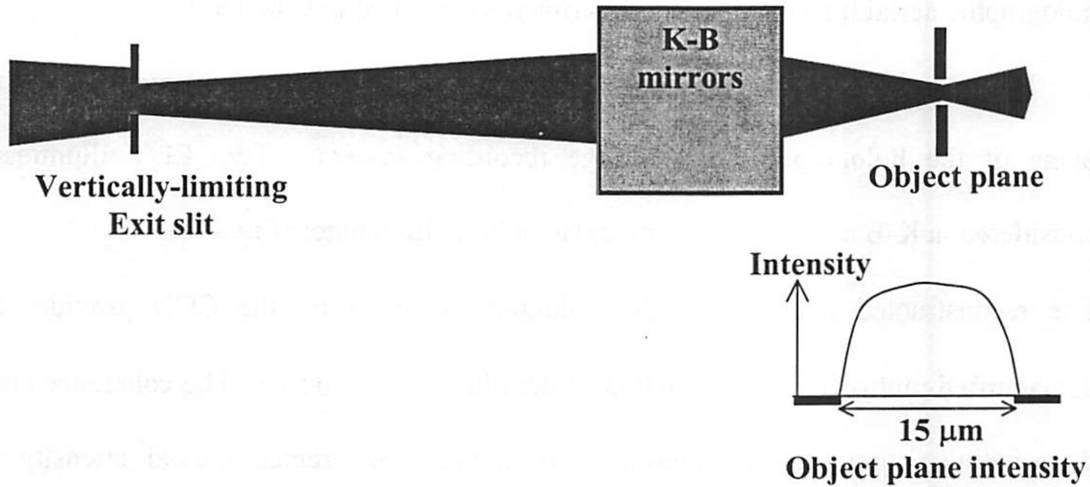

(b)

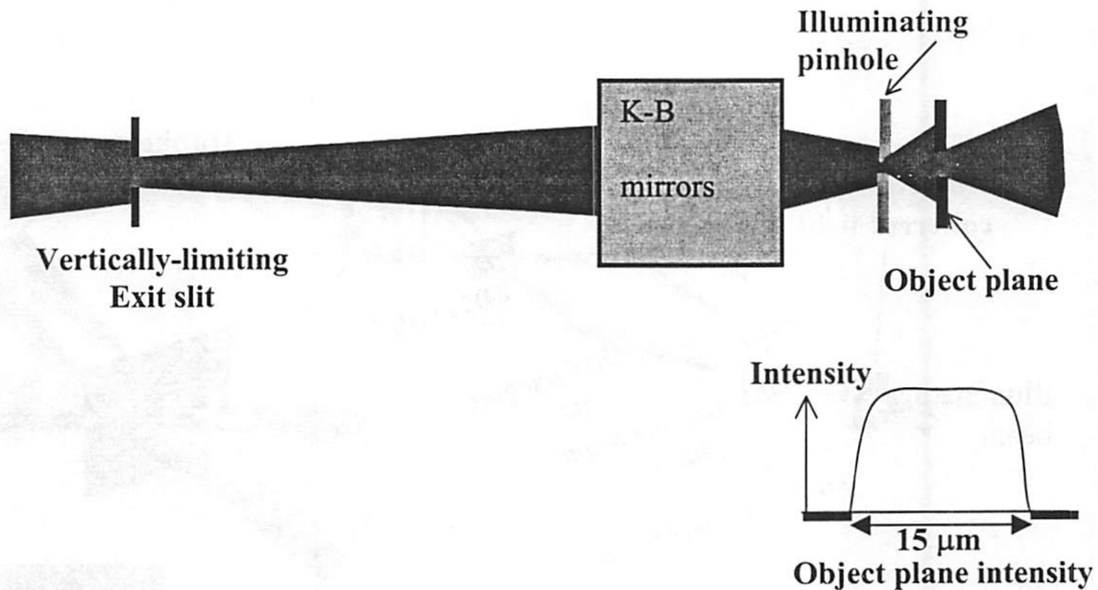

Fig. 4-4 (a) K-B condenser system. The focal plane of the K-B system coincides with the object plane of the imaging optic. The spot size (FWHM) is approximately 12 μm x 10 μm in elliptical shape. The cross section plot of the intensity profile over the 15-μm beam-defining circular aperture is shown. Relatively uniform intensity profile is observed. (b) Pinhole illuminating system. 1.4-μm pinhole is placed 15 mm before the object plane. The diffracted beam from the pinhole illuminates the object plane. The beam-defining circular aperture is placed at the object plane.

At the object plane, a relatively large circular aperture, 15-μm in diameter, is placed (Fig. 4.3) in order to define the illumination area of interest. Limiting the size of the

illuminating beam is required to maintain adequate separation of the multiple images of the source in the image plane. This experiment is functionally equivalent to the holographic technique described in Chapter 3 with the object of interest now being the raw illuminations beam or source. Reconstruction from the hologram is also performed using the techniques identical to those presented in Chapter 3.

4.2.1 Coherence of the K-B condenser system

The first illuminator considered was the standard Beamline 12.0.1 configuration, which uses a K-B system to reimage the undulator source to the test-optic object plane (a critical illuminator [57]). The beamline was set to operate at the undulator's natural bandwidth ($\lambda/\Delta\lambda$=55). This configuration sets the quasimonochromatic requirement allowing spatial coherence properties to be separated from temporal coherence properties.

In order to identify the coherence area of the illuminating source, its intensity profile at the object plane must be known or measured beforehand. The measured vertical and horizontal cross section profiles of the illuminating source at the object plane are plotted in Fig. 4-5. The object plane is intentionally moved out of the focal plane of the K-B illuminating system to achieve relatively uniform intensity at least over the source-defining aperture, the 15-μm diameter pinhole. From Fig. 4-5, the measured FWHM spot size for the K-B condenser system at the object plane is 94 μm (H) × 85 μm (V) in elliptical shape. Less than 10% peak-to-valley intensity variation is observed over 15-μm diameter central peak region of the K-B illuminating source at the object plane, allowing intensity effects to be safely ignored.

(a)

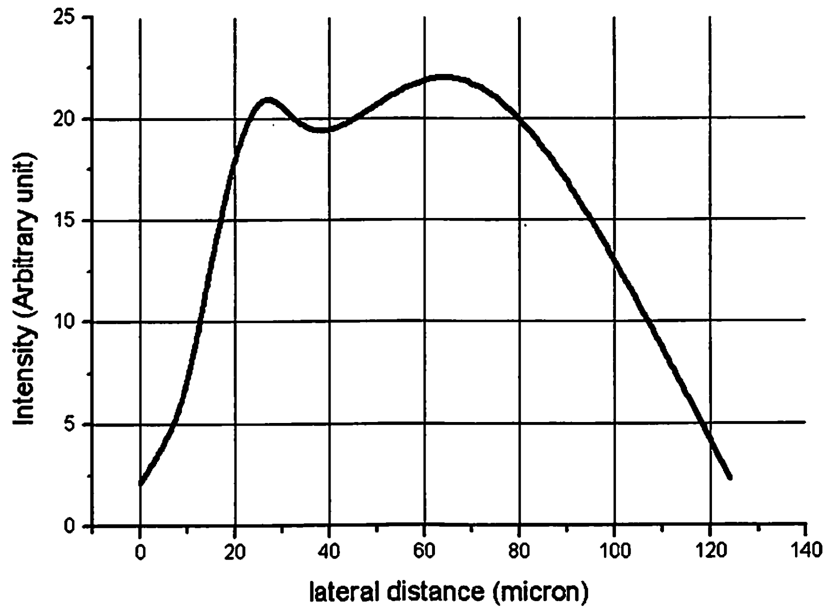

(b)

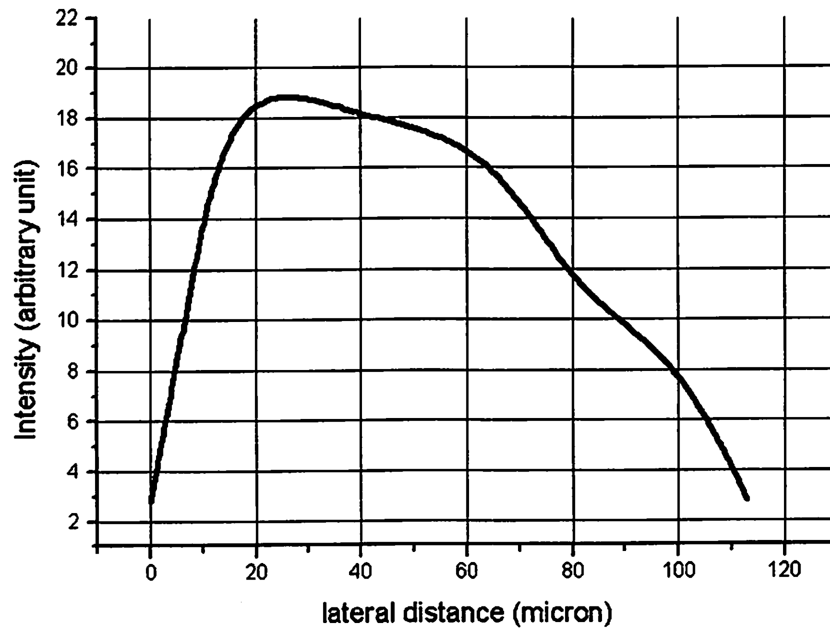

Fig. 4-5 The cross section profiles of the K-B illuminating beam at the object plane in (a) horizontal and (b) vertical directions. The FWHM spot size is measured to be 94 μm × 84 μm in elliptical shape. The beam size is much larger than the beam defining circular aperture placed at the object plane.

A representative hologram of the K-B illumination is shown in Fig. 4-6(a). Using the Fourier-transform method to reconstruct the 10× demagnified mutual intensity function yields the images shown in Figs. 4-6(b) and (c). The enlarged single-sidelobe image shown in Fig. 4-6(c) covers a 30 μm × 30 μm area. The reconstructed mutual intensity represents the spatial coherence of the illuminating source if the source intensity is assumed to be uniform. The reconstructed mutual intensity has an elliptical shape with a larger coherence distance in a vertical direction. These results are consistent with the increased spatial filtering imparted by the beamline in the vertical direction compared to the horizontal direction.

The properly scaled 15-μm circular aperture compared to the reconstructed mutual intensity is also indicated with the dotted line in Fig. 4-6(c). No features of the circular

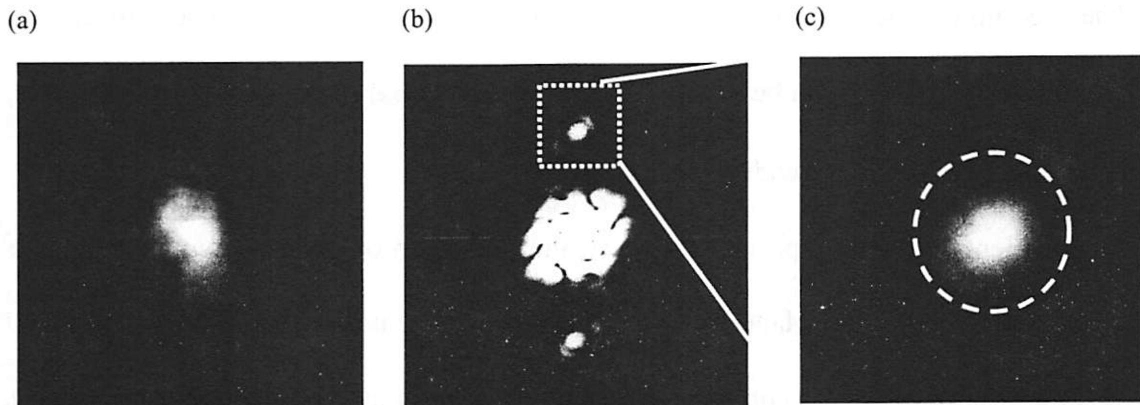

Fig. 4-6 The holographic coherence measurement results for the K-B condenser system obtained at the object plane. (a) The hologram of the image of the mutual intensity. (b) The FFT of the hologram. (c) The enlarged image of the mutual intensity function. The dashed line indicates the location of the 15-μm illumination-limiting aperture.

aperture can be observed in Fig. 4-5(c) as a result of the coherence width being smaller than 15 μm. If the entire illuminating beam were spatially coherent, detailed shapes of the beam-defining 15-μm circular aperture would be evident.

In order to precisely calculate the coherence area, the equivalent top-hat method has been used [57]. Noting that the modulus of the normalized mutual intensity depends only on the difference of coordinates ($\Delta\xi$, $\Delta\eta$), the coherence area, A_c, for the reconstructed 2-D mutual intensity can be calculated in a manner entirely analogous to the definition in [57]. The coherence width is obtained by determining the width of an equivalent top-hat function given by

$$A_c = \int\int_{-\infty}^{\infty} \left|\mu(\Delta\xi,\Delta\eta)\right|^2 d\Delta\xi \cdot d\Delta\eta \qquad \text{Eq. 4-7}$$

The measured coherence width of the K-B illuminator at the object plane from Eq. 4-7 is found to be 7.1 μm for the beamline 12.0.1 with the natural undulator bandwidth, $\lambda/\Delta\lambda$, of 55 (monochromator exit-slit width of 400 μm).

As mentioned in the previous chapter, the resolution of the holographic technique is set by the size of the image-plane pinhole. The pinhole size used in the experiment is ~100 nm, thus the resolution of the coherence width measurement at the object plane is ~1 μm. The reconstructed mutual intensity function shown in Fig. 4-6(c) includes convolution with a 1-μm diameter top-hat function. To measure coherence width smaller than 1 μm, the image plane pinhole size should be smaller than 100-nm.

It should also be noted that the measured coherence is based on the reimaged source distribution instead of the actual source distribution. The minimum measurable coherence area may, thus, be set by the resolution of the optic instead of the pinhole. For

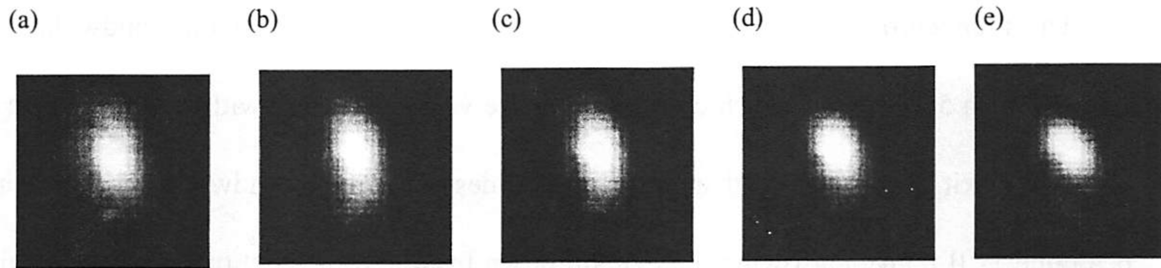

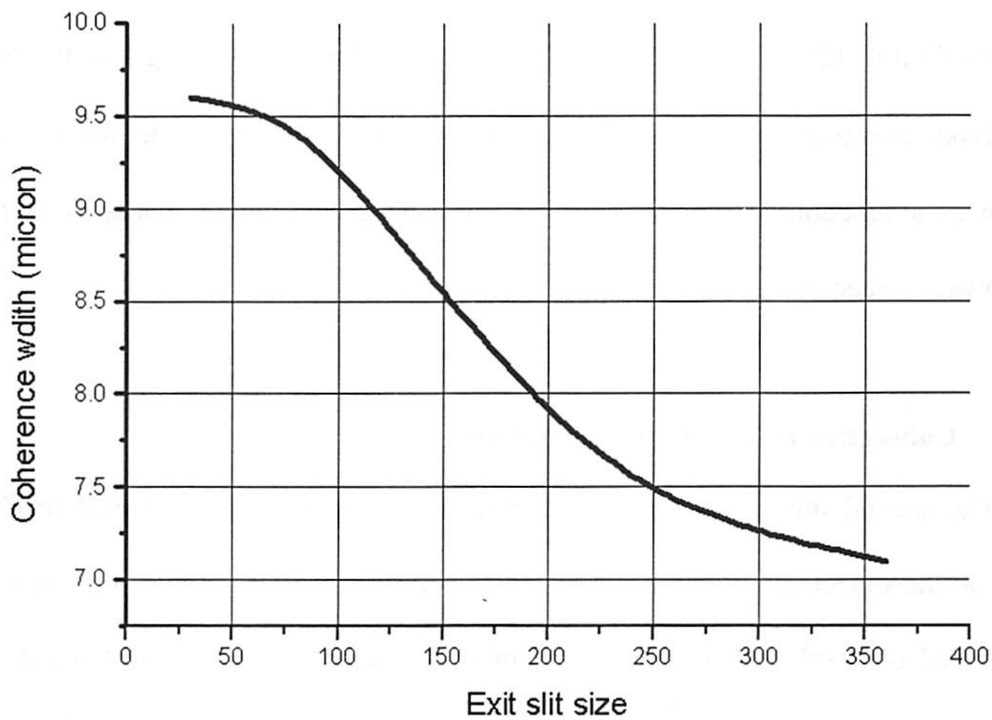

Fig. 4-7 The reconstructed mutual intensity of the K-B illuminator as a function of exit-slit width (a) 40-µm, (b) 80-µm, (c) 120-µm, (d) 160-µm, and (e) 240-µm. (f) Plot of the coherence width as a function of monochromator exit-slit size. The coherence width increases in the direction of exit-slit narrowing.

this method to be effective, it is important that the resolution of the optic to be considerably better than the expected coherence area. The requirement is readily met with the illuminator considered here.

The monochromator exit slit of the beamline is used to select the bandwidth ($\lambda/\Delta\lambda$) ranging from 55 to 1100, which correspond to the vertical exit slit width from 320 μm to 16 μm. The exit slit size wider than 320-μm provides the natural bandwidth for the undulator beamline 12.0.1. By narrowing the exit slit down from 320-μm, not only the spectrum ($\Delta\lambda$) of the propagated beam narrows, but also the spatial coherence in vertical direction increases. Figures 4-7(a) to (e) show the reconstructed coherence areas for the vertical exit slit gaps of 40 μm, 80 μm, 120 μm, 160 μm, and 240 μm respectively. The images of the reconstructed coherence area indicate 20 μm × 20 μm area. Figure 4-7(f) shows the plot of the coherence width as a function of the exit-slit size. The coherence width increases as the slit size narrows as expected.

4.2.1 Coherence of the pinhole illuminator

The second illuminator considered was the pinhole illuminator used in Chapter 3 to provide the object illumination. As seen in Fig. 4-4(b), the pinhole illuminator is simply comprised of a sub-resolution pinhole some distance before the object plane, so that the diffracted wave from the pinhole illuminates the object plane. The particular configuration characterized here uses a 1.4-μm illuminating pinhole placed 15-mm before the object plane as shown in Fig. 4-4(b). The FWHM beam spot size at the illuminating pinhole plane is measured to be approximately 100 μm in diameter. Using the result of the measured coherence area of the K-B illuminator at the object plane and the emission half angle (NA) of

the K-B system, the coherence width at the illuminating pinhole plane can be estimated. Because this coherence width is substantially larger than the 1.4-μm illuminating pinhole size, the pinhole-diffracted illumination of the object plane is expected to be fully coherent.

The FWHM spot size at the object plane is ~200 μm due to the diffraction from the illumination pinhole. Also, the peak-to-valley intensity variation over the 15-μm diameter measurement area defined by the 15-μm object-plane pinhole is less than 8%, allowing intensity variation to be ignored in the determination of the coherence area. The measurement was performed with the monochromator exit slit width of 400-μm, which corresponds to the natural undulator bandwidth, $\lambda/\Delta\lambda$, of 55.

A representative hologram of the pinhole illumination is shown in Fig. 4-8(a). Using the Fourier-transform method to reconstruct the mutual intensity of the illuminating source yields the images shown in Figs. 4-8(b) and (c). The enlarged single-sidelobe image is shown in Fig. 4-8(c) covers a 30 μm × 30 μm area. In contrast to the mutual intensity function of the K-B illuminating system shown in Fig. 4-6(c), the circular aperture, which is used as a beam-defining aperture for the illuminating source, is completely reconstructed.

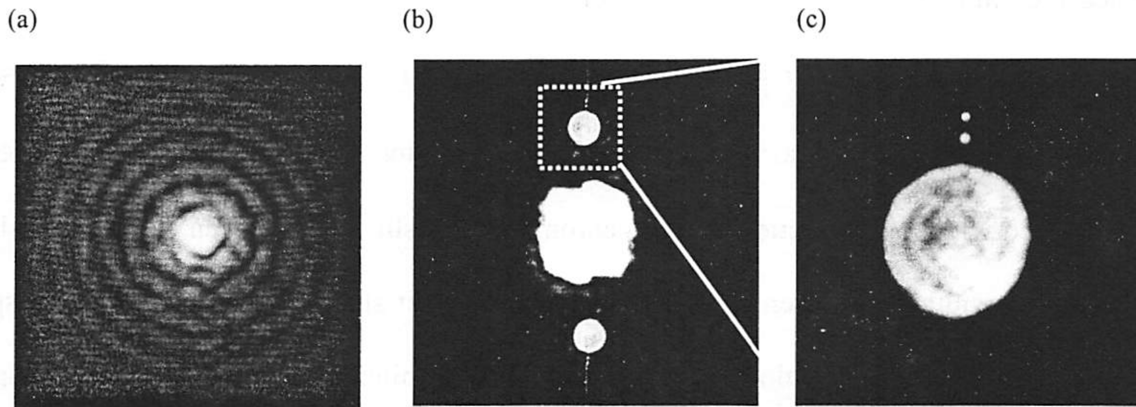

Fig. 4-8 Holographic coherence measurement results for the pinhole illuminator. (a) The hologram of the image of the mutual intensity. (b) The FFT of the hologram. (c) The enlarged image of the mutual intensity function. The full 15-μm-diameter illumination limiting aperture is reconstructed, indicating the coherence area to be larger than 15-μm in diameter.

Sharp edges and uniform intensity throughout the reconstructed image of the circular aperture are observed, indicating that the coherence area is larger than the object-plane aperture (15-μm in diameter).

It should also be noted that The objects used in the holographic aerial image recording experiments (Chapter 3) were typically 25 μm × 25 μm, and full reconstructions of the images with sharp features were achieved as seen in Figs. 3-8 through 15. This further indicates that the coherence width of the pinhole illuminator at the object plane is even larger than the object size used in the holographic aerial image recording experiments. As stated above, based on the fact that the illuminator pinhole is smaller than the measured K-B coherence area, one would expect the pinhole illumination to be fully coherent.

4.3 CONCLUSION

The holographic aerial image recording technique has been adopted to measure coherence areas of two EUV illuminator systems. Unlike the classic two-pinhole experiments used to measure coherence properties, the holographic method effectively measures all pinhole separations in parallel.

For the K-B condenser system, a coherence width of 7.1 μm at the object plane has been measured with the natural bandwidth of the undulator, $\lambda/\Delta\lambda = 55$. Furthermore, the coherence width as a function of monochromator exit-slit size has been studied, and larger coherence widths have been measured with smaller exit slit gaps due to increase in spatial coherence in vertical direction. Characterization of the pinhole illuminator used in Chapter 3 supports the prediction of fully coherent illumination.

Chapter 5

Holographic microscopy to characterize EUV-mask-blank defects

5.1 INTRODUCTION ... 109
5.1.1 Defects in EUV multilayer-mask-blanks ... 109
5.1.2 EUV holographic microscopy for characterization of EUV-mask-blank defects ... 110
5.1.3 EUV multilayer-mask-blank defect inspection tool ... 112

5.2 A PROOF OF PRINCIPLE EXPERIMENT ... 114
5.2.1 Experimental configuration ... 114
5.2.2 Transmission mask ... 116

5.3 EXPERIMENTAL RESULTS ... 119
5.3.1 Reconstruction of the Fresnel hologram ... 119
5.3.2 Mathematical description of the hologram reconstruction process ... 120
5.3.3 Results with a null mask ... 126
5.3.4 Reconstructed images of program defects ... 128

5.4 CHARACTERIZATION OF PHASE DEFECTS ... 131

5.5 CHARACTERIZING REFLECTION MASKS: PROPOSED SYSTEM ... 131
5.5.1 Multilayer bandpass issues ... 133
5.5.2 45° mirror and order sorting aperture ... 133
5.5.3 Holographic optical element: a beam-splitting grating ... 135

5.6 CONCLUSION ... 136

5.1 INTRODUCTION

5.1.1 Defects in EUV multilayer-mask-blank

Unlike the conventional chrome-on-quartz transmission mask used in the optical lithography, the mask architecture for EUV lithography is reflective, consisting of an absorber pattern on top of a multilayer reflection coating deposited onto a robust substrate such as a Si wafer or glass plate. The multilayer consists of 40-bilayers of Mo/Si or Mo/Be deposited by ion-beam sputtering with peak reflectivity around 13.4 nm or 11.5 nm. The absorber pattern is inspected for defects using mask inspection tools and is repaired as needed using focus ion beam techniques. The defect inspection tools include defect detection tools and defect characterization tools. The defect detection tools are based on light scattering (KLA/Tencor SP1, ADE Constellation AWIS, and EUV defect scanner). Defect characterization is provided by a suite of defect metrology tools including a DI-9000 AFM. A LEO SEM, and a Leica optical microscope. These characterization tools are used to measure accurate physical dimensions of defects with detailed morphology and chemical deposition for certain sizes of defects. The defect inspection tools are explained in section 5.1.3.

A significant concern for the commercial viability of EUV lithography is defect control on the requisite reflective multilayer mask blanks [89]. Because there are no known methods to correct defects in and on a multilayer, it is crucial to identify the defects providing feedback for the development of a nearly zero-defect multilayer mask fabrication process.

The major goal for mask blanks is to eliminate printable defects, and the ultimate target is the economical fabrication of defect-free masks. The coating defects of the multilayer-mask-

blank are divided into phase and amplitude defects. Defects in or below the multilayer can disrupt the multilayer which reduces the reflectivity and form amplitude defects. The phase defects occur when the multilayer grows conformally over a substrate defect [Fig. 5-1(a)]. The schematic diagram of amplitude and phase defects in the multilayer mask is shown in Figs. 5-1(b) and (c), respectively. These amplitude and phase defects on the EUV multilayer-mask-blanks can severely degrade the aerial image of the final features at the wafer plane [90,91].

5.1.2 EUV holographic microscopy for characterization of EUV-mask-blank defects

As described in previous chapters, the holographic aerial image recording technique can be used to characterize the coherent imaging performance of EUV imaging optics and the spatial coherence of EUV illuminators. By modifying the concept of the holographic aerial image recording technique, defects on EUV multilayer mask blanks can be also characterized [88]. In previous chapters, holograms of re-imaged object distributions were recorded. It is also possible, however, to record holograms of objects placed directly in the image plane, using the optic only as an illumination device. In this case, the system can be used as a holographic microscope. For example, if we consider a defect (phase or amplitude defect) on an EUV multilayer mask blank as an object, the hologram of the defect can be recorded, and, upon reconstruction of the hologram, the defect can be characterized.

A schematic of the holographic microscope for multilayer defect characterization is shown in Fig. 5-2. The system is very similar to the PS/PDI system except for the image plane mask. The 10×-Schwarzschild optic is used as an objective lens, and an image of the

pinhole source is formed at the image plane. The reference and the object waves are again generated by a grating beam splitter.

(a)

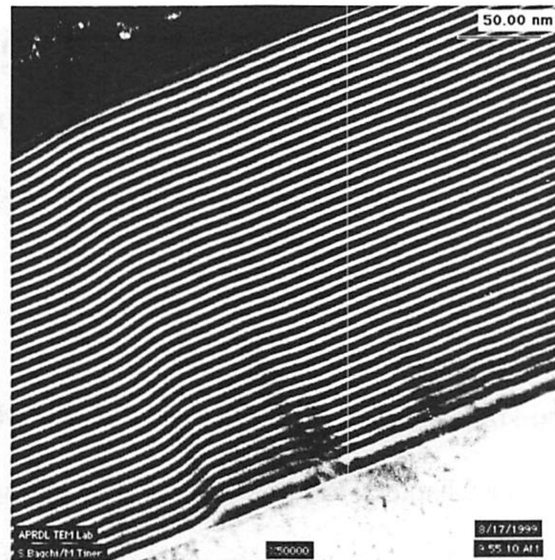

(b)

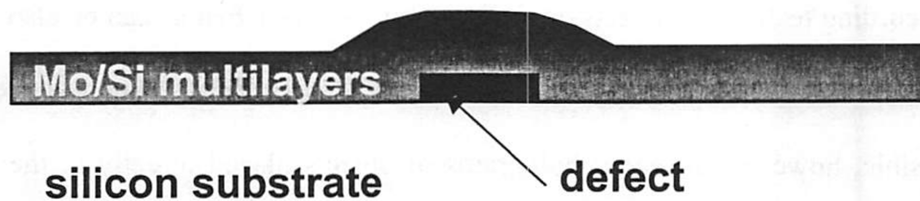

(c)

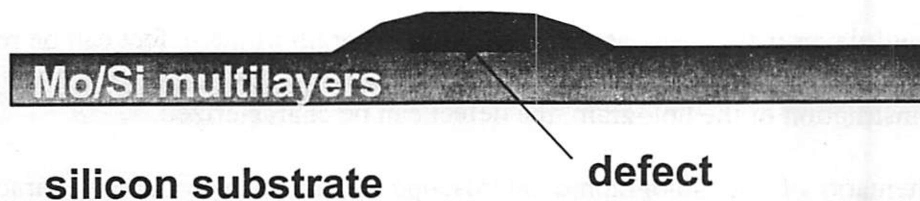

Fig.5-1 (a) TEM picture of a Mo/Si multilayer cross-section. The substrate has a step defect and the multilayer is seen to grow conformally, leading to a phase step upon reflection. (b) A diagram of a phase defect. The phase defects can be generated by conformal multilayer bumps resulting abrupt phase changes in the reflected electric field. (c) A diagram of an amplitude defect. The amplitude defect reduces the reflectivity of the multilayer.

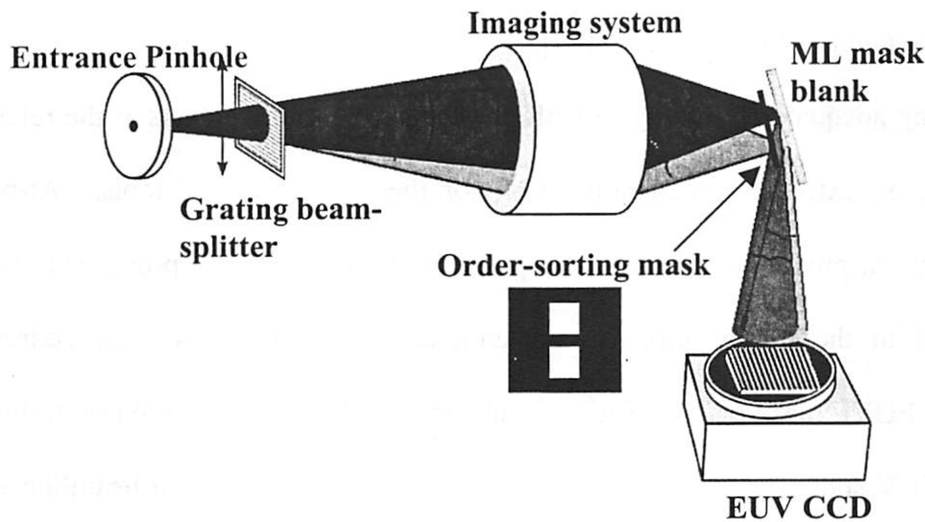

Fig. 5-2 Schematic diagram of a holographic microscope to characterize defects on EUV multilayer mask blanks. The correct angles of the reflected beams are not shown.

At the image plane of the optic, the EUV multilayer mask blank to be inspected is placed, and a hologram of the defect on the mask is formed at the CCD camera. Upon reconstruction of the hologram, the defect on the mask can be characterized (i.e. its location, shape, and size). Amplitude or phase defects can be characterized since the hologram reveals both phase and amplitude information.

5.1.3 EUV multilayer-mask-blank defect inspection tool

Tremendous progress towards the zero-defect goal has been achieved using conventional wafer inspection methods as the feedback mechanism for EUV multilayer-mask-blank fabrication [89]. EUVL mask-blanks can be scanned with a focused laser probe (λ = 488 nm) before and after multilayer coating with commercial optical tools (KLA/Tenco SP1 and ADE Constellation AWIS) to detect the defects [89]. Other metrology tools such as AFM,

SEM, and visible microscopy have been used to measure physical dimensions, morphology, and chemical composition of defects [89].

Obtaining adequate sensitivity to both phase and amplitude defects at the relevant sizes, however, is an extremely challenging task for these conventional tools. At-wavelength characterization, providing a more direct probe of the EUV optical properties of defects, is thus crucial to the optimization of conventional metrology tools. To address the at-wavelength EUVL mask bank inspection problem, an EUV scanner based on raster scanning a focused EUV spot along the EUV mask-blank has been developed at beamline 11.0 of the Advanced Light Source at the Lawrence Berkeley National Laboratory [92]. This system has the capability of identifying the locations of both amplitude and phase defects on multilayer mask blanks. Even though the EUV defect scanner is based on the same idea as the visible light detection systems, it is possible for the at-wavelength tool to probe the defects which cannot be detected with the conventional methods.

To enhance the at-wavelength system's capability to characterize defects, it would be desirable to add a holographic microscope to the scanner. In this combined device, the defects would be located using the EUV defect scanner and then characterized using the built-in holographic microscope. The holographic method is of particular interest because few other methods can quantify both the phase and amplitude of sub-micron sized defects on EUV mask blanks at wavelength. Using holographic microscopy, the locations, morphologies, shapes, and sizes of the phase and amplitude defects can be identified.

To understand the effects of multilayer deposition over a defect, a multilayer growth model has been developed [104-106]. This model has been used to investigate the complex questions ranging from defect formation on the substrate to defect printability [104]. The

simulation was based on taking a given substrate defect, simulating the multilayer growth over the defect, simulating the electromagnetic field in and directly above the multilayer, and finally calculating the image of the defect as produced by the optic in the wafer plane. The accuracy of this simulation depends strongly on accurate knowledge of the reflected electric field at the surface of the multilayer. Another important capability of the holographic microscope would be to verify the defect growth modeling results and in turn verifying the accuracy of the defect printability simulations. Upon agreement between the simulations and the holographic microscope results, the entire simulation process would be more reliable, and the simulation results can be used to identify the printable defects.

In this chapter, the concept of using the holographic microscope as an EUV mask-blank defect inspection tool is validated by characterizing programmed defects on simple transmission masks. In this proof-of-principle demonstration, we consider amplitude defect sizes ranging from 500 to 70 nm. Extension of this technique to the more relevant reflection mask configuration is further discussed.

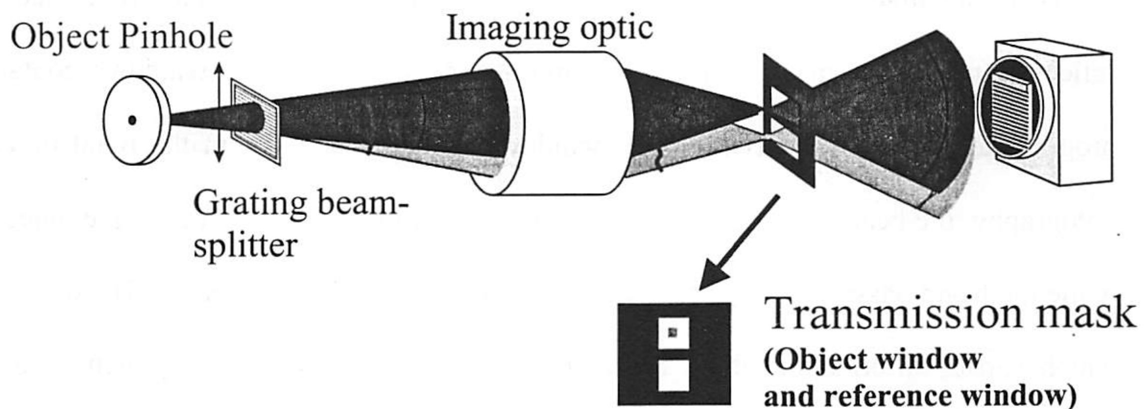

Fig. 5-3 A schematic diagram of a holographic microscopy system to characterize a program defect in a transmission mask. The system is obtained by slight modification of the PS/PDI system. The imaging optic is illuminated with uniform coherent light.

5.2 A PROOF OF PRINCIPLE EXPERIMENT

5.2.1 Experimental configuration

The schematic diagram of the proof-of-principle transmission configuration is shown in Fig. 5-3. The system, which is implemented by modifying the EUV PS/PDI described in Chapter 2, is based on the principles of lensless Fourier-transform holography described in Chapter 3 and references [80] and [81].

A spatial filtering pinhole is used to produce a spatially coherent spherical wavefront that illuminates the imaging optic. The pinhole size is chosen to yield relatively uniform illumination within the entrance pupil of the optic. A transmission grating is inserted between the object pinhole and the imaging optic to act as a beam splitter, producing multiple, laterally displaced, focal points in the image plane of the optical system. The imaging optic used in this experiment is Camera B2, a Schwarzschild objective, with 10× demagnification. The wavefront quality of the optic, as measured by the PS/PDI, is approximately $\lambda/20$ rms over 0.088 NA at the operational wavelength of 13.4 nm as shown in Chapter 2.

Near the image plane of the optic, the transmission mask is placed instead of the reflective multilayer mask. In the transmission mask, one of the windows contains the programmed defect whereas the other window has no defect. From the point of view of holography, the beam passing through the window with the defect serves as the object beam while the beam passing through the clean window serves as the reference. The object beam, which carries information about the defect, and the reference beam, which is simply a diverging spherical beam, interfere to generate a hologram on the CCD detector placed approximately 100 mm from the image plane. The hologram captures a record of the

complex-valued diffraction pattern created by the defect and can be used to reconstruct an image of the defect itself. The required exposure time is usually less than 1 sec.

5.2.2 Transmission mask

A transmission mask containing two windows is used to select two of the orders diffracted by the grating (used as an order-sorting mask). The rest of the mask is made opaque in order to block all remaining grating-order terms avoiding confusion in the data analysis. The transmission mask used here is different from the mask used in the PS/PDI and holographic aerial image recording experiments. A schematic diagram of the transmission mask is shown in Fig. 5-4.

The two windows have dimensions of 2.5 μm × 2.5 μm each with a center-to-center separation of 5 μm. The center-to-center separation is 2 times the window width preventing overlap between the holographic image and the zero order image as described in section 3.4. The object window contains programmed square amplitude defects with sizes ranging from 500 to 70 nm.

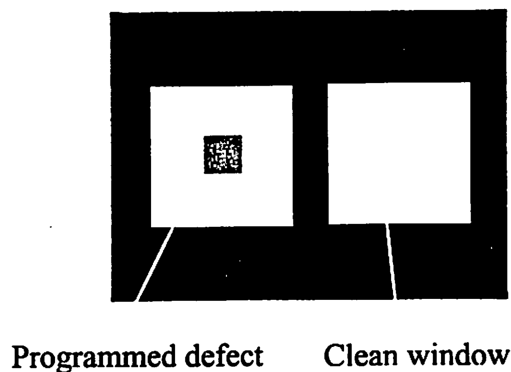

Fig.5-4 Schematic diagram of a programmed-defect mask. A programmed defect is placed at the object window while the reference window is kept clean.

An SEM picture of a test mask with a 300 nm programmed defect is shown in Fig. 5-5(a), and a diagram of the transmission mask cross-section is shown in Fig. 5-5(b). The mask is fabricated onto a 1000-Å Si_3N_4 membrane using electron beam lithography. The EUV attenuation for opaque areas of the mask and the programmed amplitude defects is provided by a 1000-Å-thick film of photoresist. Use of photoresist as the attenuation medium facilitated the mask-fabrication process.

The transmission mask can be placed anywhere between the image plane and the CCD camera plane depending on the beam separation, size of the windows, and inspecting area. If the mask is placed in the image plane, the spot size is ~100 nm for the Camera B2 optic. Thus, in order to characterize a large sized defect, the beam at the image plane would have to be scanned over an area spanning the defect. When the mask is placed at the image plane, the recorded hologram is a Fourier-transform hologram as described for the aerial image recording experiments. In this case, a simple Fourier transform is required to reconstruct the image of the defect.

(a)

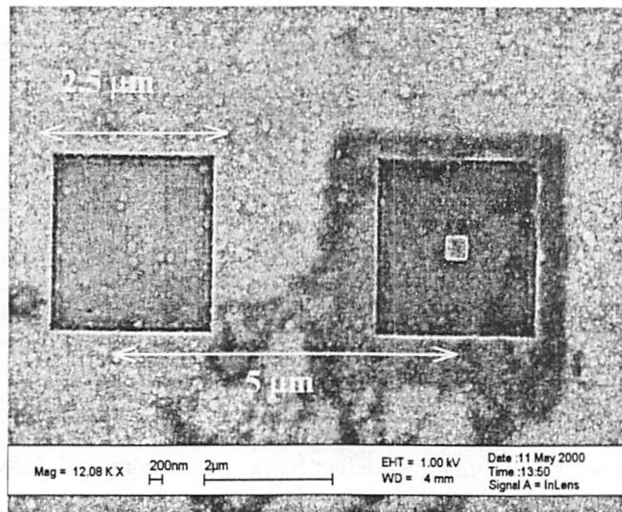

(b)

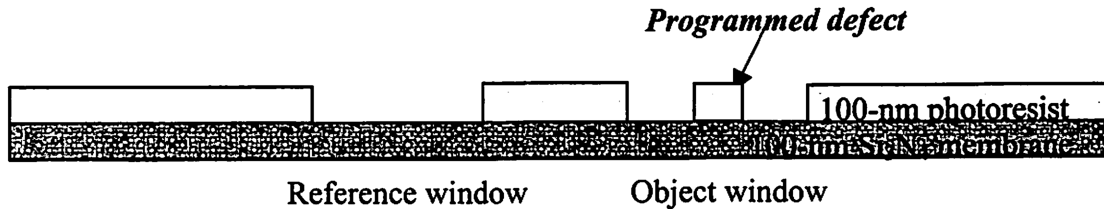

Fig.5-5 (a) A SEM picture of a transmission mask used in the experiment. (b) The diagram of the transmission mask cross-section. The photoresist was used for necessary EUV attenuation on top of nitride membrane. The object window contains square defects sized from 500-nm to 70-nm, and the defects are amplitude defects and also made with the photoresist

In practice, the mask is placed about 12-μm beyond the image plane (Fig. 5-3), allowing a larger window area to be directly observed. In this way, large or multiple defects may be characterized in parallel, minimizing the need for scanning the probe beam across the area of interest. The illuminating beam size at the mask plane is about 2.3-μm in diameter. This size is chosen to be larger than any defect size of interest yet smaller than the size of the window itself.

5.3 EXPERIMENTAL RESULTS

5.3.1 Reconstruction of the Fresnel hologram

Because the defect in the transmission mask is placed out of the focal plane of the imaging optic, the recorded hologram is not, strictly speaking, a Fourier-transform hologram. The hologram recorded for this configuration is a Fresnel hologram, and it is described in section 3.3 and reference [77].

The schematic diagram of the experimental geometry to acquire Fresnel holograms of programmed defects is shown in Fig. 5-6. In Fig. 5-6, *plane O*, *plane M*, and *plane R*

correspond to the image, mask, and recording planes, respectively. The distance between *plane O* and *plane M* is z_1 and *plane M* and *plane R* is z_2, and z_2 is much larger than z_1 ($z_2 >> z_1$). The reference beam $[U(u,v)_{ref}]$ passing through the clean window of the transmission mask and the object beam $[U(u,v)_{obj}]$ diffracted from the programmed defect form a Fresnel hologram $[H(u,v)]$, at *plane R*. Our goal is to reconstruct the programmed defect from the recorded hologram.

In order to reconstruct the Fresnel hologram, only the Fresnel propagation integral [77] is necessary. There are two methods to reconstruct the recorded Fresnel hologram. The first method is a single Fresnel propagation method, by which the programmed defect can be reconstructed by using a single Fresnel propagation integral of the recorded hologram from the recording plane to the mask plane. The second method is a combination method which utilizes the Fresnel propagation integral with a Fourier transform. The Fresnel propagation method is useful if the distance between the recording plane and the mask plane is precisely

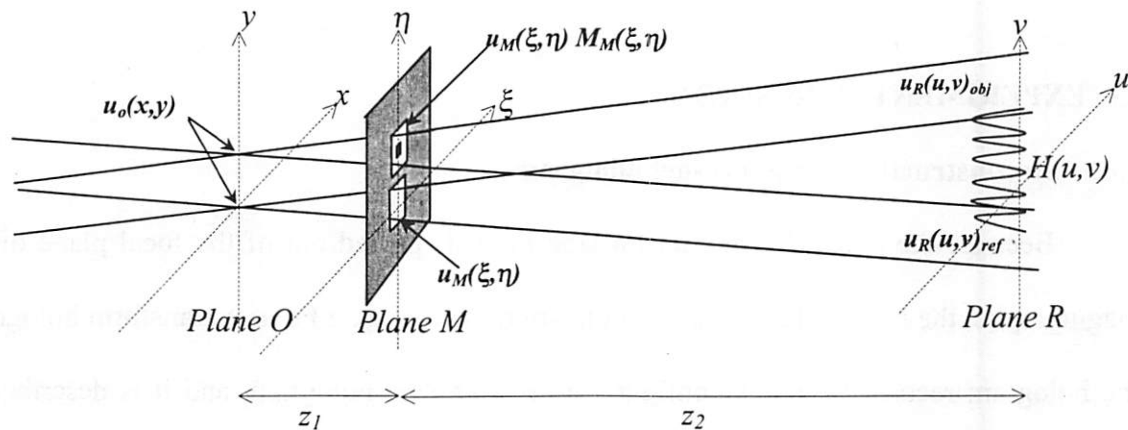

Fig. 5-6 Schematic Fresnel hologram recording geometry. Plane *O*, *M*, and *R* indicate image plane, mask plane, and recording plane respectively.

known within a few microns or better. Since only a single propagation integral is needed, this method can be fairly simple. However, in practice, the distance between the recording plane and the mask plane, z_2, cannot be measured with the accuracy required here. Thus, the combination method is used to reconstruct the programmed defects from the recorded Fresnel holograms. The combination method requires the precise knowledge of z_1, the distance between the *plane O* and *plane M*, however, an accurate measure of z_1 can be directly obtained in-situ using an accurate mask positioning stage to first position the mask in focus and then move it longitudinally a known amount.

5.3.2 Mathematical description of the hologram reconstruction process

The combination method used to reconstruct the programmed defects from the recorded holograms is described as follows. Simple Fourier-transform processing would reconstruct the field in the image plane (*plane O*) whereas we are interested in the field in the mask plane (*plane M*) where the programmed defect is located. From the field in the image plane (*plane O*), we can readily calculate the field in the mask plane (*plane M*) by Fresnel propagation.

We now describe the process mathematically. In *plane O*, we simply have multiple, laterally-displaced, copies of the optic PSF, $u_o(x,y)$. Similar to Eq. 3-1 in Chapter 3, the propagation of the reference beam from *plane O* to *plane R* through the clean window at *plane M* can be written as follows

$$u_R(u,v)_{ref} = c \cdot \iint_{-\infty}^{\infty} u_o(x,y) \cdot \exp\left\{ \frac{k}{2(z_1+z_2)} [(u-x)^2 + (v-y)^2] \right\} dx \cdot dy \qquad \text{Eq. 5-1}$$

where $u_R(u,v)_{ref}$ is the electric field at *plane R* for the reference beam, c is a constant, and k is the wave number ($2\pi/\lambda$). We assumed the clean window to be a perfect membrane (free from any defects or aberrations), which does not corrupt the propagating field. Equation 5-1 is a convolution and can be rewritten as

$$u_R(u,v)_{ref} = \int_{-\infty}^{\infty}\int_{-\infty}^{\infty} u_o(x,y)h(u-x,v-y)dxdy = u_o(x,y) \otimes h(u,v,z_1+z_2)|_{z=z_1+z_2}$$

Eq. 5-2

where the convolution kernel is

$$h(u,v,z_1+z_2) = c \cdot e^{\frac{jk}{2(z_1+z_2)}(u^2+v^2)}$$ Eq. 5-3

With further simplifications of the convolution integral using the paraxial approximation, the reference wave at the recording plane, $u_R(u,v)_{ref}$, can be expressed as

$$u_R(u,v)_{ref} = e^{\frac{jk}{2(z_2+z_1)}(u^2+v^2)} \cdot \int_{-\infty}^{\infty}\int_{-\infty}^{\infty} u_O(x,y) \cdot e^{-\frac{jk}{z_2}(ux+vy)} dxdy$$ Eq. 5-4

$$u_R(u,v)_{ref} = e^{\frac{jk}{2(z_2+z_1)}(u^2+v^2)} \cdot F.T.\{u_O(x,y)\}$$

Thus, the reference beam at *plane R* after passing through the clean window is simply the Fourier transform of the PSF.

By using similar arguments, an expression for the object beam containing the information about the programmed defect can be obtained. Using Eqs. 5-1 and 2, the electric field, $u_M(\xi,\eta)$, propagated from the image plane (*plane O*) to the mask plane (*plane M*) can be written as

$$u_M(\xi,\eta) = u_O(x,y) \otimes h(\xi,\eta,z) \qquad \text{Eq.5-5}$$

where $h(\xi,\eta)$ is the same convolution kernel form as described in Eq. 5-3, over distance z_1 instead of z_1+z_2. The programmed defect in *plane M* can be expressed as $M_M(\xi,\eta)$. Thus, the electric field right after the transmission mask can be written as

$$u_t(\xi,\eta) = u_M(\xi,\eta) \cdot M_M(\xi,\eta) \qquad \text{Eq. 5-6}$$

Now, in order to find the electric field at *plane R*, $u_t(\xi,\eta)$ needs to be further propagated from *plane M* to *plane R*, using the similar propagating integral as Eq. 5-1. Thus the electric field at the recording plane, $u_R(u,v)_{obj}$, can be shown as

$$u_R(u,v)_{obj} = e^{\frac{jk}{2z_2}(u^2+v^2)} \cdot \int_{-\infty}^{\infty}\int_{-\infty}^{\infty} u_t(\xi,\eta) \cdot e^{\frac{jk}{2z_2}(\xi^2+\eta^2)} e^{-\frac{jk}{z_2}(u\xi+v\eta)} d\xi d\eta \qquad \text{Eq.5-7}$$

The integral shown in Eq. 5-7 with arbitrary $M_M(\xi,\eta)$ can be very complicated and hard to perform. Therefore, it is easier to consider the electric field of the object beam at the image plane rather than the mask plane. It only takes a Fourier transform to propagate the object

beam from the image plane to the recording plane as described in Eq. 5-4, because the object and the reference beams are essentially diverging spherical waves originated from the image plane.

The electric field of the object beam at *plane M*, $u_t(\xi,\eta)$, can be transferred to *plane O* by using the transfer function given in Eq. 5-3. Thus, the electric field of the object beam at *plane O* containing information about the program defect is

$$u_O(x,y)_{obj} = u_t(\xi,\eta) \otimes h(x,y,z_1) = [u_M(\xi,\eta) \cdot M_M(\xi,\eta)] \otimes h(x,y,-z_1) \qquad \text{Eq. 5-8}$$

Now, let's propagate the object beam from *plane O* to *plane R*. By using the same diffraction integral used to get Eq. 5-4 with paraxial approximations, the electric field of the object beam at the recording plane, $u_R(u,v)_{obj}$, can be written as

$$u_R(u,v)_{obj} = e^{\frac{jk}{2(z_2+z_1)}(u^2+v^2)} \cdot F.T.\{[u_M(\xi,\eta) \cdot M_M(\xi,\eta)] \otimes h(x,y,-z_1)\} \qquad \text{Eq. 5-9}$$

Now, we have the explicit forms of the reference and object beams at the recording plane. The recorded Fresnel hologram, $H(u,v)$, can be expressed as

$$H(u,v) = \left|u_R(u,v)_{ref} + u_R(u,v)_{obj}\right|^2 \qquad \text{Eq. 5-10}$$

$$= u_{ref} \cdot u_{ref}^* + u_{obj} \cdot u_{obj}^* + u_{obj} \cdot u_{ref}^* + u_{ref} \cdot u_{obj}^*$$

The goal is to retrieve the programmed defect information, $M_M(\xi,\eta)$, from the recorded hologram, $H(u,v)$. As mentioned earlier, the electric field distribution at *plane O* can be obtained by taking a Fourier transform of the recorded hologram, $H(u,v)$,

$$F.T.\{H(u,v)\} = F.T.\{u_{ref} \cdot u^*{}_{ref}\} + F.T.\{u_{obj} \cdot u^*{}_{obj}\} + F.T.\{u_{obj} \cdot u^*{}_{ref}\} + F.T.\{u_{ref} \cdot u^*{}_{obj}\}$$

Eq. 5-11

By taking a Fourier transform of $H(u,v)$, the first and the second terms in Eq.5-11 correspond to autocorrelation functions of $u_o(x\text{-}s, y)$ and $u_t(\xi, \eta) \otimes h(x,y,-z_1)$ respectively, and the third and the fourth terms correspond to the cross-correlation functions between $u_o(x\text{-}s, y)$ and $u_t(\xi, \eta) \otimes h(x, y,-z_1)$ and its complex conjugate. Thus, if we consider the displaced PSF, $u_o(x\text{-}s, y)$, as a displaced delta function, the cross-correlation functions yield the electric field information of the programmed defect at *plane O*, the image plane, such as

$$F.T.\{u_{obj} \cdot u^*{}_{ref}\} = F.T.\{u_{ref}\} \otimes F.T.\{u^*{}_{obj}\}$$ Eq. 5-12

$$= [u_O(x-s,y)] \otimes [u_M(\xi,\eta) \cdot M_M(\xi,\eta) \otimes h(x,y,-z_1)]$$

where s indicates the displacement or the separation of the two PSFs at the image plane. Equation 5-12 represents the displaced PSF convolved with the product of the illumination beam and programmed defect *at the image plane*. This indicates that the resolution of the system is limited by the PSF of the optics. The FWHM of the PSF is ~100 nm, so the defect microscope with the current optical system can resolve the feature size as mall as 100 nm.

By approximating the PSF as a point source or a delta function, the desired electric field at the image plane, $R_o(x,y)$, can be further simplified. After simplification, Eq. 5-12 can be expressed as

$$R_O(x,y) = [u_M(\xi,\eta) \cdot M_M(\xi,\eta) \otimes h(x-s,y,-z_1)] \qquad \text{Eq. 5-13}$$

This is the final form of the electric field at the image plane obtained after Fourier transforming the recorded hologram. Now, in order to retrieve $M_M(\xi,\eta)$ located at the mask plane, $R_o(x,y)$ needs to be propagated to *plane M*, the mask plane. Again, the Fresnel propagation from the image plane to mask plane can be done by using a similar equation as Eq. 5-2, and the convolution kernel, $h(\xi,\eta,z_1)$, has a conjugate property of $h(x,y,-z_1)$. The propagated $R_o(x,y)$ to the mask plane can be written as

$$\begin{aligned} u_M(\xi,\eta) &= \{[u_M(\xi,\eta) \cdot M_M(\xi,\eta)] \otimes h(x,y,-z_1)\} \otimes h(\xi,\eta,z_1) \qquad \text{Eq. 5-14} \\ &= u_M(\xi,\eta) \cdot M_M(\xi,\eta) \end{aligned}$$

The PSF propagated to the mask plane, $u_M(\xi,\eta)$, which is also the illuminating beam, is given by Eq. 5-5, and can be experimentally obtained by using a mask without the programmed defect. Once $u_M(\xi,\eta)$ is known, $M_M(\xi,\eta)$ can be readily obtained.

The time required to reconstruct the data using the combination method described above is relatively short when the location of the mask plane (z_1) is well known. The Fresnel propagation integral is the most time consuming part. A single Fresnel integral is necessary if the exact value of z_1 is known, otherwise multiple Fresnel integrations are required for the

complete reconstruction of the programmed defect. In practice, it takes approximately 30 sec to completely reconstruct the programmed defect using a Sun microsystems' Ultra 2 workstation with dual processors and 512 Mb memory, although no effort has been made to optimize the process.

5.3.3 Results with a null mask

As stated above, a null mask (mask where neither window has defects), can be used to obtain the illumination beam profile, $u_M(\xi,\eta)$, at the mask plane. A typical hologram recorded with a null mask is shown in Fig. 5-7(a), along with its Fourier transform, Fig. 5-7(b). The Fourier transform represents the reconstruction of the image plane distribution. Because there is no defect present, Equation 5-12 can be written as

$$R_O(x,y) = [u_O^*(x-s,y)] \otimes [u_M(\xi,\eta) \otimes h(x,y)] \qquad \text{Eq. 5-15}$$

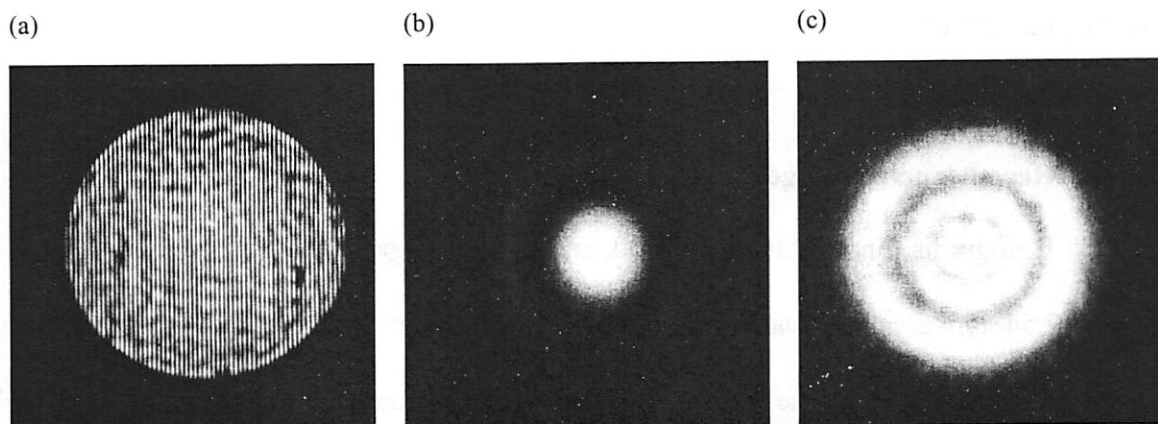

Fig. 5-7 (a) Recorded hologram for a null transmission mask. (b)Fourier transform of Fig. 5-7(a), representing the image-plane distribution. (c) The illumination pattern intensity at the mask plane. Since the mask is placed very near the image plane, the Fresnel rings are observed. It is essentially a near field image of Fig. 5-7(b).

Using Eq. 5-5, this can be further simplified to

$$R_O(x,y) = [u_O^*(x-s,y)] \otimes [u_O(x,y)] \qquad \text{Eq. 5-16}$$

Equation 5-16 is essentially an autocorrelation function of two PSFs, which are in this case two Airy functions. The autocorrelation function of an Airy pattern is an Airy pattern. The almost perfect reconstructed Airy pattern is shown in Fig. 5-7(b). In this configuration, the system essentially acts as a shearing interferometer, however, the object-side grating arrangement results in the shear being virtually zero, hence the sensitivity to aberrations is also nearly zero. This fortuitous result means that aberrations in the imaging optic will not adversely affect the imaging performance of the holographic defect reconstruction.

Figure 5-7(c) shows the defect-free intensity reconstruction, illumination beam, after Fresnel propagation to the mask plane. Figure 5-7(c) effectively represents the illumination pattern, $u_M(\xi,\eta)$, at the mask plane and can be used to normalize subsequent images obtained in the presence of actual defects.

5.3.4 Reconstructed images of program defects

Holograms for 500, 300, 200, 100, and 70 nm programmed opaque defects over 2.54 cm × 2.54 cm area are shown in Figs. 5-8(a) through 5-12(a), and the corresponding reconstructed images of the defects after Fresnel propagation are shown in Figs. 5-8(b) through 5-12(b), respectively. The reconstructed images reveal the illumination beam and the programmed defects. In order to more accurately represent the transmittance of the mask

and isolate the programmed defects from the reconstructed images, they have been normalized by the mask-plane illumination pattern [Fig. 5-7(c)]. The reconstructed images of the programmed defects with normalizations are shown in Figs. 5-8(c) through 5-12(c). The normalized images cover an area of 1.7-μm × 1.7-μm.

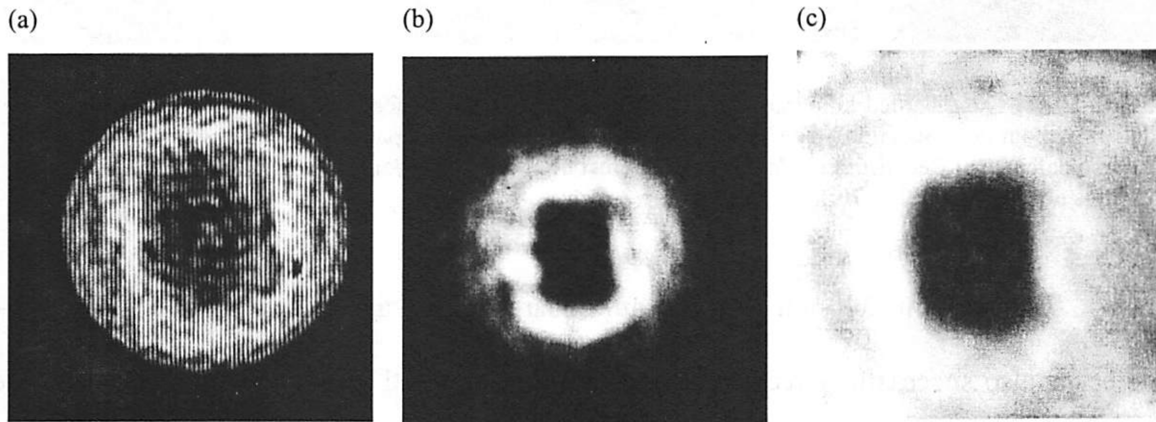

Fig. 5-8 (a) The recorded hologram for the 500 nm programmed defect. (b) Reconstructed image of the defect without normalization. The image represents the illumination pattern intensity with the 500 square opaque defect. (c) Reconstructed image of the defect after normalization. The reconstructed image shown in (b) is normalized with 5-7(c).

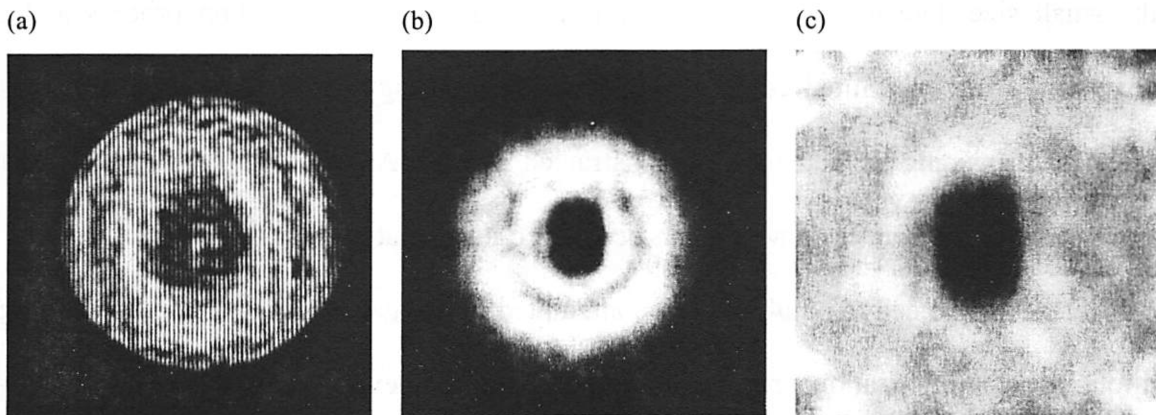

Fig. 5-9 (a) The recorded hologram for the 300 nm programmed defect. (b) Reconstructed image of the defect without normalization. The image represents the illumination pattern intensity with the 300 square opaque defect. (c) Reconstructed image of the defect after normalization. The reconstructed image shown in (b) is normalized with 5-7(c).

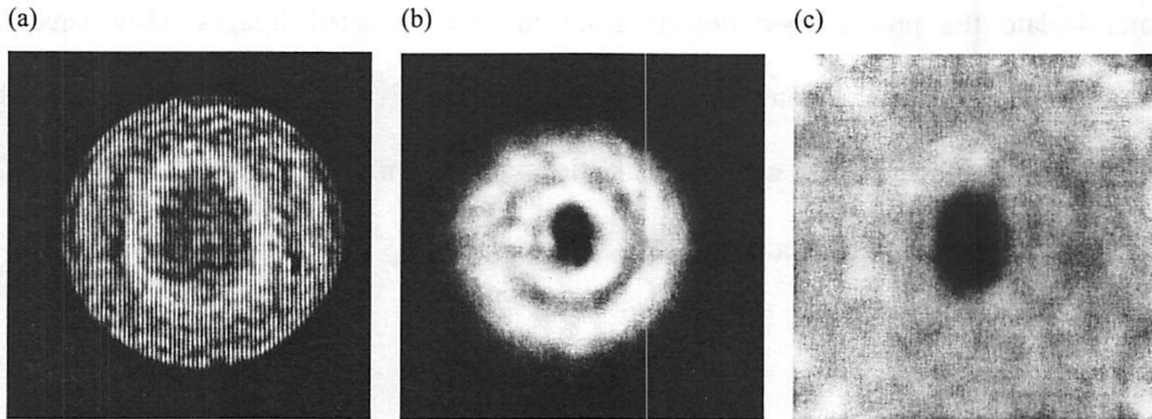

Fig. 5-10 (a) The recorded hologram for the 200 nm programmed defect. (b) Reconstructed image of the defect without normalization. The image represents the illumination pattern intensity with the 200 square opaque defect. (c) Reconstructed image of the defect after normalization. The reconstructed image shown in (b) is normalized with 5-7(c).

The 500-nm, 300-nm and 200-nm square defects are clearly visible. The 100-nm defect is also successfully reconstructed, however, detailed shape information is lost due to the resolution limit of the holographic defect microscope. Observing the reconstruction of the 70-nm defect, we see that its shape is indistinguishable from that of 100-nm defect, however, the contrast is lower than the 100-nm defect case. We note that the rings around the small size defects are most likely artifacts from the normalization process and data analysis. The bandlimited coherent nature of the imaging process described here has the effect of producing ringing in the reconstructed images. Another source of ringing comes from the illumination itself which can be viewed as an out-of-focus coherent image of the Schwarzschild objective pupil. We have attempted to mitigate this second source of ringing through the normalization process described above, however, uncorrelated speckle in the images renders this normalization incomplete.

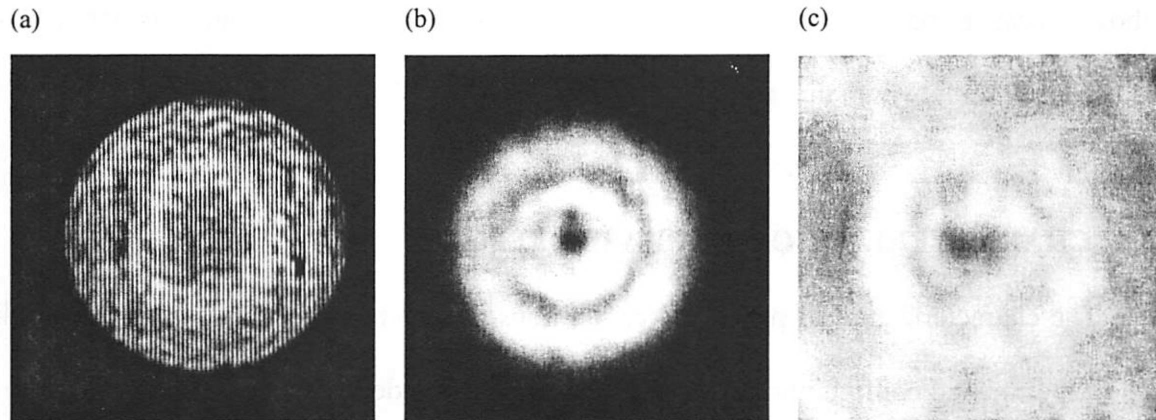

Fig. 5-11 (a) The recorded hologram for the 100 nm programmed defect. (b) Reconstructed image of the defect without normalization. The image represents the illumination pattern intensity with the 100 square opaque defect. (c) Reconstructed image of the defect after normalization. The reconstructed image shown in (b) is normalized with 5-7(c).

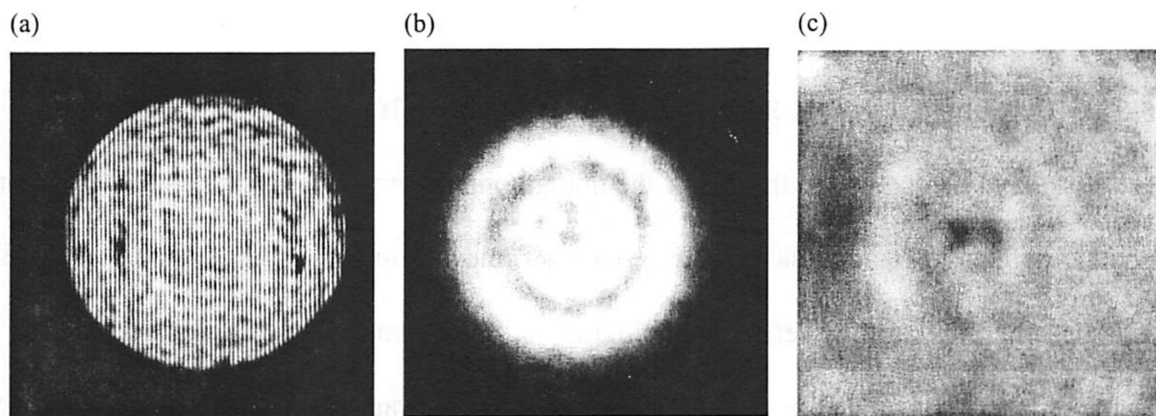

Fig. 5-12 (a) The recorded hologram for the 70 nm programmed defect. (b) Reconstructed image of the defect without normalization. The image represents the illumination pattern intensity with the 70 square opaque defect. (c) Reconstructed image of the defect after normalization. The reconstructed image shown in (b) is normalized with 5-7(c).

The ultimate resolution of this system is set by the NA of the reference beam, which in turn is set by the NA of the imaging optic (0.088 in the case presented here), just like a conventional microscope objective lens. The NA of 0.088 corresponds to a resolution of approximately 100 nm, using the equation ($res = 0.61 \cdot \lambda / NA$). As mentioned earlier, the resolution is also represented by a FWHM of the PSF of the imaging optic. Characterization of smaller defects will require the use of a higher NA imaging system. However, as noted

above, because aberrations in the imaging optic are effectively nulled-out, it is not necessary to use an extremely high quality optic.

5.4 CHARACTERIZATION OF PHASE DEFECTS

The characterization of phase defects on transmission masks is currently being studied. The experimental configuration would be identical to that described above (Fig.5-3) with the exception of the programmed amplitude defects being replaced by programmed phase defects. The material to be used for the phase defects is Molybdenum (Mo) which at a thickness of 86 nm provides a phase shift of π with only 40% attenuation.

5.5 CHARACTERIZING REFLECTION MASKS: PROPOSED SYSTEM

Here we have demonstrated the use of the holographic microscope for the characterization of opaque defects in transmission masks. To be a relevant tool for the development of EUV mask technology, however, the holographic microscope must be adapted to the characterization of reflection masks. A proposed configuration for such a device with some key components is depicted in Fig. 5-13.

5.5.1 Multilayer issues

In Fig. 5-13(a), the transmission mask used in the proof-of-principle experiments described above is replaced by a EUV multilayer-mask-blank. As discussed in Chapter 1, in the EUV lithography system, the EUV mask is placed approximately 5° off from the normal to the illuminating radiation. Because the mask is designed to be used in near normal incident angle, it is critical to measure the defects under similar conditions. A 45° turning

mirror is used to steer the reflected beams to the CCD. For clarity, the correct reflection angle is not shown in Fig. 5-13(a).

(a)

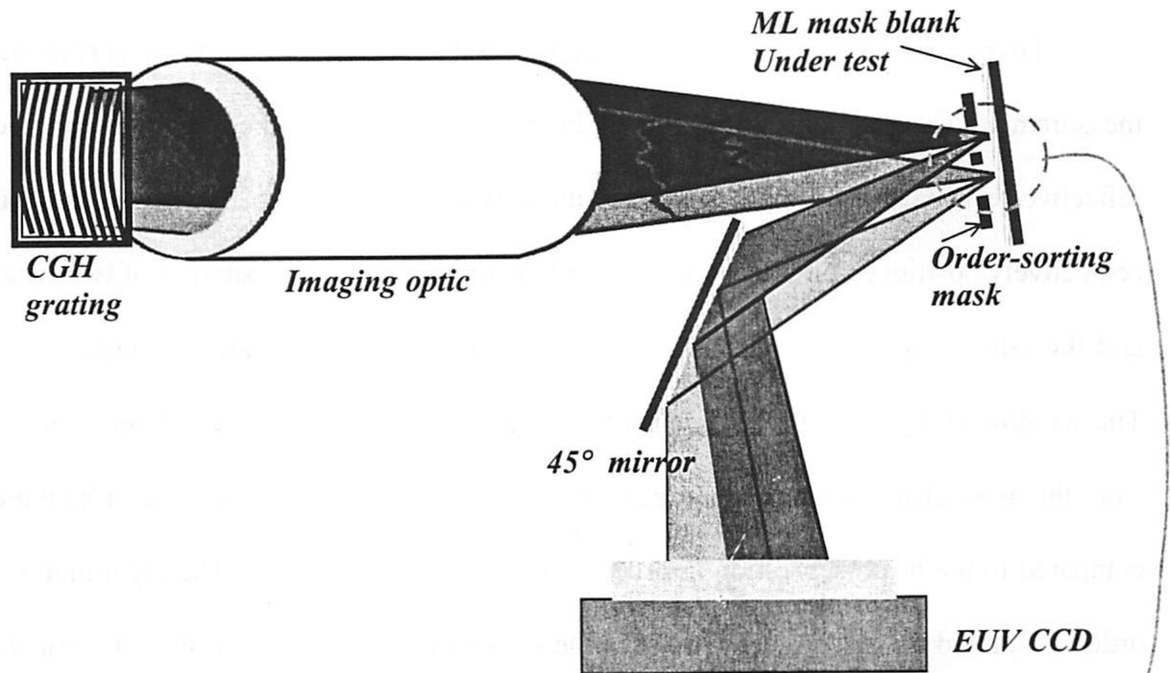

(b)

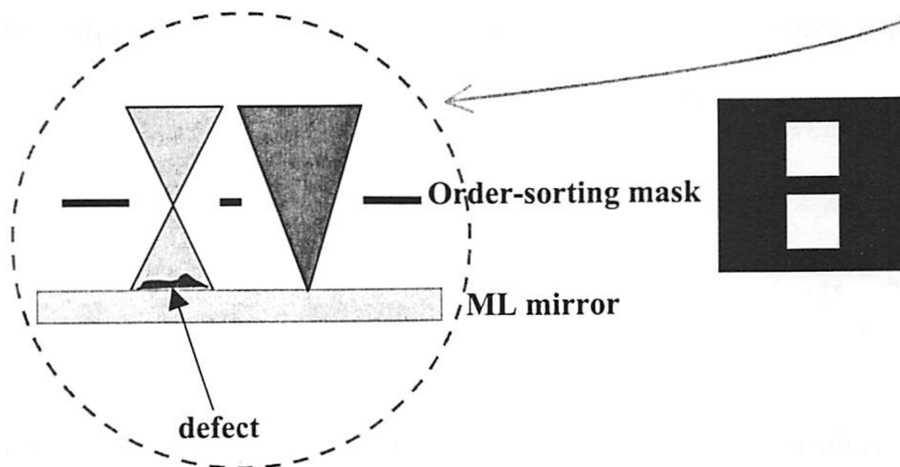

Figure 5-13 (a) A proposed experimental set-up to characterize EUV multilayer reflective mask blanks. A CGH grating and an order-sorting mask are used to select two orders with different foci. Due to the space constraint, a 45° mirror is placed to direct the reflected object and reference beams to the CCD camera, where the hologram of the defect is recorded. (b) Detailed view of the dotted-circle area in (a). The zeroth order focuses at the surface of the mask, and the first order focuses near the order-sorting mask plane.

5.5.2 45° mirror and order sorting aperture

Due to the space constraint, the 45° mirror is placed to direct the reflected object and reference beams to the CCD camera, where the hologram of the defect is recorded.

To prevent extraneous orders from the grating beam splitter from corrupting the measurement, an order-sorting mask must be positioned between the imaging optic and the reflective test mask [Fig. 5-13(b)]. This mask would contain two free-standing windows respectively positioned on the two grating orders of interest. The separation of two windows and the window sizes depend on the beam-splitting grating pitch and the inspecting area. The window size should be larger than the illuminating beam because the reflected orders from the mask also have to pass through the windows. The window size cannot be too large compared to the beam separation in order to prevent data corruption. The separation of two orders is limited by several factors. When the separation of two orders is too far compared to the coherence length of the source, the interference pattern or hologram may not be formed at the recording plane. The maximum separation of two orders due to the coherence length (l_{coh}) requirement is given by

$$S_{coh} = \frac{l_{coh}}{NA} \qquad \text{Eq. 5-17}$$

where NA is the numerical aperture of the system. The other factor to consider for the order separation is the fringe density at the recording device. When two orders are separated by a distance s, the number of fringes recorded at the CCD camera is given by $N_{fringes} = 2\frac{s}{\lambda}NA$ [40], and this is equal to the path length difference in waves. If the two orders are separated

too far, the number of fringes recorded in the recording device exceeds the *Nyquist* limit. In summary, the relationship between the minimum order separation (s_{min}), window size (w), maximum order separation (s_{max}), and recording device pixel size (x) are described in the following equations.

$$S_{\min} = \frac{3}{2}w \qquad \text{Eq. 5-18}$$

$$S_{\max} = \frac{\lambda z}{2x} - \frac{w}{2} \qquad \text{Eq. 5-19}$$

where z is the distance from the image plane to the recording plane, and Equation 5-18 and 5-19 are valid only if S_{max} is greater than S_{coh}. The minimum order separation, S_{min}, is obtained by using the same argument described in section 3.51, and the maximum order separation, S_{max}, is obtained by the *Nyquist* limit of the recording device.

For example, the beamline bandwidth ($\lambda/\Delta\lambda$) of 500 yields the coherence length of approximately 7 μm. According to Eq. 5-17, the bandwidth of the source provides the S_{coh} to be ~80 μm for NA of 0.088. If we assume that the interested inspection area is 10 μm in diameter, the window size (w) is chosen to be ~18 μm to be larger than the beam size. Then, the separation of the two windows is 27 μm center to center, and the desired separation is achieved by using a 3.0-μm pitch grating. The *Niquist* limited separation, S_{max}, is approximately 30 μm, which is larger than the intended separation, 27 μm. The 2.54 cm × 2.54 cm area CCD camera with 1024 pixels × 1024 pixels is placed ~144 mm from the image plane in order to fill the entire area of the detector (NA of 0.088). In this design, the order sorting windows should be placed ~10 μm from the multilayer mask surface.

5.5.3 Holographic optical element: a beam-splitting grating

In the proof-of-principle experiment described in the previous sections, the mask was intentionally positioned out of focus allowing a larger area to be inspected. There was no concern of reference beam contamination because the reference window was kept clean (no defects on the reference window). In a practical situation, however, it is not possible to distinguish between the two beams. If both beams are of the same size on the sample, they will be equally likely to encounter defects and it will be hard to isolate an individual defect. This potential problem can be minimized by making one of the two beams (the reference beam) significantly smaller on the sample. This could be achieved by adding optical power to the beam splitter grating allowing the zeroth and first-diffracted orders to be focused to different planes as shown in Fig. 5-13(b). The grating now effectively becomes a holographic optical element, like a computer-generated hologram (CGH) [93,94]. An example image diagram of diffraction patterns from a CGH grating at the multilayer surface is depicted in Fig. 5-14. The zeroth order, which is focused on the multilayer mirror surface, is used as a reference beam, and the first order with some amount of defocus is used as an object beam. The reference beam is substantially small at the inspection area so it is less likely to hit defects, while the object beam illuminates the defect area with a larger beam.

For the configuration with a CGH grating, Fresnel propagation may be eliminated in the hologram reconstruction process. The proposed system with a CGH grating allows us to record Fourier-transform holograms similar to the holograms described in Chapter 3 and 4 while inspecting a larger area with the defocused object beam. The Fourier-transform hologram is attractive due to its simple reconstruction process.

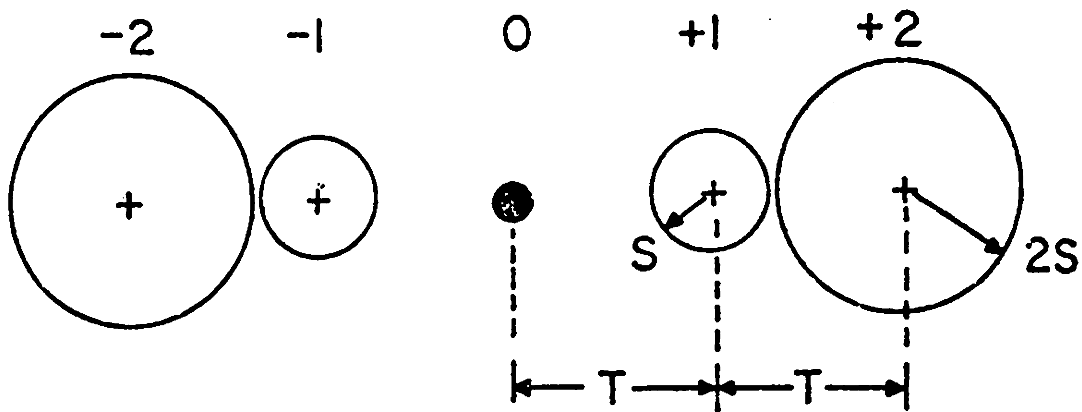

Fig. 5-14 The image diagram of diffraction patterns from a CGH grating. The right amount of defocus is added to the grating to generate two orders with different foci. The spots size increases as the order number increases. The zeroth order is used as a reference beam and the second order is used as an object beam.

It should be also noted that, in designing the CGH grating, the duty cycle has to be considered to balance the reference and object beam powers. High contrast holograms with less exposure times can be achieved by balancing two beam powers.

5.6 CONCLUSION

The use of holographic microscopy for the characterization of opaque defects in transmission masks has been successfully demonstrated at 13.4-nm wavelength. The biggest advantage of using a holographic technique is that both amplitude and phase information can be directly obtained. Amplitude defects of sizes ranging from 500 to 70 nm have been holographically reconstructed. The characterization of equivalently sized phase defects is currently under investigation.

A holographic microscope system to characterize defects on a reflective EUV multilayer mask blank has been proposed. The various design constraints have been discussed, and a

feasible layout including an order-sorting aperture and holographic beam splitter has been presented.

Chapter 6

Summary

Various applications of holographic metrology at 13.4-nm wavelength in support of EUV lithography development have described and demonstrated. These applications include wavefront interferometry, aerial image monitoring, coherence characterization, and defect microscopy.

6.1 INTERFEROMETRY

Motivated by the desire for near diffraction-limited imaging performance from EUV projection lithography optics, the PS/PDI has recently been developed. The PS/PDI is extremely stable and has phase shift capability increasing its accuracy and throughput. The PS/PDI has been successfully used to characterize several prototype EUV lithographic optics. The demonstrated capabilities of the PS/PDI include measuring multilayer-coating errors, characterizing flare, and performing at-wavelength alignment. To assess the wavefront measurement quality, various null tests have been performed.

As part of the research presented here, the precision and accuracy of the PS/PDI has been studied by means of computer simulations. The simulation results reveal the systematic-error-limited accuracy of 0.002λ (λ=13.4 nm) with the pinhole size of 100 nm, and the simulation results are also used to verify the two-pinhole null experiments.

Also developed as part of this research is a new DUV implementation of the PS/PDI geared towards the characterization of DUV-radiation-induced damage. This 193nm-PS/PDI using an upstream grating configuration is based on the EUV PS/PDI system. The interferometer preserves the advantages of the previously described EUV phase-shifting point diffraction interferometer but offers higher relative efficiency. Wavefront measurement of an imaging system, operating at 193-nm wavelength, has been reported. Direct measurement of the refractive index change in DUV radiation-damaged fused silica sample has been also investigated as an application.

6.2 AERIAL IMAGE MONITORING

Although it is possible to predict imaging performance based on wavefront metrology data, it is often desirable to obtain direct measurements of imaging performance of lithographic optics. As described in Chapter 3, to address this need a holographic aerial image monitoring system has been developed through modification of the PS/PDI. Using this holographic method allows one to directly monitor the coherent imaging performance of the lithographic system without printing in photoresist. Moreover, the system provides electric-field information including phase and amplitude, rather than simply intensity.

The holographic aerial image monitor has been used to study the imaging performance of a 10×-Schwarzschild optic using various amplitude and phase objects. The study included

through-focus measurements to identify the depth of focus of the optical system and the resolution of the system was demonstrated to be better 100 nm.

The results obtained with the holographic aerial image recording system have also been verified by way of computer simulation based on actual interferometry results, revealing good agreement.

6.3 COHERENCE MEASUREMENT

Understanding illumination coherence properties is crucial to the design of various systems. As new instruments and sources are developed at EUV avelengths, it is important to be able to quantitatively characterize their illumination coherence properties.

As described in Chapter 4, the holographic aerial image monitoring system can be modified to allow for the characterization of the illumination mutual coherence function. Unlike the traditional two-pinhole method, the holographic method requires only a single measurement to characterize the coherence area, assuming the illumination to be stationary.

The holographic method has been used to characterize two EUV illuminators: a K-B condenser system and a pinhole illuminator. For the K-B critical illuminator system, the coherence width of 7.1 μm has been measured with the undulator operating at its natural bandwidth. This study also included the effects of various beamline elements including the monochromator. For the pinhole illuminator system, a coherence width lager than 25 μm was measured. This result supports the use pinhole filters for the generation of full spatial coherence.

6.4 DEFECT MICROSCOPY

Finally, as described in Chapter 5, the holographic aerial image monitoring system can be modified to act as a holographic microscope for objects placed on the image side of the optical system. In this mode EUV mask blank defect characterization can be performed. This addresses a significant concern for the commercial viability of EUV lithography: namely, the fabrication of nearly defect-free multilayer mask blanks. Because there are no known methods to correct defects in and on a multilayer, it is crucial to identify the defects providing feedback for the development of a nearly zero-defect multilayer mask fabrication process.

The concept of using holographic microscopy as an EUV mask-blank defect inspection tool has been validated by characterizing programmed defects on simple transmission masks. This method allows for the characterization of both amplitude and phase defects. In the demonstration presented here a series of programmed amplitude defects size ranging from 500 to 70 nm were successfully characterized. Although not yet demonstrated, it is evident that this method could equally well be applied to phase defects. It is also important to note that the demonstrated method could also be implemented in the more relevant reflection-mask case. In Chapter 5, the design of such an implementation was described in detail.

Bibliography

1. J. S. Petersen, M. McCallum, N. Kachwala, R. Socha, J.F. Chen, T. Laidig, B.W. Smith, R. Gordon, C.A. Mack, **"Assessment of a hypothetical road map that extends optical lithography through the 70 nm technology node"**, Proceedings of the SPIE - The International Society for Optical Engineering, vol.**3741**, (Lithography for Semiconductor Manufacturing, Edinburgh, UK, 19-21 May 1999.) SPIE-Int. Soc. Opt. Eng, 1999. p.73-89.

2. S. Okazaki ,**"Future of optical lithography"**, Proceedings of the SPIE - The International Society for Optical Engineering, vol.**3749**, (18th Congress of the International Commission for Optics, San Francisco, CA, USA, 2-6 Aug. 1999.) SPIE-Int. Soc. Opt. Eng, 1999. p.328-9.

3. K. A. Chivers, **"Challenge of extending optical lithography"**, Proceedings of the SPIE - The International Society for Optical Engineering, vol.**3741**, (Lithography for Semiconductor Manufacturing, Edinburgh, UK, 19-21 May 1999.) SPIE-Int. Soc. Opt. Eng, 1999. p.48-58.

4. M. Maenhoudt., S. Verhaegen., K. Ronse, D. Flagello, B. Geh, W. Kaiser, **"Feasibility of printing 0.1 mu m technology with optical lithography,"** Proceedings of the SPIE - The International Society for Optical Engineering, vol.**3679**, pt.1-2, (Optical Microlithography XII, Santa Clara, CA, USA, 17-19 March 1999.) SPIE-Int. Soc. Opt. Eng, 1999. p.347-57.

5. J. A. McClay, A.S.L. McIntyre, **"157 nm optical lithography: The accomplishments and the challenges,"** Solid State Technology, vol.**42**, (no.6), PennWell Publishing, June 1999. p.57, 59-60, 62, 64, 66, 68.

6. K. Nakazawa, T. Onodera, M. Sasago, **"Approach to next-generation optical lithography"**, Japanese Journal of Applied Physics, Part 1 (Regular Papers, Short Notes & Review Papers), vol.**38**, (no.5A), Publication Office, Japanese Journal Appl. Phys, May 1999. p.3001-2.

7. P. Burggraaf, **"Optical lithography to 2000 and beyond,"** Solid State Technology, vol.**42**, (no.2), PennWell Publishing, Feb. 1999. p.31-2, 34, 36, 38, 41.

8. P. Rai-Choudhury, **"Handbook of Microlithography, micromachning, and microfabrication"**, SPIE Optical Engineering Press, 1997, Bellingham, Wash., USA.

9. R. DeJule,. **"Next-generation lithography tools: the choices narrow"**, Semiconductor International, vol.**22**, (no.3), Cahners Publishing, March 1999. p.48-50, 52.

10. D. L. White, J. E. Bjorkholm, J. Bokor, L. Eichner, R.R. Freeman, T.E. Jewell, W. M. Mansfield, A. A. MacDowell, L.H. Szeto, D.W. Taylor, D.M. Tennant, W. K.

Waskiewicz, D. L. Windt, O. R. Wood, **"Soft X-ray projection lithography"**, Solid State Technology, vol.**34**, (no.7), July 1991. p.37-42.

11. D. A. Tichenor, G.D. Kubiak, R.H. Stulen, **"Extreme ultraviolet lithography for circuit fabrication at 0.1 mu m feature size"**, Proceedings of the SPIE - The International Society for Optical Engineering, vol.**2523**, (Applications of Laser Plasma Radiation II, San Diego, CA, USA, 12-14 July 1995.) 1995. p.23-8.

12. R. H. Stulen, D.W. Sweeney, **"Extreme ultraviolet lithography,"** IEEE Journal of Quantum Electronics, vol.**35**, (no.5), IEEE, May 1999. p.694-9.

13. C. W. Gwyn, **"Extreme ultraviolet lithography,"** Journal of Vacuum Science & Technology B (Microelectronics and Nanometer Structures), vol.**16**, (no.6), (42nd International Conference on Electron, Ion, and Photon Beam Technology and Nanofabrication, Chicago, IL, USA, 26-29 May 1998.) AIP for American Vacuum Soc, Nov.-Dec. 1998. p.3142-9.

14. S. Vaidya, D. Sweeney, R. Stulen, D. Attwood, **"Extreme ultraviolet lithography for 0.1 mu m devices,"** 1999 International Symposium on VLSI Technology, Systems, and Applications. Proceedings of Technical Papers. (Cat. No.99TH8453), (1999 International Symposium on VLSI Technology, Systems, and Applications. Proceedings of Technical Papers. (Cat. No.99TH8453), Proceedings of International Symposium on VLSI Technology Systems and Applications, Taipei, Taiwan, 8-10 June 1999.) Piscataway, NJ, USA: IEEE, 1999. p.127-30.

15. R. H. Stulen, **"Progress in the development of extreme ultraviolet lithography exposure systems"**, Microelectronic Engineering, vol.**46**, (no.1-4), (Micro-and-Nano-Engineering 98. MNE. International Conference on Micro-and Nanofabrication, Leuven, Belgium, 22-24 Sept. 1998.) Elsevier, May 1999. p.19-22.

16. http://www-cxro.lbl.gov/optical_constants/

17. J. D. Jackson, **"Classical Electrodynamics"**, John Wiley and Sons, New York, 1975, Ch.2.

18. D. T. Attwood, **"Soft X-Rays and Extreme Ultraviolet Radiation"**, Cambridge university press, New York, NY, 1999, Ch. **4**.

19. E. Spiller, **"Reflective multilayer coatings for the far UV region"**, Applied Optics, vol.**15**, (no.10), Oct. 1976. p.2333-8.

20. E. Spiller, A. Segmuller, J. Rife, R.P. Haelbich, **"Controlled fabrication of multilayer soft-X-ray mirrors,"** Applied Physics Letters, vol.**37**, (no.11), 1 Dec. 1980. p.1048-50.

21. W. T. Silfvast,. M. Klosner, G. Shimkaveg, H. Bender, G. Kubiak, N. Fornaciari, **"High-power plasma discharge source at 13.5 nm and 11.4 nm for EUV lithography,"** Proceedings of the SPIE - The International Society for Optical Engineering, vol.**3676**, pt.1-2, (Emerging Lithographic Technologies III, Santa Clara, CA, USA, 15-17 March 1999.) SPIE-Int. Soc. Opt. Eng, 1999. p.272-5.

22. G. D. Kubiak, L.J. Bernardez, K. Krenz, W.C. Sweatt, **"Scale-up of a cluster jet laser plasma source for extreme ultraviolet lithography,"** Proceedings of the SPIE - The International Society for Optical Engineering, vol.**3676,** pt.1-2, (Emerging Lithographic Technologies III, Santa Clara, CA, USA, 15-17 March 1999.) SPIE-Int. Soc. Opt. Eng, 1999. p.669-78.

23. G. D. Kubiak, L.J. Bernardez, K. Krenz, W.C. Replogle, W.C. Sweatt, D.W. Sweeney, Hudyma, R.M.; Shields, H. **"High-power source and illumination system for extreme ultraviolet lithography,"** Proceedings of the SPIE - The International Society for Optical Engineering, vol.**3767**, (EUV, X-Ray, and Neutron Optics and Sources, Denver, CO, USA, 21-23 July 1999.) SPIE-Int. Soc. Opt. Eng, 1999. p.136-42.

24. G. D. Kubiak, L. J. Bernardez, K. Krenz, **"High-power extreme ultraviolet source based on gas jets,"** Proceedings of the SPIE - The International Society for Optical Engineering, vol.**3331**, (Emerging Lithographic Technologies II, Santa Clara, CA, USA, 23-25 Feb. 1998.) SPIE-Int. Soc. Opt. Eng, 1998. p.81-9.

25. D. T. Attwood, **"Soft X-Rays and Extreme Ultraviolet Radiation"**, Cambridge university press, New York, NY, 1999, Ch.6.

26. D. C Ockwell, N. C. Crosland, V. C. Kempson, "**Synchrotron light as a source for extreme ultraviolet lithography**", Journal of Vacuum Science & Technology B (Microelectronics and Nanometer Structures), vol.**17**, (no.6), (43rd International Conference on Electron, Ion, and Photon Beam Technology and Nanofabrication, Marco Island, FL, USA, 1-4 June 1999.) AIP for American Vacuum Soc, Nov. 1999. p.3043-6.

27. E. Di Fabrizio, A. Nucara, M. Gentili, R. Cingolani, **"Design of a beamline for soft and deep lithography on third generation synchrotron radiation source,"** Review of Scientific Instruments, vol.**70**, (no.3), AIP, March 1999. p.1605-13.

28. H. N. Chapman, K. A. Nugent, **"Novel condenser for EUV lithography ring-field projection optics"** Proceedings of the SPIE - The International Society for Optical Engineering, vol.**3767**, (EUV, X-Ray, and Neutron Optics and Sources, Denver, CO, USA, 21-23 July 1999.) SPIE-Int. Soc. Opt. Eng, 1999. p.225-36.

29. D. M. Williamson, "**The elusive diffraction limit**", OSA Proceedings on Extreme ultraviolet lithography, Vol. **23**, edited by F. Zernike and D.T. Attwood, (Optical Society of America, Washington, DC, 1995), pp. 68-76.

30. V. Rao, J. Cobb, C. Henderson, U. Okoroanyanwu, D. Bozman, P. Mangat, R. Brainard, J. Mackevich, **"Ultrathin photoresists for EUV lithography"**, Proceedings of the SPIE - The International Society for Optical Engineering, vol.**3676**, pt.1-2, (Emerging Lithographic Technologies III, Santa Clara, CA, USA, 15-17 March 1999.) SPIE-Int. Soc. Opt. Eng, 1999. p.615-26.

31. C. R. Kessel, L. D. Boardman, S. J. Rhyner, J. L. Cobb, C. C. Henderson, V. Rao, U. Okoroanyanwu,, **"Novel silicon-containing resists for EUV and 193 nm lithography,"** Proceedings of the SPIE - The International Society for Optical Engineering, vol.**3678**, pt.1-2, (Advances in Resist Technology and Processing XVI, Santa Clara, CA, USA, 15-17 March 1999.) SPIE-Int. Soc. Opt. Eng, 1999. p.214-20.

32. C. Henderson, D. Wheeler, T. Pollagi, G. Cardinale, D. O'Connell, A. Fisher, V. Rao, J. Goldsmith, **"Top surface imaging for extreme ultraviolet lithography,"** Journal of Photopolymer Science and Technology, vol.**11**, (no.3), Tech. Assoc. Photopolymers, 1998. p.459-64.

33. C. Henderson, D. Wheeler, T. Pollagi, D. O'Connell, J. Goldsmith, A. Fisher, G. Cardinale, J. Hutchinson, V. Rao, **"Top surface imaging resists for EUV lithography,"** Proceedings of the SPIE - The International Society for Optical Engineering, vol.**3331**, (Emerging Lithographic Technologies II, Santa Clara, CA, USA, 23-25 Feb. 1998.) SPIE-Int. Soc. Opt. Eng, 1998. p.32-40.

34. R. N. Smartt and W. H. Steel, **"Theory and application of point diffraction interferometers,"** Jap. J. Appl. Phys. Vol. **14,** Suppl. 14-1, 351-356 (1975).

35. G. E. Sommargren, **"Point diffraction interferometry at soft x-ray wavelengths"**, OSA Proceedings on Soft-xray projection lithography, vol. **18,** edited by A.M. Hawryluk and R.H. Stulen, (Optical Society of America, Washington DC, 1993), pp.100-4.

36. W. Linnk, **"A simple interferometer to test optical systems,"** Proc. of the Academy of Science of USSR 1, 210-212 (1933).

37. H. Medecki, E. Tejnil, K. A. Goldberg, and J. Bokor, **"A Phase-Shifting Point Diffraction Interferometer,"** Opt. Lett., **21** (19), 1526-8 (1996).

38. D. T. Attwood, **"Soft X-Rays and Extreme Ultraviolet Radiation"**, Cambridge university press, New York, NY, 1999, Ch. **5**.

39. D. T. Attwood, **"Soft X-Rays and Extreme Ultraviolet Radiation"**, Cambridge university press, New York, NY, 1999, Ch.**10**.

40. K. Goldberg, **"EUV Interferometry"**, Doctoral Dissertation, Department of Physics, University of California, Berkeley (1997).

41. E. Tejnil, "**Characterization of Extreme ultraviolet imaging systems**", Doctoral Dissertation, Department of Electrical Engineering and Computer Science, University of California, Berkeley (1997).

42. K. A. Goldberg, R. Beguiristain, J. Bokor, H. Medecki, D. T. Attwood, K. Jackson, E. Tejnil, G. E. Sommargren, "**Progress toward λ/20 EUV interferometry,**" Journal of Vacuum Science and Technology B, **13** (6), 2923-7 (1995).

43. K. A. Goldberg, R. Beguiristain, J. Bokor, H. Medecki, K. Jackson, and D. T. Attwood, G. E. Sommargren, J. P. Spallas, and R. Hostetler, "**At-wavelength testing of optics for EUV,**" Proceedings of the SPIE, vol. **2437**, 347-54 (1995).

44. E. Tejnil, K. A. Goldberg, H. Medecki, R. Beguiristain, J. Bokor, and D. T. Attwood, "**Phase-shifting point diffraction interferometry for at-wavelength testing of lithographic optics,**" OSA TOPS Volume on Extreme Ultraviolet Interferometry (1996).

45. K. A. Goldberg, E. Tejnil, S. H. Lee, H. Medecki, D. T. Attwood, K. H. Jackson, and J. Bokor, "**Characterization of an EUV Schwarzschild objective using phase-shifting point diffraction interferometry,**" Proceedings of the SPIE, **3048,** 264-70 (1997).

46. E. Tejnil, K. A. Goldberg, S. H. Lee, H. Medecki, P. J. Batson, P. E. Denham, A. A. MacDowell, and J. Bokor, "**At-wavelength interferometry for EUV lithography,**" Journal of Vacuum Science and Technology B, vol. **15** (6), 2455-2461 (1997).

47. S. H. Lee, K. A. Goldberg, P. Naulleau, E. Tejnil, H. Medecki, C. Bresloff, C. Chang, D. T. Attwood, and J. Bokor, "**At-wavelength interferometry of Extreme Ultraviolet Lithographic Optics,**" Presented at NIST international conference on characterization and metrology for ULSI technology, March, 1998.

48. K. A. Goldberg, P. Naulleau, S. Lee, C. Bresloff, D. Attwood, and J. Bokor, "**High-accuracy interferometry of EUV lithographic optical systems,**" Proceedings of the EIPBN'98 Conference, Chicago, IL, May 1998, Journal of Vacuum Science and Technology B, vol. **16** (6), 3435-3439 (1998).

49. D. T. Attwood, E. Anderson, P. Batson, R. Beguiristain, J. Bokor, K. Goldberg, E. Gullikson, K. Jackson, K. Nguyen, M. Koike, H. Medecki, S. Mrowka, R. Tackaberry, E. Tejnil, and J. Underwood, "**At-wavelength metrologies for extreme ultraviolet lithography,**" Future Electron Devices Journal Vol. **9** Suppl. 1 , 5-14 (1998).

50. P. Naulleau, K. A. Goldberg, S. H. Lee, C. Chang, P. Batson, D. Attwood, and J. Bokor, "**Recent advances in EUV phase-shifting point diffraction interferometry,**" Proc. SPIE **3767,** 154-63.

51. K. A. Goldberg, P. Naulleau, and J. Bokor, "**EUV interferometric measurements of diffraction-limited optics,**" Journal of Vacuum Science and Technology B, vol.**17** (6), 2982-86 (Nov.-Dec. 1999).

52. K. A. Goldberg, P. Naulleau, S. H. Lee, C. Chang, C. Bresloff, R. Gaughan, H. N. Chapman, J. Goldsmith, and J. Bokor, "**Direct comparison of EUV and visible-light interferometries,**" in Emerging Lithographic Technologies III, Y. Vladimirski, Ed., Proc. SPIE **3676**, 635-42, (1999).

53. K. A. Goldberg, P. Naulleau, P. J. Batson, P. Denham, J. Bokor, and H. N. Chapman, "**EUV Interferometry of a Four-mirror Ring Field EUV Optical System,**" Proceedings of the SPIE - The International Society for Optical Engineering (Emerging Lithographic Technologies II, Santa Clara, CA, USA, 27 Feb-3 Mar. 2000.), vol.**3997,** to be published (2000).

54. S. Lee, F. Piao, P. Naulleau, K. Goldberg, W. Oldham, and J. Bokor, "**193-nm phase-shifting point diffraction interferometer,**" Appl. Opts. vol. **82,** to be published (2000).

55. S. Lee, F. Piao, P. Naulleau, K. Goldberg, W. Oldham, and J. Bokor, "**At-wavelength characterization of DUV-radiation-induced damage in fused silica,**" Proceedings of the SPIE - The International Society for Optical Engineering (Emerging Lithographic Technologies II, Santa Clara, CA, USA, 27 Feb-3 Mar. 2000.), vol.**3998**, to be published (2000).

56. C. Chang, P. Naulleau, E. Anderson, and D. Attwood, "**Spatial coherence characterization of undulator radiation,**" Optics communications, accepted on June 8, to be published (2000).

57. J. W. Goodman, "**Statistical optics,**" 2nd Edition,Wiley, New York, 1985.

58. D. T. Attwood, "**Soft X-Rays and Extreme Ultraviolet Radiation**", Cambridge university press, New York, NY, 1999, Ch. **8**.

59. E.H. Anderson, Private conversation

60. J. P. Spallas, R. E. Hostetler, G. E. Sommargren, and D. R. Kania, "**Fabrication of extreme-ultraviolet point diffraction interferomter aperture arrays**", Applied optics, vol. **34**(28), pp. 6393-8, 1995.

61. D. M. Tennant, E. L. Raab, M. M. Becker, M. L. O'Malley, J. E. Bjorkholm, and R.W. Epworth, "**High resolution germanium zone plates and apertures for soft x-ray focalometry**", Journal of Vacuum Science and Technology B, vol. **8** (6), pp. 1970-4, 1990.

62. T. Wilson, D. Rothweiler, A. Tusche, F. Scholze, and W. Meyer-Ilse, "**Thinned, back-illuminated CCDs for x-ray microscopy**", X-Ray Microscopy IV, edited by V. Aristov and A.I. Erko, Chernogolovska, Russia, pp. 470-474, (1994).

63. Scientific Imaging Technologies, Inc. (SITe), http://www.site-inc.com/product-1024x1024-ccd.htm

64. D. A. Tichenor, G. D. Kubiak, M. E. Malinowski, R. H. Stulen, S.J. Haney, K.W. Berger, R.P. Nissen, R.L. Schmitt, G.A. Wilkerson, L.A. Brown, P.A. Spnce, P.S. Jin, W.C. Sweatt, W.W. Chow, J.E. Bjorkholm, R.R. Freeman, M.D. Himel, A.A. MacDowell, D.M. Tennant, O.R. Wood II, W.K. Waskiewcz, D.L. White, D.L. Windt, and T.E. Jewell, " **Development and chracterization of a 10X Schwarzchild system for SXPL**", OSA Proceedings on soft x-ray projection lithography, vol.**18**, edited by A.M. Hawryluk and R.H. Stulen, (OSA, Washington DC), pp.79-82, (1993).

65. E. A. Spiller, F. J. Weber, C. Montcalm, S. L. Baker, E. M. Gullickson, J.H. Underwood, "**Multilayer coating and tests of a 10X extreme ultraviolet lithographic camera**," in Emerging Lithographic Technologies II, Y. Vladimirski, ed., Proc. SPIE **3331**, 62-71, (1998).

66. J. E. M. Goldsmith, K. W. Berger, D. R. Bozman, G. F. Gardinale, et.al., "**Sub-100-nm imaging with the EUV 10X microstepper**," in Emerging lithographic technologies III, Y. Vladimirski, ed., Proc. SPIE 3676, 62-71, (1999).

67. D. Malacara, "**Optical Shop testing**", Ch.**13** and Ch. **14**, Wiley, New York, (1992).

68. K. M. Skulina, C. S. Alford, R. M. Bionta, D. M.; Makowiecki, E. M.; Gullikson, R. Soufli, J. B. Kortright, J. H. Underwood, "**Molybdenum/beryllium multilayer mirrors for normal incidence in the extreme ultraviolet**," Applied Optics, vol.**34**, (no.19), 1 July 1995. p.3727-30.

69. G. E. Sommargren, (Edited by: G. D. Kubiak, D. R. Kania, D.R.), "**Phase shifting diffraction interferometry for measuring extreme ultraviolet optics,**" OSA Trends in Optics and Photonics. Vol. **4** Extreme Ultraviolet Lithography. From the Topical Meeting, (OSA Trends in Optics and Photonics. Vol.4 Extreme Ultraviolet Lithography. From the Topical Meeting, Proceedings of Extreme Ultraviolet Lithography (ISBN 1 55752 435 1), Boston, MA, USA, 1-3 May 1996.) Washington, DC, USA: Opt. Soc. America, 1996. p.108-12.

70. G. E. Sommargren, "**Diffraction methods raise interferometer accuracy,**" Laser Focus World, vol.32, (no.8), PennWell Publishing, Aug. 1996. p.61-2, 64, 66, 70-1.

71. K. A. Goldberg, P. Naulleau, J. Bokor, P. Batson, P. Denham, E. Anderson, S. Lee, and C. Chang, **EUV interferometric measurement and alignment of diffraction-**

limited optics," poster presentation, The Advanced Light Source Users Meeting (1999).

72. P. Naulleau, K. A. Goldberg, E. M. Gullikson, and J. Bokor, **"Interferometric at-wavelength flare characterization of EUV optical systems,"** Journal of Vacuum Science and Technology B, **17** (6), 2987-91 (Nov.-Dec. 1999).

73. P. Naulleau and K. A. Goldberg, **"A Dual-domain point diffraction interferometer,"** Applied Optics, **38** (16), 3523-33, (June 1, 1999).

74. P. Naulleau, K. A. Goldberg, S. H. Lee, C. Chang, C. Bresloff, P. Batson, D. Attwood, and J. Bokor, **"Characterization of the accuracy of EUV phase-shifting point diffraction interferometry,"** Emerging Lithographic Technologies II, Y. Vladimirski, (ed.), Proceedings of the SPIE **3331**, pp. 114-23.

75. P. Naulleau, K. A. Goldberg, S. H. Lee, C. Chang, D. Attwood, and J. Bokor, **"Extreme-ultraviolet phase-shifting point-diffraction interferometer: a wave-front metrology tool with subangstrom reference-wave accuracy,"** Applied Optics, **38** (35), 7252-63, (December 10, 1999).

76. S. Lee, **"Accuracy of phase-shifting point Diffraction Interferometer to test EUV optics,"** Master's thesis, Department of Electrical Engineering and Computer Science, May 1998.

77. J. W. Goodman, **"Fourier optics,"** McGraw-Hill, New York, 1996.

78. A. K. Wong, and A. R. Neureuther, **"Rigorous three dimensional time domain finite difference electromagnetic simulation for photolithography application,"** Ph.D. Dissertation, Electronic Research Laboratory, UC Berkeley, May 1995.

79. T. Pistor, **"Generalizing the TEMPEST FDTD Electromagnetic Simulation Program,"** MS report, Electronic Research Laboratory, UC Berkeley, May 1997.

80. S. Lee, P. Naulleau, K. A. Goldberg, and J. Bokor, **"EUV holographic aerial image recording,"** SPIE Microlithography Conference in Emerging Lithographic Technologies III, Proc. SPIE **3997**, to be published (2000).

81. S. Lee, P. Naulleau, K. A. Goldberg, C. Cho, and J. Bokor, **"EUV Fourier transform holography,"** Applied optics, submitted June 2000, to be published (2000).

82. P. Naulleau, private conversation.

83. E. M. Gullikson, S. L. Baker, J. E. Bjorkholm, J. Bokor, K. A. Goldberg, J. E. M. Goldsmith, C. Montcalm, P. Naulleau, E. A. Spiller, D. G. Stearns, J. S. Taylor, J. H.

Underwood, "**EUV scattering and flare of 10x projection cameras,**" in Emerging Lithographic Technologies III, Y. Vladimirski, ed., Proc. SPIE **3676**, 717-23 (1999).

84. C. Cho, Private conversation

85. C. A. Mack, "**PROLITH: A comprehensive optical lithography model**", Proc. SPIE **538**, 207-220 (1985).

86. P. Rai-Choudhury, "**Handbook of Microlithography, Micromachining, and Microfabrication,**" SPIE press, 74-82 (1997).

87. B. J. Thompson, E. Wolf, J. Opt. Soc. Amer. Vol. **47**, pg. 895 (1957).

88. S. Lee, P. Naulleau, K. Goldberg, S. Jeong, and J. Bokor, " **EUV holographic microscopy and its applications to EUV mask-blank defect characterizations,**" Proceedings of the EIPBN'00 Conference, Palm Spring, CA, May 2000, Journal of Vacuum Science and Technology B, to be published in Nov/Dec 2000.

89. S. Burkhart, C. Cerjan, P. Kearney, P. Mirkarimi, C. Walton, P. Ray-Chaudhuri, "**Low-defect reflective mask blanks for extreme ultraviolet lithography,**" Proceedings of the SPIE - The International Society for Optical Engineering, vol.**3676**, pt.1-2, (Emerging Lithographic Technologies III, Santa Clara, CA, USA, 15-17 March 1999.) SPIE-Int. Soc. Opt. Eng, 1999. p.570-7.

90. K. Nguyen, "**EUV lithography**", Ph.D. dissertation, Applied science and technology, UC Berkeley (1995).

91. Y. Lin and J. Bokor, "**Minimum critical defects in extreme-ultraviolet lithography masks**", Journal of Vacuum Science and Technologies, B **15**(6), 2467-2470, Nov/Dec 1997.

92. S. Jeong; L. Johnson, S. Rekawa.; C.C. Walton; and others, "**Actinic detection of sub-100 nm defects on extreme ultraviolet lithography mask blanks**", Journal of Vacuum Science & Technology B (Microelectronics and Nanometer Structures), vol.**17**, (no.6):3009-13 (1999).

93. J. C. Wyant, V.P Bennett, "**Using computer generated holograms to test aspheric wavefronts,**" Applied Optics, vol.**11**, (no.12), Dec. 1972. p.2833-9.

94. J. S. Loomis, "**Computer-generated holography and optical testing,**" Optical Engineering, vol.**19**, (no.5), Sept.-Oct. 1980. p.679-85.

95. M. Lurie, Journal of Optical Society of America, Vol. **58**, 1968, p. 614.

96. C. C. Aleksoff, **"Holographic determination of spatial coherence,"** 1970 Spring meeting of the Optical Society of America, (1970 Spring meeting of the Optical Society of America, Philadelphia, PA, USA, 7-10 April 1970.) Washington, DC, USA: Optical Soc. America, 1970. p.39.

97. I. Weingartner, **"Measurement of mutual coherence functions by image holography,"** Journal of the Optical Society of America, vol.**60,** (no.4), April 1970. p.572-3.

98. W. Mirande, I. Weingartner, **"Recording of inhomogeneous mutual coherence functions in one hologram by using a combination of image and Fourier (Fresnel) holography,"** Optics Communications, vol.**2,** (no.3), Aug. 1970. p.97-100.

99. D.I. Staselko, V.B. Voronin, A.G. Smirnov, **"Holographic method for measuring spatial coherence functions,"** Optika i Spektroskopiya, vol.**34,** (no.3), March 1973. p.561-6. (Translation: Optics and Spectroscopy)

100. Roychoudhuri, B.J. Thompson, **"Application of local reference beam holography to the study of laser beam parameters,"** Optical Engineering, vol.**13,** (no.4), July-Aug. 1974. p.347-53.

101. I.N. Ross, **"Design and operation of holographic techniques for measuring coherence,"** Optica Acta, vol.**22,** (no.8), Aug. 1975. p.639-51.

102. A. M. Dukhovnyi, A.E. Korolev, D.I. Staselko, **"Features of the measurement of the spatial coherence of laser emission by interferometric and holographic methods,"** Optika i Spektroskopiya, vol.**48,** (no.3), March 1980. p.560-7. (Translation: Optics and Spectroscopy)

103. W. J. Smith, **"Modern Optical Engineering: the design of optical system"**, 2nd Edition, McGraw-Hill, 1990, p.30-32.

104. G.F. Cardinale, J.E.M. Goldsmith, A. K. Ray-Chaudhuri, A. Fisher, S. Hector, P.J.S. Mangat, Z. Masnyj, D. Mancini, B. Wilkinson, J. Bokor, S. Jeong, S. Burkhart, C. Cerjan, C. Walton, C. Larson, P.Y. Yan, G. Zhang, **"Comparison of at-wavelength inspection, printability, and simulation of nm-scale substrate defects in extreme ultraviolet lithography (EUVL),"** Proceedings of the SPIE, vol.**3873,** pt.1-2, SPIE-Int. Soc. Opt. Eng, 1999. p.429-39.

105. T. Pistor, A. Neureuther, **"Extreme ultraviolet mask defect simulation,"** Journal of Vacuum Science & Technology B (Microelectronics and Nanometer Structures), vol.17, (no.6), Nov. 1999. p.3019-23.

106. T. Pistor, A. Neureuther, **"Calculating aerial images from EUV masks,"** Proceedings of the SPIE - The International Society for Optical Engineering,

vol.3676, pt.1-2, (Emerging Lithographic Technologies III, Santa Clara, CA, USA, 15-17 March 1999.) SPIE-Int. Soc. Opt. Eng, 1999. p.679-96.